Ligand Fluorination to Mitigate the Raman Relaxation of Dy(III) Single-Molecule Magnets: A Combined Terahertz, Far-IR and Vibronic Barrier Model Study

Yan Ma[†], Yuan-Qi Zhai[†], Qian-Cheng Luo, You-Song Ding, and Yan-Zhen Zheng*

[*]   Y. Ma, Y.-Q. Zhai, Q.-C. Luo, Dr. Y.-S. Ding, Prof. Y.-Z. Zheng.
        Frontier Institute of Science and Technology (FIST), State Key Laboratory for Mechanical Behavior of Materials, MOE Key Laboratory for Nonequilibrium Synthesis of Condensed Matter, Xi'an Key Laboratory of Sustainable Energy and Materials Chemistry, School of Chemistry and School of Physics, Xi'an Jiaotong University.
        99 Yanxiang Road, Xi'an, Shaanxi 710054, P. R. China.
        E-mail: zheng.yanzhen@xjtu.edu.cn.
[†]   These authors contributed equally to this work.

        Supporting information for this article is given via a link at the end of the document.

Abstract: *Engineering the local dynamic environment is currently the major approach for preventing fast magnetization loss for single-molecule magnets (SMMs). It is hypothesized that the presence of fewer −CH₃ which results in fewer C−H bonds, would reduce excitation energy loss via vibrations, but thus far, no experimental evidence clearly elaborates this effect. Moreover, although Gu and Wu proposed a vibronic barrier model to interpret the Raman process, the relationship between the barriers (ℏω) and the molecular structure has not been explicitly correlated. Here, we use the trifluoromethyl group to systematically substitute the methyl groups in the axial position of the parental bis-butoxide pentagonal-bipyramidal dysprosium(III) SMM - [Dy(OᵗBu)₂(py)₅][BPh₄]. The resulting complexes - [Dy(OL^A)₂py₅][BPh₄ (L^A = CH(CF₃)₂⁻ **1**, CH₂CF₃⁻ **2**, CMe₂CF₃⁻ **3**)- show progressively enhanced T_B^{hys} (@100 Oe/s) from 17 K (for **3**), 20 K (for **2**) to 23 K (for **1**). As the gradually enhanced averaged vibration energy generated by different axial ligands from 230 cm⁻¹ (for **3**), 257 cm⁻¹ (for **2**) to 321 cm⁻¹ (for **1**) was identified experimentally and theoretically to be the only variant that leads to this improvement, this finding unambiguously reveals, for the first time, the correlation between structural change and the multi two-phonon (Raman) relaxation processes in lanthanide-based SMMs and highlights the importance of controlling the relevant vibrations in building SMMs with higher blocking temperatures.*

Single-molecule magnets (SMMs) are a kind of molecular material with a molecular origin of nanomagnetism that have been widely explored in the fields of miniature spintronics, quantum bits and ultrahigh dense information storage.[1–3] Owing to a large unquenched orbital momentum as well as a high magnetic anisotropy, dysprosium(III) ion has emerged as an optimal candidate for building high-performance SMMs.[4–14] The design principles were long focusing on enhancing the axial crystal field potential while weakening the equatorial one, aiming to increase the so-called effective energy barrier U_{eff}.[15–16] Previously, our group reported a near-perfect pentagonal-bipyramidal dysprosium(III) complex - [Dy(OᵗBu)₂(py)₅][BPh₄] (**4**) with a huge U_{eff} of 1815 K.[7] Later, U_{eff} is further lifted by other SMMs, e.g., [(Cp^{iPr5})Dy(Cp*)][B(C₆F₅)₄], [Dy(Cp^{iprR})][B(C₆F₅)₄] (R = H, Me, Et, iPr) and [Dy(OᵗBu)₂(4-phenylpyridine)₄][Na(BPh₄)₂], which show U_{eff} > 2000 K.[10,11,17] However, despite these accomplishments, the improvements of the blocking temperature (T_B) in SMMs are much lagged compared to the expectations from the largely raised U_{eff}.[18]

There are three generally used definitions for T_B, namely, the temperature with maximized zero-field cooled (ZFC) magnetization (T_B^{ZFC}); the temperature with a relaxation time of 100 seconds (T_B^{100s}); and the temperature with visible hysteresis loops (T_B^{hys}). The first two definitions are more widely used in traditional superparamagnetism.[19] Regardless of which definition further enhances T_B, an in-depth understanding of the magnetostructural correlation is fundamentally critical. For most Dy^{III}-based SMMs, the reversal of magnetic moments actually involves three types, namely, quantum tunnelling and one- and two-phonon processes.[20,21] The last one is usually further divided into Orbach and Raman processes according the energy levels, which are real and virtual, respectively.[22,23] For the former, by comparing the relaxation between [Dy((S)-(-)-1-phenylethanol)₂(py)₅][BPh₄] and **4**, our group found that the intramolecular C–H⋯π and intermolecular π⋯π interactions can enhance the relaxation times in the region of the Orbach regime, which was similar to the conclusion that the vibrational motion of the C–H groups on the Cp^{ttt} ligands can facilitate the Orbach relaxation step in the [Dy(Cp^{ttt})₂][B(C₆F₅)₄] complex.[8,24] For the latter, the anomalously small Raman exponent (*n*) has puzzled the field for a long time. This is due to the lack of understanding of molecular systems compared to inorganic solids.[25] Recently, more theoretical evidence showed that the Raman process was actually due to the contribution from a series of vibrational modes under magnetic spin reversal barriers.[26–32]

In addition to the introduction of intra- and intermolecular interactions to stiffen the molecule, the introduction of terminal F⁻ ions in the related molecular solids has been proven to be useful for enhancing the stability and axial crystal-field strength (CFS) of dysprosium(III) complexes.[33–35] In addition, the fluoride ligands used as equatorial ligands can reduce transversal CFS due to the with-drawing effects from F⁻ ions.[36–38] However, there is no experimental result to show the effect of swapping C−H bonds with C−F bonds on the Raman process. If we view chemical bonds as a harmonic oscillator system, the stronger C−F bonding energy (485 kJ/mol) over that of the C−H bond (414 kJ/mol) will lead to more optical phonons with higher frequencies,[39-40] which in return reduce the Raman process. The difficulty remains in distinguishing the contribution from the Orbach process. Hence, a system with an almost fixed Orbach process is critical.

Herein, we report a family of Dy(III)-based complexes in pentagonal-bipyramidal geometry with fluorinated axial ligands

to serve as the model for testing vibrational barrier-assisted magnetic relaxation in two-phonon relaxations, including both the Orbach and Raman regions. The complexes were named [DyOL$^A_2$py$_5$][BPh$_4$], where L^A = CH(CF$_3$)$_2^-$ (**1**), CH$_2$CF$_3^-$ (**2**), and CMe$_2$CF$_3^-$ (**3**). Compared with parental complex **4**, the design rule for **1**–**3** is to reduce the methyl protons of the axial ligand (O^{t}Bu$^-$) by introducing trifluoromethyl groups (Scheme 1). For **1**, O^{t}Bu$^-$ is replaced with OCH(CF$_3$)$_2^-$, in which two methyl groups are replaced by trifluoromethyl groups. For **2**, one methyl group is replaced by a trifluoromethyl group, while the other two methyl groups are also removed. For **3**, only one trifluoromethyl group was introduced to replace one methyl group on the O^{t}Bu$^-$ group. Hence, the structures of **1**–**3** are similar except for the axial ligands. Astonishingly, the blocking temperatures are very different, which show much enhanced T_B^{hys} (@100 Oe/s) from 17 K (for **3**), 20 K (for **2**) to 23 K (for **1**). Since U_{eff} and the first-step energy gap of these three complexes are similar, the different dynamic magnetic properties were solely due to the molecular vibrations from different substitutions on the axial ligands. Moreover, the subtle variation in the axial ligand reflected in the absorption bands in the far-IR spectra can be well explained by a newly developed barrier multi two-phonon relaxation model. With detailed vibration modes elaborated from DFT calculations, this work unambiguously validates such a magnetostructural correlation.
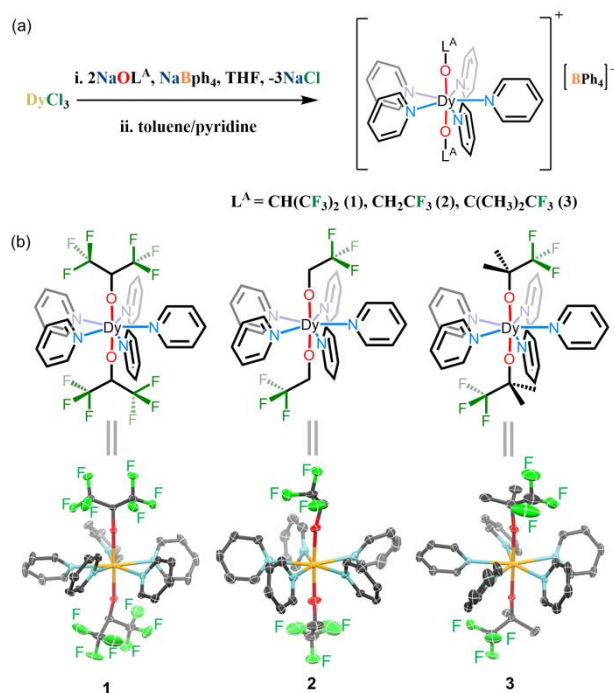

Figure 1. (a) Synthesis of complexes **1**–**3**. (b) Crystal structure of **1**–**3**. Gold, red, sky blue, light green and black spheres represent Dy, O, N, F, and C atoms, respectively. Displacement ellipsoids set at the 40% probability level and hydrogen atoms and [BPh$_4$]$^-$ counteranions are omitted for clarity.

Single-crystal X-ray diffraction studies show complexes **1**–**3** comprise mononuclear cations [DyOL$^A_2$py$_5$]$^+$ (Figure 1), charge-balancing anions BPh$_4^-$ and disordered solvent molecules (Table S1). The [DyOL$^A_2$py$_5$]$^+$ cations for **1**–**3** are similar, with five pyridine molecules coordinated at the equatorial sites and two alkoxide ions at axial positions. Thus, the local Dy(III) ion lies in a pentagonal-bipyramidal coordination geometry (D_{5h})

indicated by the continuous shape measures (CShM) calculations (Table S6).[37] The equatorial Dy–N bonds and axial Dy–O bond lengths vary with different alkoxide ions. Compared to parental complex **4**, all the Dy–O bond lengths become longer, and the longest Dy–O bond distance is observed in **1** with the apical OCH(CF$_3$)$_2^-$ ligand. This is obviously due to the strong electron-sucking effect of the more fluorinated substituents, as also reported in other works.[13] The O–Dy–O angles range from 175.55(7)° to 178.84(7)°, showing slight bending from **1** to **3**. The average N–Dy–N angles are all approximately 72.03(4)° (Tables S2–S5). The shortest intermolecular Dy⋯Dy distances are 9.551(2) Å, 10.115(7) Å and 10.234(5) Å for **1**–**3**, respectively (Figures S1–S3).

Direct current (DC) magnetic susceptibility data were collected for crushed crystals of **1**–**3** from 2 to 300 K under an applied magnetic field of 1000 Oe. At room temperature, the $\chi_m T$ products are 14.09, 13.97 and 14.02 cm^3 mol^{-1} K for **1**–**3** (Figures S4–S6), respectively. These values agree with the expected 14.17 cm^3 mol^{-1} K for free Dy^{3+} (J = 15/2, g = 4/3) ions. Upon cooling, all the $\chi_m T$ products remain nearly constant before starting to drop sharply ca. 20 K, indicating magnetic blocking below this temperature. Alternating current (AC) measurements under zero DC field (Figures S10–S15) show strong temperature and frequency dependencies below 100 K for both in-phase (χ') and out-of-phase (χ'') susceptibility data. Using the generalized Debye model in CC-FIT software (Figures S16–S18),[38] the temperature-dependent magnetic relaxation times τ were obtained and are plotted in Figure S19. Above 60 K, the relaxation rates of all three complexes are exponentially dependent on T, while below 60 K, they become more dependent on T^n, indicating a τ_{switch} of ~ 60 K for all complexes. This inflection point indicates a change from the Orbach to Raman process. As such, the relaxation times were commonly fitted using equation (1):

$$\tau^{-1} = \tau_0^{-1}e^{-U_{eff}/k_BT} + CT^n \qquad (1)$$

which yields the best parameters listed in Table 1. Remarkably, all the U_{eff} values in the Orbach region are almost the same at ~1400 K, which provides excellent model complexes to study the differences in Raman regions.

Table 1. The magnetic fit parameters for **1**–**3**.

	1	2	3
τ_0/s	$3.00(9)\times10^{-12}$	$1.70(6)\times10^{-12}$	$1.88(6)\times10^{-12}$
U_{eff}/K	1430(20)	1400(31)	1446(25)
C/s$^{-1}\cdot$K^{-n}	$5.0(5)\times10^{-8}$	$3.0(4)\times10^{-7}$	$4.0(7)\times10^{-6}$
n	4.5(4)	4.3(5)	3.8(2)
T_B^{ZFC}/K	14.0	10.8	9.8
T_B^{100s}/K	12.0	8.0	3.0
T_B^{hys} (@100 Oe/s)/K	23.0	20.0	17.0
τ_{30K}/s	3.48	1.84	0.58

We further compare the blocking temperatures according to the three definitions mentioned above. Regardless of T_B^{zfc}, T_B^{100s} and T_B^{hys} (@100 Oe/s), the common feature is **3** < **2** < **1** (Figures S7–S9, Tables S8–S10). This tendency is actually manifested in the Raman prevailing region, i.e., at 30 K, the relaxation time already shows a similar relationship (Table 1). We also measured the relaxation time rate using direct-current

magnetization decay down to 2 K, which shows much enhanced relaxation times from 219(44.6) seconds (for **3**), 246(0.5) seconds (for **2**) to 513(1.9) seconds (for **1**), as shown in Figures S24–S26. Hence, the plots of magnetic hysteresis loops at 2 K exhibit different opening shapes, from which we can see that the loop for **1** is the widest, while **3** has the most obvious tunneling feature at zero field (Figure S23). Using a field sweep rate of 100 Oe/s, T_B^{hys} is determined to be 23 K for **1**, 20 K for **2** and 17 K for **3** (Figures S20–S22).

To understand this difference, we focus on the magnetostructural correlation study of these three complexes by terahertz (THz), far-infrared (Far-IR), *ab initio* and DFT calculations using a newly established vibronic-barrier model (*vide infra*). First, the static electronic structures of **1**–**3** were obtained by *ab initio* calculations using complete active space self-consistent field spin-orbit (CASSCF-SO) methods operated by the OPENMOLCAS program.[41] The ground states were calculated with over 99% $|\pm15/2\rangle$ wavefunctions for **1**–**3**, which was due to the strong axial ligand field. The first excited states were found to be composed of over 99% $|\pm13/2\rangle$ with a principal magnetic axis almost parallel to the ground one, resulting in two ideal Ising states. Pure states with over 98% $|\pm11/2\rangle$ were found for the second excited states; however, the principal axis became tilted. The upper excited states were highly mixed by wavefunctions of $|\pm9/2\rangle$ to $|\pm1/2\rangle$ due to the unquenched nonaxial crystal field parameters (Tables S11–S16). The transition pathways between different substates are shown in Figures S28–S30, where we can estimate U_{eff}, determined by the Orbach process, to be in-between the highly bunched excited states, with transitions from the fourth to fifth excited states at 919–939 cm^{-1} for **1** and the same transitions but higher energies at 988–1008 and 989–1013 cm^{-1} for **2** and **3**, respectively (Tables S17–S19). The theoretical predicted U_{eff} values here are very close to the experimental results, thus proving that the axial ligands provide a static crystal field similar to that of the central Dy(III) ions.

For the spin dynamics, apart from the low-temperature quantum tunnelling of magnetization (QTM) and the direct processes, the spin relaxation at higher temperatures is governed by the inelastic scattering of phonons, involving absorption and emission of two single phonons. This is the so-called two-phonon relaxation mechanism, which can be further divided into Orbach and Raman processes. For the Orbach process, Chilton and Lunghi *et al* have individually developed two complete first-principle calculation methods by using the Fermi golden rules, where on-resonant phonons facilitate this process, and succeeded in predicting the relaxation rates in the Orbach process region for some Dy(III) and 3d SMMs systems.[8, 24, 27–30, 43-45] For the Raman process, the relaxation mechanism has long been understood as a high power dependence of temperature under the Debye mode ($\tau_{Raman} = CT^n$), which gave the power $n \sim 9$ for Kramers ion and $n \sim 7$ for non-Kramers ion, while sometimes a slight reduction due to the so-called acoustic-optical mechanism.[42] However, such a mechanism fails in interpreting many large barrier Dy(III) SMMs.[4-14] Recently, Gu *et al* mentioned that the phonons generated by vibrational modes should be responsible for Raman-type relaxations and successfully created a vibronic barrier model (VBM).[30] The core of this model is to upgrade equations (1) to (2) and (3) by introducing different off-resonant vibration modes (phonons).

$$\tau^{-1} = \tau_0^{-1} e^{-U_{eff}/k_B T} + \sum_n \tau_n^{-1} e^{-U_n/k_B T} + \tau_{QTM}^{-1} \qquad (2)$$

$$\begin{cases} \tau_0^{-1} = \dfrac{2\pi |a_0|^2 \rho(U_{eff})}{\hbar U_{eff}} \\ \tau_n^{-1} = \dfrac{|a_n|^2}{U_n \Gamma_n} \end{cases} \qquad (3)$$

where τ_0 and τ_n are the prefactors, a_0 is the spin-phonon transition matrix element from the ground to excited states, U_{eff} is the effective energy barrier, $\rho(U_{eff})$ is the phonon density of states (DOS), $\hbar$ is the reduced Planck constant, a_n is the spin-phonon transition matrix element within the ground Kramers doublet (KD), U_n is the energy of the vibration mode and Γ_n is the broadening width. Unlike the power law in equation (1), the new relaxation mechanism introduces the contributions of phonons from the molecular vibrations at temperatures lower than the energy gap of the magnetic structure; that is, in addition to the Orbach process being associated with on-resonant phonons, the Raman process also complies with a real physical meaning following $e^{-U_n/k_B T}$ ($U_n = \hbar\omega$) for a mode of frequency ω.

Gu *et al.* have previously applied VBM to two 3d SMMs. One is the complex [tpa^{Ph}Fe]$^{-1}$ with U_{eff} = 26 cm^{-1},[31] and the other is the complex (HNEt$_3$)$_2$[Co(L$_2$)$_2$] (H$_2$L = 1,2-bis(methanesulfonamido)benzene) with U_{eff} = 230 cm^{-1}.[26] For the former, the investigated phonons are below 26 cm^{-1}; thus, only the four lowest vibrational mode energies ranging from 20–27 cm^{-1} are involved in characterizing the exponential relation with the Raman relaxation barriers. However, for the latter, the zero-field splitting (zfs) is large, and there are 24 vibrational modes with energies lower than the Orbach barrier involved. Thus, the fitting process is much more complicated and has the risk of overparameterization. We can expect that once this model is applied for Dy(III)-based SMMs with even larger energy barriers, the related phonons could be overwhelmed.

Table 2. The magnetic fitting parameters for **1**–**3** with equation (2).

		1	2	3
Orbach process	τ_0/s	3.00×10^{-12}	1.70×10^{-12}	1.88×10^{-12}
	U_0/K	1430	1400	1446
Raman process	τ_R/s	0.013(3)	0.005(7)	0.0028(5)
	U_R/cm^{-1}	180(2)	175(3)	170(1)
Band III	τ_3/s	1.9(2)×10^{-4}	1.2(1)×10^{-4}	2.1(4)×10^{-4}
	U_3/cm^{-1}	439	439	439
Band II	τ_2/s	0.009(2)	0.002(1)	0.001(1)
	U_2/cm^{-1}	321	257	230
Band I	τ_1/s	0.06(2)	0.04(1)	0.03(2)
	U_1/cm^{-1}	121	126	125

However, here, we show that by combining THz and far-IR spectroscopy, we can identify as many barrier phonons as possible and avoid overparameterization in the following fitting process. First, from the *ab initio* calculation mentioned above, the energy lifting from the ground to the first excited m_J states was approximately 500 cm^{-1} for the three complexes. Hence, most of the under-barrier phonons mediating Raman processes have energies below 500 cm^{-1}, as shown in Figure 2a. We then expect to observe these phonons in the vibration spectroscopy

in this energy range. To determine these phonons, we used two Arrhenius plots, one for the high-temperature region above 60 K and the other for the low-temperature region below 50 K, to obtain a reliable Orbach process (τ_0 and U_0) and average phonon energy involved in the Raman process (τ_R and U_R), respectively. The fitting results for **1–3** (Table 2 and Figure S27) give almost identical Orbach process parameters while significantly different τ_R and U_R values. As U_R is the average energy of the under barrier phonons we then focus on what causes this difference. For vibration energy below 500 cm^{-1} is the region of THz and Far-IR we did the measurements for **1–3.**

The THz spectra in the energy range of 5–110 cm^{-1} were recorded by time-domain transmission spectroscopy (THz-TD)

on powder samples of **1–3**. In this frequency range, all three complexes display almost identical absorption peaks (Figure 2b), indicating that the low-energy vibrations are almost the same for **1–3**. Usually, these vibrations belong to acoustic phonons from the lattice, where low-frequency phonons are formed by stimulated Brillouin scattering following the Debye model. In addition to the similarities, the intensities of acoustic phonons below 80 cm^{-1} are ca. ten times lower compared to the optical ones observed in the Far-IR region (see below). Hence, we can safely conclude that the Far-IR active vibrations should contribute the most to the Raman process.
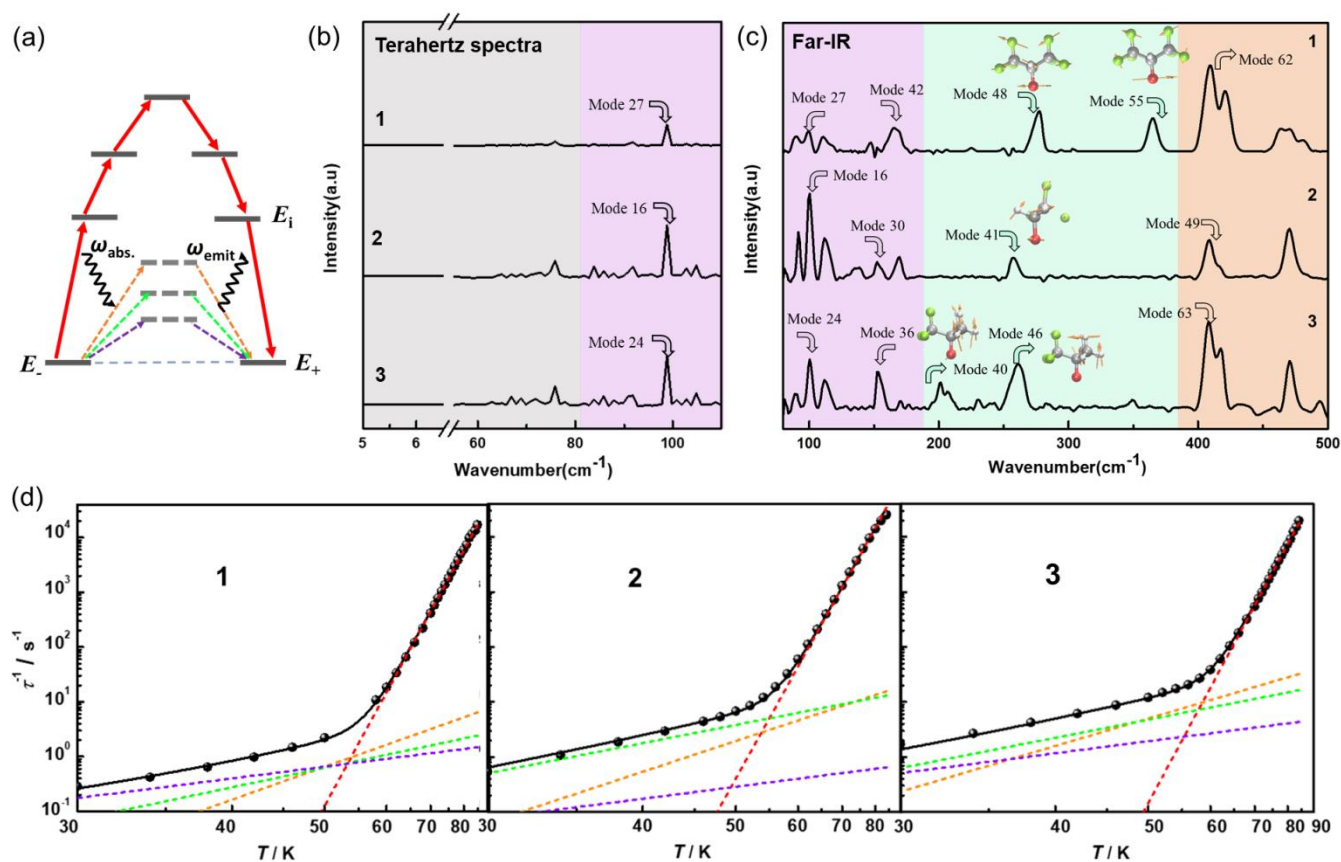

Figure 2. (a) Resonant two-phonon relaxation process (red solid lines) and vibranic barrier two-phonon relaxation process (dotter lines); (b) Experimental THz spectra in the range of 5–110 cm^{-1} for **1–3**; (c) Experimental far-IR spectra in the range of 80–500 cm^{-1} for **1–3**; (d) Experimental relaxation rates (black dots) and simulations with two-phonon relaxation processes (red, orange, green and violet dashed lines for Orbach process, Band III, Band II and Band I, respectively) for **1–3**.

The Far-IR spectra in the frequency range of 80−500 cm^{-1} show discrete peaks distinct from the Debye nature for three complexes (Figure 2c). Interestingly, the absorption spectra in this frequency range can be divided into three zones (indicated in different background colors in Figure 2c) for all the three complexes. For **1**, the lowest energy zone (Band I) ranging from 90 cm^{-1} to 164 cm^{-1} belongs to the vibration modes of 26, 27, 28, 38 and 42 (see Figures S40–S44 in Supporting Information), which arise from a mixture of stretching vibrations of Dy–O and Dy–N bonds and torsional vibrations of OCH(CF$_3$)$_2$$^-$ and pyridine ligands. The averaged phonon for this band (U_1) is thus

determined to be 121 cm^{-1}. The intermediate energy zone (Band II) possesses two phonons with energies of 277 and 365 cm^{-1} belonging to modes 48 and 55, respectively, which arise from the local bending or stretching of the C−F bonds in the axial OCH(CF$_3$)$_2$$^-$ ligand (Figures S45–46). Thus, U_2 is determined to be 321 cm^{-1} (averaged energy for Band II). The highest absorption peak at 408 and 470 cm^{-1} (Band III) are calculated to be from modes 62 and 65, which arise from the C−H bending of the pyridine rings (Figures S47–48). Hence, U_3 is determined to be 439 cm^{-1}. Then, these determined values of U_1, U_2, U_3, τ_0 and U_0 are used as fixed values in the final fitting by using

4

equation (2). To this end, the variables are reduced to just three prefactors (τ_1, τ_2 and τ_3), which effectively avoids overparameterization during the fitting and yields the very good results listed in Table 2 and plotted in Figure 2d. Similar processes can be used to determine U_n and τ_n for both **2** and **3**. Interestingly, we found an identical U_3 of 439 cm^{-1} and almost identical U_1 values for all three complexes (Table 2). According to our DFT analysis, these two bands reflect the vibrations of C–H bending of the pyridine rings (Figures S56, S57, S65 and S66) and a mixture of stretching vibrations of Dy–O and Dy–N bonds (Figures S49–S54 and S58–S62). These similarities for U_3 and U_1 are thus accountable. However, the peaks at the medium energy bands show disparate locations. The absorption peak at the medium energy band (Band II) only shows one at 257 cm^{-1}, which belongs to vibration mode 41 arising from the C−F bond bending of the axial OCH$_2$CF$_3^-$ ligand (Figure S55). Owing to the much reduced C−F bonds in the axial ligand compared to **1**, the U_2 = 257 cm^{-1} for **2** is significantly lower than that of **1**. For **3**, the medium energy band is characterized by peaks at 200 cm^{-1} and 260 cm^{-1} (Figures S63–64), belonging to the 40 and 46 vibration modes of the axial OCMe$_2$CF$_3^-$ ligand, which means that U_2 is significantly reduced to 230 cm^{-1} due to the further reduction of C−F bonding numbers.

From the above analysis of the Far-IR spectra we can discern the only variant to cause the difference in τ_R and U_R is the medium frequency range of 200–350 cm^{-1}, which correspond to the "fingerprints" of C−F bond vibrations. Using these limited U_n and τ_n values we can nicely reproduce the relaxation plots below the τ_{switch} (Figure 2d), where Raman relaxation processes dominate. This reveals that the replacement of the C−H bond with the C−F bond resulting in higher energy of the bending or stretching vibrations in the regime of 200–350 cm^{-1} is essential to mitigate the Raman relaxation processes in these complexes. However, without the experimental identification of U_1, U_2 and U_3, such a fitting by using equations (2) and (3) would be definitely overparameterized. In that sense, we found a way to manifest the chemical meaning of $\hbar\omega$ in the vibronic barrier model.[31]

In summary, by fixing the equatorial pyridine ligands and the counteranions of the pentagonal-bipyramidal dysprosium(III) SMMs we stepwise fluorinated the axial alkoxide ligands, which effectively mitigate the under barrier Raman processes. The T_B^{hys} (@100 Oe/s) is progressively enhanced from 17 K (for **3**), 20 K (for **2**) to 23 K (for **1**). Taking the advantage of nearly identical energy gap between the ground and first excited states of these three complexes, we are able to rationalize the difference of Raman relaxation rates among these three complexes by using a combined THz, Far-IR spectra and a newly developed vibronic barrier model by Gu et al.[31] This allows us to directly correlate, for the first time, the Raman relaxation barriers to the vibration modes of the ligands. As Far-IR spectrum is commonly accessible we believe that such a treatment can be readily used to help screen ligands with unwanted vibrations.

Acknowledgements

References

1. R. Sessoli, D.Gatteschi, A. Caneschi, M. A. Novak, *Nature* **1993**, *365*, 141–143.
2. M. N. Leuenberger and D. Loss, *Nature*, **2001**, *410*, 789–793.
3. F. D. Natterer, K. Yang, W. Paul, P. Willke, T. Choi, T. Greber, A. J. Heinrich and C. P. Lutz, *Nature*, **2017**, *543*, 226–228.
4. J.-L. Liu, Y.-C. Chen, Y.-Z. Zheng, W.-Q. Lin, L. Ungur, W. Wernsdorfer, L. F. Chibotaru and M.-L. Tong, *Chem. Sci.*, **2013**, *4*, 3310–3316.
5. Y.-C. Chen, J.-L. Liu, L. Ungur, J. Liu, Q.-W. Li, L.-F. Wang, Z.-P. Ni, L. F. Chibotaru, X.-M. Chen and M.-L. Tong, *J. Am. Chem. Soc.*, **2016**, *138*, 2829–2837.
6. S. K. Gupta, T. Rajeshkumar, G. Rajaraman and R. Murugavel, *Chem. Sci.*, **2016**, *7*, 5181–5191.
7. Y. -S. Ding, N. F. Chilton, R. E. Winpenny and Y. -Z. Zheng, *Angew. Chem., Int. Ed.*,**2016**, *55*, 16071–16074.
8. C. A. P. Goodwin, F. Ortu, D. Reta, N. F. Chilton and D. P. Mills, *Nature*, **2017**, *548*, 439–442.
9. K. L. M. Harriman, J. L. Brosmer, L. Ungur, P. L. Diaconescu and M. Murugesu, *J. Am. Chem. Soc.*, **2017**, *139*, 1420–1423.
10. K. Randall McClain, C. A. Gould, K. Chakarawet, S. J. Teat, T. J. Groshens, J. R. Long and B. G. Harvey, *Chem. Sci.*, **2018**, *9*, 8492–8503
11. F. S. Guo, B. M. Day, Y. C. Chen, M. L. Tong, A. Mansikkamaki and R. A. Layfield, *Science*, **2018**, *362*, 1400–1403.
12. P. -B. Jin, Y. -Q. Zhai, K. -X. Yu, R. E. P. Winpenny and Y. -Z. Zheng, *Angew. Chem., Int. Ed.*, **2020**, *59*, 9350–9354.
13. Z. Zhu, Y.-Q. Zhang, X.-L. Li, M. Guo, J. Lu, S. Liu, R. A. Layfield and J. Tang, *CCS Chemistry*, **2021**, *3*, 388–398.
14. J. Long, A. O. Tolpygin, D. M. Lyubov, N. Y.. Rad'kova, A. V. Cherkasov, Y. V. Nelyubina, Y. Guari, J. Larionova and A. A. Trifonov, *Dalton Trans.*, **2021**, *50*, 8487–8496.
15. J. D. Rinehart and J. R. Long, *Chem. Sci.*, **2011**, *2*, 2078–2085.
16. S. T. Liddle and J. van Slageren, *Chem. Soc. Rev.*, **2015**, *44*, 6655–6669.
17. X. L. Ding, Y. Q. Zhai, T. Han, W. P. Chen, Y. S. Ding and Y. Z. Zheng, *Chem. Eur. J.,* **2021**, *27*, 2623–2627.
18. J. L. Liu, Y. C. Chen and M. L. Tong, *Chem. Soc. Rev.*, **2018**, *47*, 2431–2453.
19. D. Gatteschi, R. Sessoli, J. Villain, *Molecular Nanomagnets*, Oxford University Press, **2006**
20 R. J. Blagg, L. Ungur, F. Tuna, J. Speak, P. Comar, D. Collison, W. Wernsdorfer, E. J. L. McInnes, L. F. Chibotaru and R. E. P. Winpenny, *Nat. Chem.*, **2013**, *5*, 673–678.
21. Y. Xu, J.-S.Wang,W. Duan, B.-L. Gu, and B. Li, *Phys. Rev. B.*,**2008**, *78*, 224303 .
22. S. T. Liddle and J. van Slageren, *Chem. Soc. Rev.*, **2015**, *44*, 6655–6669.
23. R. Orbach, Proc. R. Soc. *London, Ser. A*, **1961**, *264*, 458–484.

24. K. X. Yu, J. G. C. Kragskow, Y. S. Ding, Y. Q. Zhai, D. Reta, N. F. Chilton and Y. Z. Zheng, *Chem*, **2020**, *6*, 1777–1793.

25. Y. S. Ding, T. Han, Y. Q. Zhai, D. Reta, N. F. Chilton, R. E. P. Winpenny and Y. Z. Zheng, *Chem. Eur. J.,* **2020**, *26*, 5893–5902.

26. L. Gu and R. Wu, *Phys. Rev. B.*, **2021**, *103*, 01440.

27. M. Briganti, F. Santanni, L. Tesi, F. Totti, R. Sessoli, A. Lunghi, *J. Am. Chem. Soc.* **2021**, *143*, 13633-13645.

28. A. Lunghi, F. Totti, S. Sanvito and R. Sessoli, *Chem. Sci.*, **2017**, *8*, 6051–6059

29. A. Lunghi, F. Totti, R. Sessoli and S. Sanvito, *Nat. Commun.*, **2017**, *8*, 14620.

30. A. Lunghi and S. Sanvito, *Science Advances*, **2019**, *5*, eaax7163;

31. L. Gu and R. Wu, *Phys. Rev. Lett.*, **2020**, *125*, 117203

32. A. Lunghi and S. Sanvito, *J Chem Phys*, **2020**, *153*, 174113.

33. L. Norel, L. E. Darago, B. Le Guennic, K. Chakarawet, M. I. Gonzalez, J. H. Olshansky, S. Rigaut and J. R. Long, *Angew. Chem., Int. Ed.*, **2018**, *57*, 1933–1938.

34. B.-K. Ling, Y.-Q. Zhai, J. Han, T. Han, Y.-Z. Zheng, *Dalton Trans.*, **2020**, *49*, 6969–6973.

35. A. B. Canaj, M. K. Singh, E. Regincos Marti, M. Damjanovic, C. Wilson, O. Cespedes, W. Wernsdorfer, G. Rajaraman and M. Murrie, *Chem. Commun.*, **2019**, *55*, 5950–5953.

36. F. Habib, G. Brunet, V. Vieru, I. Korobkov, L. F. Chibotaru, M. Murugesu, *J. Am. Chem. Soc.* **2013**, *135*, 13242–13245.

37. Z. Zhu, C. Zhao, T. Feng, X. Liu, X. Ying, X.-L. Li, Y.-Q. Zhang, J. Tang, *J. Am. Chem. Soc.* **2021**, *143*, 10077–10082.

38. L. Zhu, B. Yin, P. Ma, D. Li, *Inorg. Chem.* **2020**, *59*, 16117-16121.

39. R. T. Sanderson, in *Polar Covalence* (Ed.: R. T. Sanderson), Academic Press, **1991**, pp. 13-34.

40 R. Minkwitz, S. Reinemann, *Zeitschrift fur Anorganische und Allgemeine Chemie* **1998**, *624*, 1695-1698.

41. M. V. Ignacio Fdez. Galván, Ali Alavi, Celestino Angeli, Francesco Aquilante, Jochen Autschbach, Jie J. Bao, Sergey I. Bokarev, Nikolay A. Bogdanov, Rebecca K. Carlson, Liviu F. Chibotaru, Joel Creutzberg, Nike Dattani, Mickaël G. Delcey, Sijia S. Dong, Andreas Dreuw, Leon Freitag, Luis Manuel Frutos, Laura Gagliardi, Frédéric Gendron, Angelo Giussani, Leticia González, Gilbert Grell, Meiyuan Guo, Chad E. Hoyer, Marcus Johansson, Sebastian Keller, Stefan Knecht, Goran Kovačević, Erik Källman, Giovanni Li Manni, Marcus Lundberg, Yingjin Ma, Sebastian Mai, João Pedro Malhado, Per Åke Malmqvist, Philipp Marquetand, Stefanie A. Mewes, Jesper Norell, Massimo Olivucci, Markus Oppel, Quan Manh Phung, Kristine Pierloot, Felix Plasser, Markus Reiher, Andrew M. Sand, Igor Schapiro, Prachi Sharma, Christopher J. Stein, Lasse Kragh Sørensen, Donald G. Truhlar, Mihkel Ugandi, Liviu Ungur, Alessio Valentini, Steven Vancoillie, Valera Veryazov, Oskar Weser, Tomasz A. Wesołowski, Per-Olof Widmark, Sebastian Wouters, Alexander Zech, J. Patrick Zobel, and Roland Lindh, *J. Chem. Theory Comput.*, **2019**, *15*, 5925–5964.

42. M. Blume and R. Orbach, *Phys. Rev.*, **1962**, *127*, 1587–1592.

43. M. Briganti, F. Santanni, L. Tesi, F. Totti, R. Sessoli and A. Lunghi, *J. Am. Chem. Soc.*, **2021**, *143*, 13633–13645.

44. A. Chiesa, F. Cugini, R. Hussain, E. Macaluso, G. Allodi, E. Garlatti, M. Giansiracusa, C. A. P. Goodwin, F. Ortu, D. Reta, J. M. Skelton, T. Guidi, P. Santini, M. Solzi, R. De Renzi, D. P. Mills, N. F. Chilton and S. Carretta, *Phys. Rev. B*, **2020**, *101*, 174402.

45. D. Reta, J. G. C. Kragskow, N. F. Chilton, *J. Am. Chem. Soc.* **2021**, *143*, 5943-5950.

6

Entry for the Table of Contents
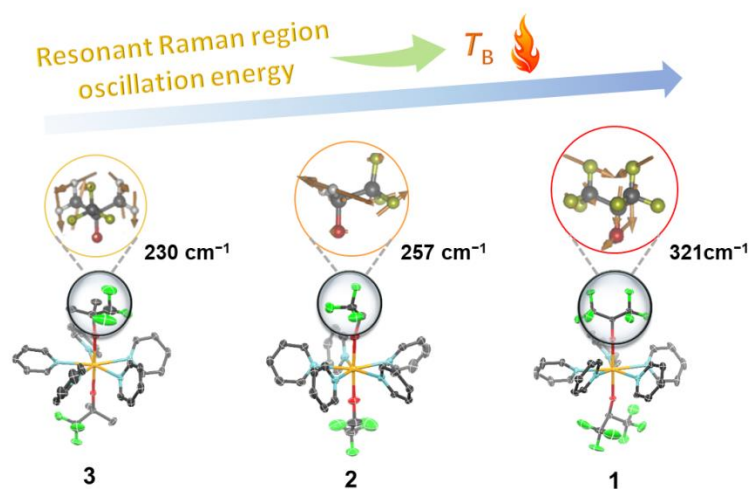
Here, we show that fluorination at the axial position of pentagonal-bipyraimdal dysprosium(III) single-molecule magnets effectively reduces the anharmonic phonon-assisted Raman relaxation process, as validated by THz, far-IR, *ab initio* and DFT calculations using a newly established vibronic-barrier model.

Ligand Fluorination to Mitigate the Raman Relaxation of Dy(III) Single-Molecule Magnets: A Combined Terahertz, Far-IR and Vibronic Barrier Model Study

Yan Ma[†], Yuan-Qi Zhai[†], Qian-Cheng Luo, You-Song Ding and Yan-Zhen Zheng*

[*] Frontier Institute of Science and Technology (FIST), State Key Laboratory for Mechanical Behaviour of Materials, MOE Key Laboratory for Nonequilibrium Synthesis of Condensed Matter, Xi'an Key Laboratory of Sustainable Energy and Materials Chemistry,Xi'an Jiaotong University, 99 Yanxiang Road, Xi'an, Shaanxi 710054, P. R. China.

[†]These authors contributed equally to this work.

Corresponding email:zheng.yanzhen@xjtu.edu.cn.

Contents

1. General Procedures

All air- and moisture-sensitive experiments were performed under a dry and oxygen-free argon atmosphere in a glovebox. All solvents were purified by standard methods and distilled prior to use. Anhydrous dysprosium chloride was prepared according to the literature procedures.[1] 2,2,2-trifluoroethanol, 2-trifluoromethyl-2-propanol, 1,1,1,3,3,3-hexafluoro-2-propanol and sodium tetraphenylbororate are commercially available and were used without further treatment. Elemental analyses were carried out by an EA3000 Automatic Elemental Analyzer at the Instrument Analysis Center of Xi'an Jiaotong University with Dr Chang Gang's assistance. IR spectra were collected on a Thermo Fisher Nicolet 6700 FTIR spectrometer fitted with a Platinum ATR module. Far-IR spectra were collected on a Thermo Scientific Nicolet iS50 FTIR spectrometer.

2. Synthesis

Synthesis of [Dy(OCH(CF$_3$)$_2$)$_2$py$_5$][BPh$_4$] (1): A mixture of DyCl$_3$ (0.5 mmol, 0.13 g), NaOCH(CF$_3$)$_2$ (1 mmol, 0.10 g) and NaBPh$_4$ (0.5 mmol, 0.17 g) was reacted at 85 °C in 8 mL THF for 12 hours to form a cloudy solution, which was filtered, and then the solvent was under vacuum to give a white powder. The powder was washed three times with a mixture of toluene and hexane (1:1) and then dissolved in 3 mL pyridine. The pyridine solution was layered with 7 mL of hexane and stored at -35 °C, which gave crystals in good yield (348 mg, 53.4% based on Dy). Elemental analysis calcd (%) for **1**: C 57.13, H 4.22, N 5.37; found: C 56.27, H 4.27 N 5.85. IR spectra (cm^{-1}): 3054w, 1587m, 1482m, 1437m, 1282m, 1213w, 1149w, 1067w, 1031m, 994w, 843w, 746m, 732m, 699s.

Synthesis of [Dy(OCH$_2$CF$_3$)$_2$py$_5$][BPh$_4$] (2) The synthesis was the same as **1**, except that NaOCH(CF$_3$)$_2$ was replaced by NaOCH$_2$CF$_3$ (Yield, 285 mg, 48.5% based on Dy). Elemental analysis calcd (%) for **2**: C 58.97, H 4.91, N 6.48; found: C 57.25, H 4.30 N 6.20. IR spectra (cm^{-1}): 3056w, 1598m, 1483m, 1442m, 1271m, 1215w, 1152w, 1136w, 1068w, 1037m, 1006m, 957m, 844w, 745m, 733m, 698s, 672m.

Synthesis of [Dy(OC(CH$_3$)$_2$CF$_3$)$_2$py$_5$][BPh$_4$] (3) The synthesis was the same as **1**, except that NaOCH(CF$_3$)$_2$ was replaced by NaOC(CH$_3$)$_2$CF$_3$ (Yield, 335 mg, 59.3% based on Dy). Elemental analysis calcd (%) for **3**: C 60.51, H 5.64, N 6.19; found: C 60.23, H 5.48 N 6.08. IR spectra (cm^{-1}): 3055w, 1598m, 1481m, 1443m, 1378w, 1312w, 1206m, 1134w, 1118m, 1067w, 1036m, 1005m, 989w, 876w, 749m, 733m, 700s.

3. X-ray Crystallography Data

The diffraction data for **1–3** were collected at 150 K on a Bruker SMART CCD diffractometer with MoKα radiation (λ = 0.71073 Å). The structures were solved by direct methods and were refined by full-matrix least-squares on all unique F^2 values, with anisotropic displacement parameters for all nonhydrogen atoms. SHELXTL[2, 3], and OLEX2[4] were employed for structure solution and refinement.

Table S1. Crystal data and structure refinement for **1**–**3**.

	1	2	3
Formula	$C_{65}H_{56}BDyF_{12}N_7O_2$	$C_{53}H_{53}BDyF_6N_5O_2$	$C_{57}H_{57}BDyF_6N_5O_2$
F.w(g mol^{-1})	1368.49	1179.32	1131.39
T(K)	150	150	150
Space group	P-1	$P2_1/c$	P-1
a/Å	10.114(3)	32.585(7)	11.5906(17)
b/Å	17.242(5)	17.973(4)	16.476(3)
c/Å	18.477(5)	19.027(4)	17.857(3)
α/°	74.161(4)	90	94.577(2)
β/°	88.977(4)	90.193(3)	107.8770(19)
γ/°	87.368(4)	90	106.5645(19)
V(Å)^3	3096.4(15)	11143(4)	3058.0(8)
Z	2	8	2
ρ_c(g/cm^3)	1.468	1.423	1.311
F(000)	1380.0	4848.0	1230.0
Reflns collected	33617	104536	45975
R_1(>2σ/all data)	0.0288/0.0365	0.0535/0.0739	0.0364/0.0400
wR_2(>2σ/all data)	0.0658/0.0690	0.1144/0.1249	0.1003/0.1031
GOF	1.047	1.052	1.100
Residues(e Å^{-3})	1.23/-0.31	2.38/-1.65	2.04/-0.94

Table S2. Selected bond lengths (Å) and angles (deg) in complex **1**.

Dy(1)–O(1)	2.1216(17)	Dy(1)–O(2)	2.1422(18)
Dy(1)–N(1)	2.582(2)	Dy(1)–N(2)	2.555(2)
Dy(1)–N(3)	2.529(2)	Dy(1)–N(4)	2.590(2)
Dy(1)–N(5)	2.538(2)		
O(1)–Dy(1)–O(2)	178.84(7)		
O(1)–Dy(1)–N(1)	88.42(7)	O(2)–Dy(1)–N(1)	92.42(7)
O(1)–Dy(1)–N(2)	93.80(7)	O(2)–Dy(1)–N(2)	87.24(7)
O(1)–Dy(1)–N(3)	91.69(7)	O(2)–Dy(1)–N(3)	88.137(7)
O(1)–Dy(1)–N(4)	90.30(7)	O(2)–Dy(1)–N(4)	88.55(7)
O(1)–Dy(1)–N(5)	89.83(7)	O(2)–Dy(1)–N(5)	89.72(7)
N(2)–Dy(1)– N(1)	70.54(7)	N(2)–Dy(1)–N(3)	71.86(7)
N(3)–Dy(1)–N(4)	74.57(7)	N(5)–Dy(1)–N(4)	73.75(7)
N(5)–Dy(1)–N(1)	69.38(7)		

Table S3. Selected bond lengths (Å) and angles (deg) in complex **2**.

Dy(1)–O(1)	2.114(4)	Dy(1)–O(2)	2.120(12)
Dy(1)–N(1)	2.554(5)	Dy(1)–N(2)	2.534(5)
Dy(1)–N(3)	2.548(5)	Dy(1)–N(4)	2.536(5)
Dy(1)–N(5)	2.518(5)		
O(1)–Dy(1)–O(2)	175.77(17)		
O(1)–Dy(1)–N(1)	89.83(18)	O(2)–Dy(1)–N(1)	91.39(18)
O(1)–Dy(1)–N(2)	94.37(18)	O(2)–Dy(1)–N(2)	89.86(19)
O(1)–Dy(1)–N(3)	88.28(17)	O(2)–Dy(1)–N(3)	93.29(18)
O(1)–Dy(1)–N(4)	88.98(7)	O(2)–Dy(1)–N(4)	87.74(18)
O(1)–Dy(1)–N(5)	89.03(16)	O(2)–Dy(1)–N(5)	87.46(17)
N(2)–Dy(1)– N(1)	71.06(18)	N(4)–Dy(1)–N(3)	72.67(17)
N(2)–Dy(1)–N(3)	70.65(18)	N(5)–Dy(1)–N(1)	72.62(17)
N(5)–Dy(1)–N(4)	73.24(16)		

Table S4. Selected bond lengths (Å) and angles (deg) in complex **3**.

Dy(1)–O(1)	2.115(2)	Dy(1)–O(2)	2.126(2)
Dy(1)–N(1)	2.573(3)	Dy(1)–N(2)	2.579(3)
Dy(1)–N(3)	2.557(3)	Dy(1)–N(4)	2.572(3)
Dy(1)–N(5)	2.592(3)		
O(1)–Dy(1)–O(2)	175.55(9)		
O(1)–Dy(1)–N(1)	91.47(9)	O(2)–Dy(1)–N(1)	92.45(11)
O(1)–Dy(1)–N(2)	94.80(9)	O(2)–Dy(1)–N(2)	88.58(10)
O(1)–Dy(1)–N(3)	88.27(8)	O(2)–Dy(1)–N(3)	90.12(9)
O(1)–Dy(1)–N(4)	87.70(8)	O(2)–Dy(1)–N(4)	87.86(10)
O(1)–Dy(1)–N(5)	90.67(8)	O(2)–Dy(1)–N(5)	88.60(9)
N(2)–Dy(1)– N(1)	68.92(9)	N(4)–Dy(1)–N(3)	73.89(8)
N(2)–Dy(1)–N(3)	70.75(8)	N(5)–Dy(1)–N(1)	71.08(8)
N(5)–Dy(1)–N(4)	75.53(8)		

Table S5. Comparison of selected structural parameters for complex **1**–**4**. (bond lengths (Å) and angles (deg)).

	1	2	3	4
Dy(1)–O(1)	2.1216(17)	2.114(4)	2.115(2)	2.114(2)
Dy(1)–O(2)	2.1422(18)	2.120(12)	2.126(2)	2.110(2)
Dy(1)–N(1)	2.582(2)	2.554(5)	2.573(3)	2.534(3)
Dy(1)–N(2)	2.555(2)	2.534(5)	2.579(3)	2.556(3)
Dy(1)–N(3)	2.529(2)	2.548(5)	2.557(3)	2.563(3)
Dy(1)–N(4)	2.590(2)	2.536(5)	2.572(3)	2.572(3)
Dy(1)–N(5)	2.538(2)	2.518(5)	2.592(3)	2.580(3)
Dy–N(average)	2.558	2.538	2.574	2.561
O(1)–Dy(1)–O(2)	178.84(7)	175.77(17)	175.55(9)	178.91(9)

Table S6. Continuous Shape Measures calculations (CShM) for **1–3**.

Complex	HP-7 (D_{7h})	HPY-7 (C_{6V})	PBPY-7 (D_{5h})	COC-7 (C_{3V})	CTPR-7 (C_{3V})	JPBPY-7 (D_{5h})	JETPY-7 (C_{3V})
1	33.094	23.676	0.730	7.880	6.036	1.369	24.028
2	33.457	23.794	0.725	7.573	5.872	1.373	24.088
3	33.321	23.245	0.866	7.682	5.841	1.323	23.406

HP-7 = Heptagon; HPY-7 = Hexagonal pyramid; PBPY-7 = Pentagonal bipyramid; COC-7 = Capped octahedron; CTPR-7 =Capped trigonal prism; JPBPY-7 = Johnson pentagonal bipyramid J13; JETPY-7 = Johnson elongated triangular pyramid J7.
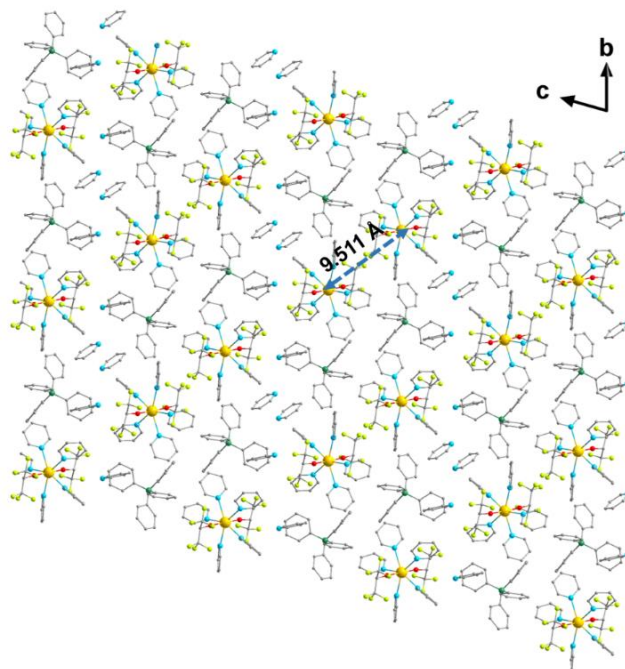

Figure S1. The packing diagram of **1** viewed along the *a* axis. Hydrogen atoms are omitted for clarity.
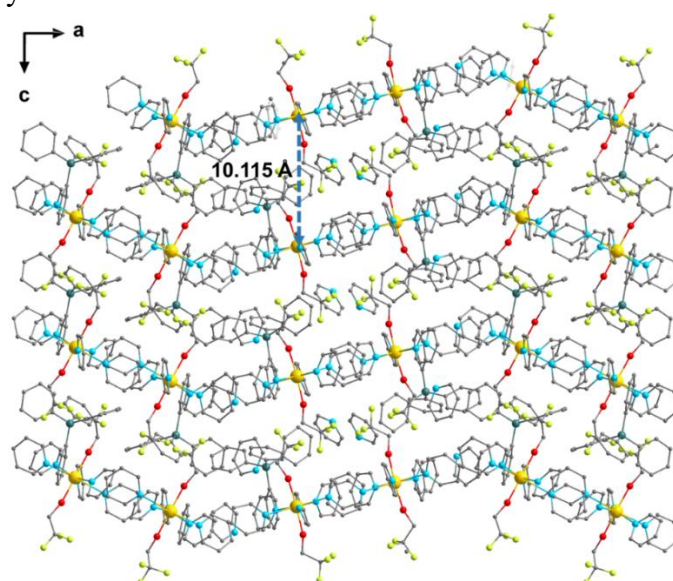
Figure S2. The packing diagram of **2** viewed along the *b* axis. Hydrogen atoms are omitted for clarity.
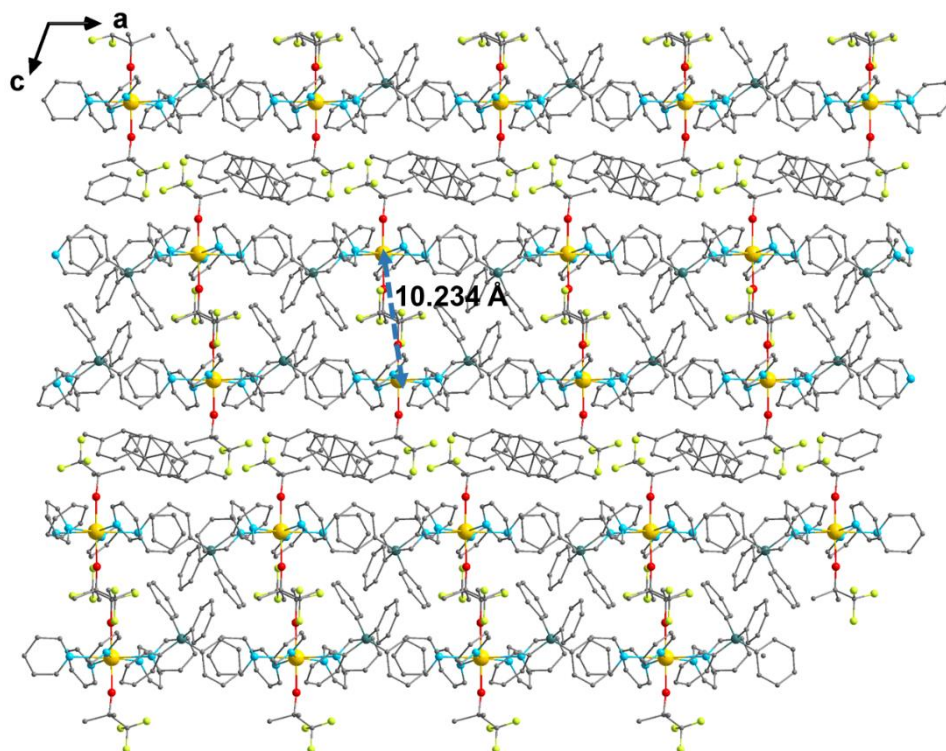
Figure S3. The packing diagram of **3** viewed along the *b* axis. Hydrogen atoms are omitted for clarity.

4. Magnetic Characterization

Magnetic susceptibility measurements were carried out with a Quantum Design MPMS-XL7 SQUID. Freshly prepared crystalline samples were embedded in eicosane to avoid any field-induced crystal reorientation. Diamagnetic corrections have been applied for the eicosane and for the molecule, the latter being calculated from the Pascal constants.
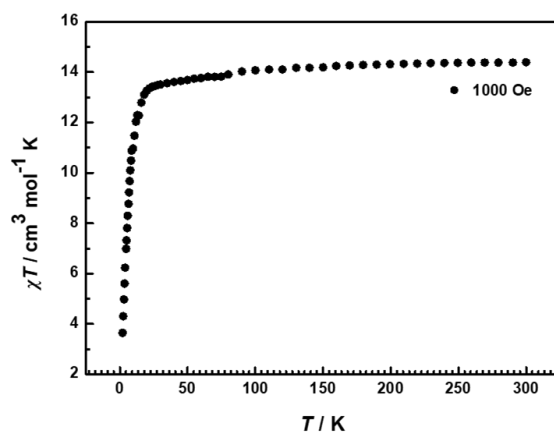
Figure S4. Variable temperature magnetic susceptibility of **1** under a field of 1000 Oe.
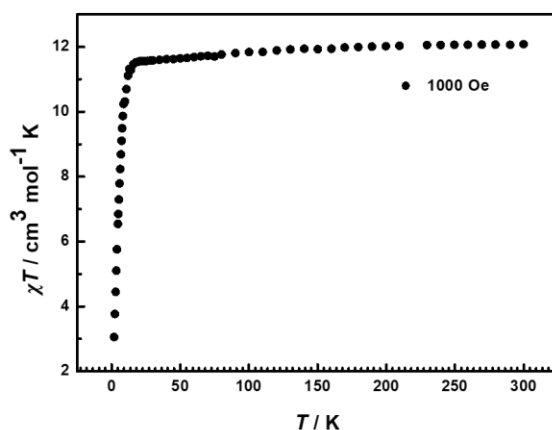
Figure S5. Variable temperature magnetic susceptibility of **2** under a field of 1000 Oe.
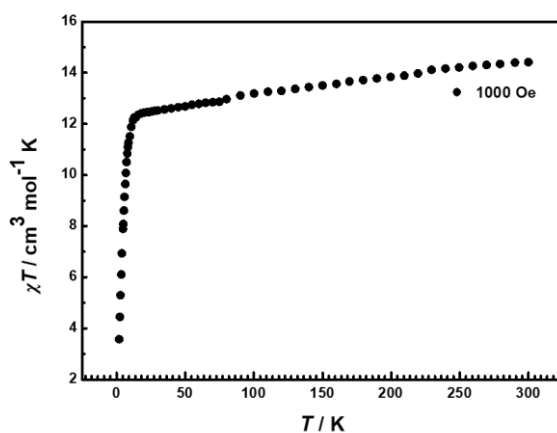
Figure S6. Variable temperature magnetic susceptibility of **3** under a field of 1000 Oe.
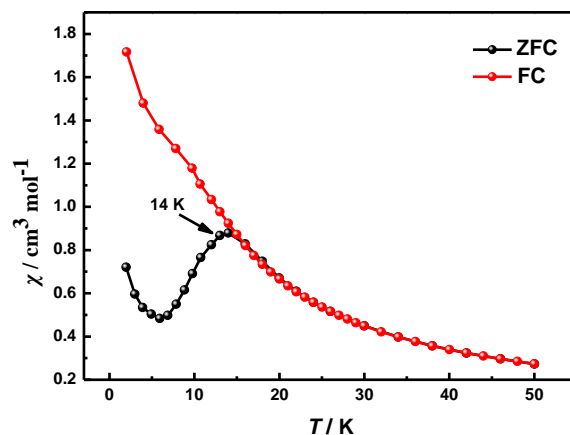
Figure S7. Field-cooled (FC, red line) and zero-field-cooled (ZFC, black line) variable-temperature magnetic susceptibility for **1** under a 2000 Oe DC field in warm mode from 2 to 50 K.
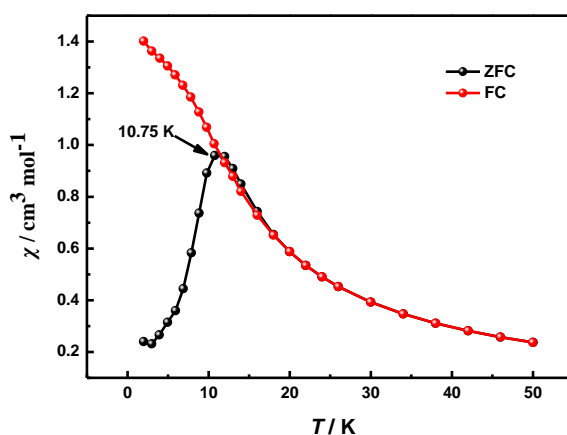
Figure S8. Field-cooled (FC, red line) and zero-field-cooled (ZFC, black line) variable-temperature magnetic susceptibility for **2** under a 2000 Oe DC field in warm mode from 2 to 50 K.
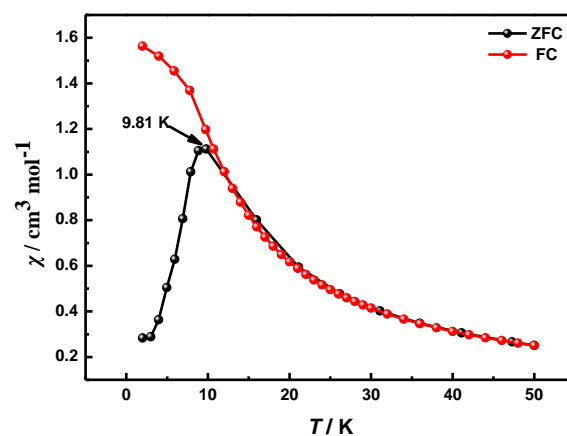
Figure S9. Field-cooled (FC, red line) and zero-field-cooled (ZFC, black line) variable-temperature magnetic susceptibility for **3** under a 2000 Oe DC field in warm mode from 2 to 50 K.
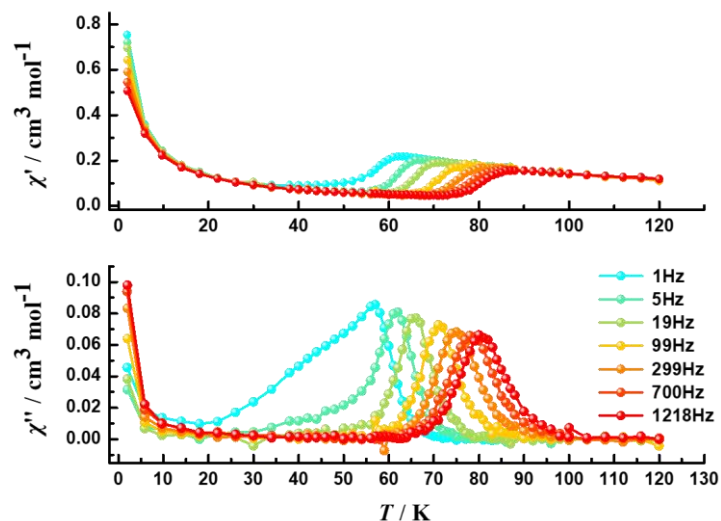
Figure S10. Temperature dependence of the in-phase (top) and out-of-phase (bottom) for **1** in a zero DC field with an AC frequency of 1–1218 Hz.
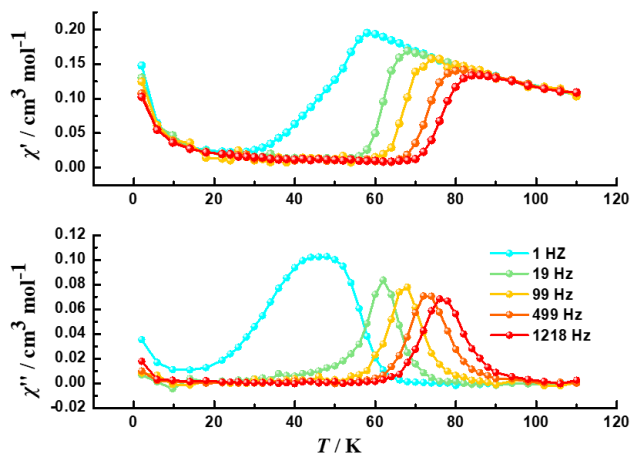
Figure S11. Temperature dependence of the in-phase (top) and out-of-phase (bottom) for **2** in a zero DC field with an AC frequency of 1–1218 Hz.
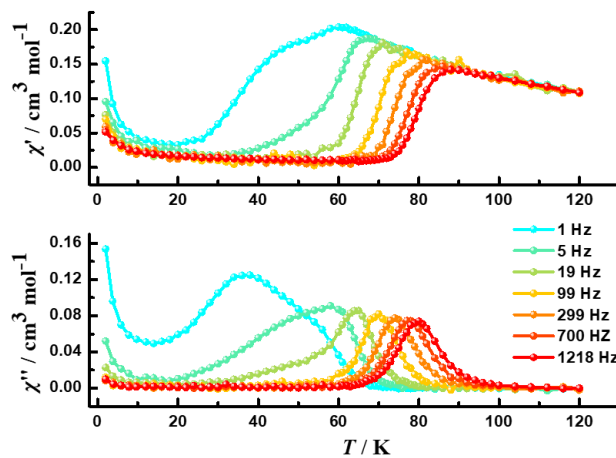
Figure S12. Temperature dependence of the in-phase (top) and out-of-phase (bottom) for **3** in a zero DC field with an AC frequency of 1–1218 Hz.
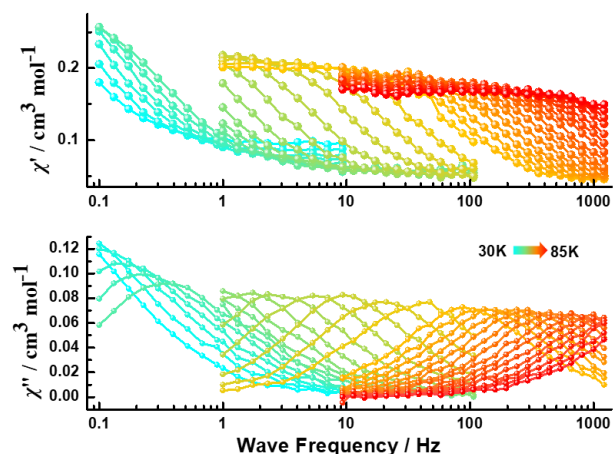
Figure S13. Variable frequency in-phase (top) and out-of-phase (bottom) magnetic susceptibility for **1** under zero applied dc field at frequencies ranging from 9–1217 Hz and temperatures from 30–84 K.
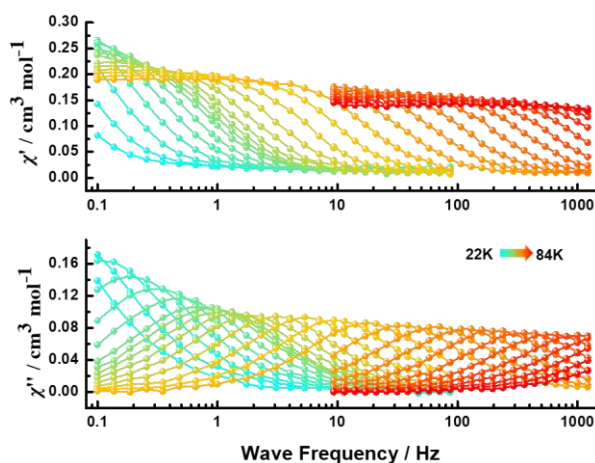
Figure S14. Variable frequency in-phase (top) and out-of-phase (bottom) magnetic susceptibility for **2** under zero applied dc field at frequencies ranging from 9–1217 Hz and temperatures from 22–84 K.
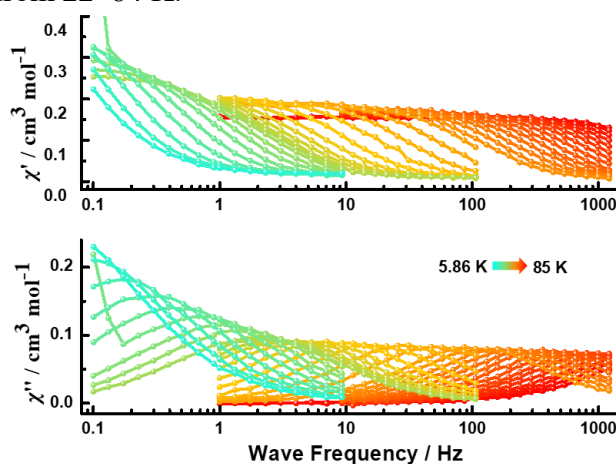
Figure S15. Variable frequency in-phase (top) and out-of-phase (bottom) magnetic susceptibility for **3** under zero applied dc field at frequencies ranging from 9–1217 Hz and temperatures from 5.86–84 K.
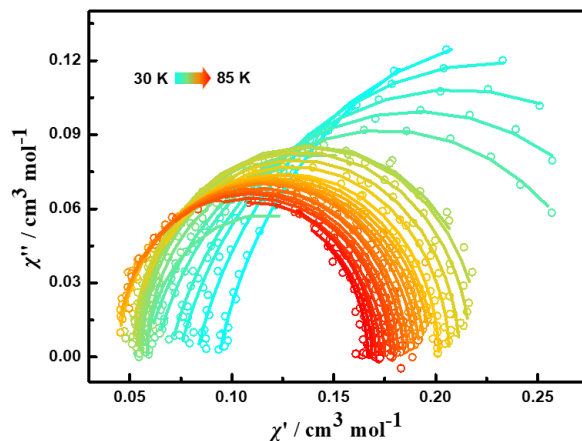
Figure S16. Cole-Cole plot for the AC susceptibilities in a zero DC field for **1** from 30–84 K.
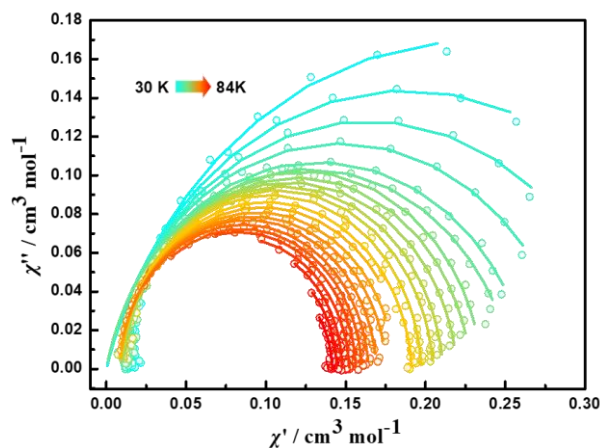
Figure S17. Cole-Cole plot for the AC susceptibilities in a zero DC field for **2** from 30–84 K**.**
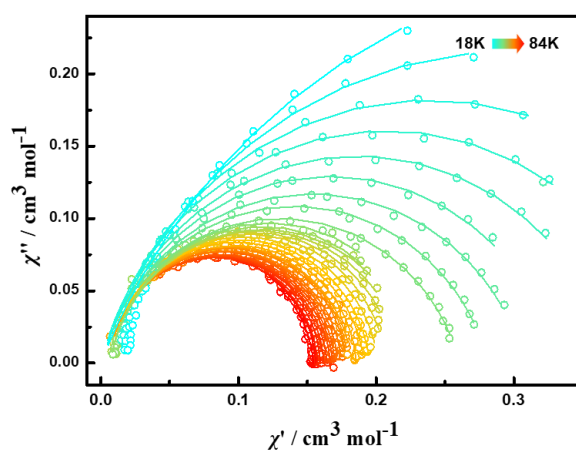
Figure S18. Cole-Cole plot for the AC susceptibilities in a zero DC field for **3** from 18–84 K**.**
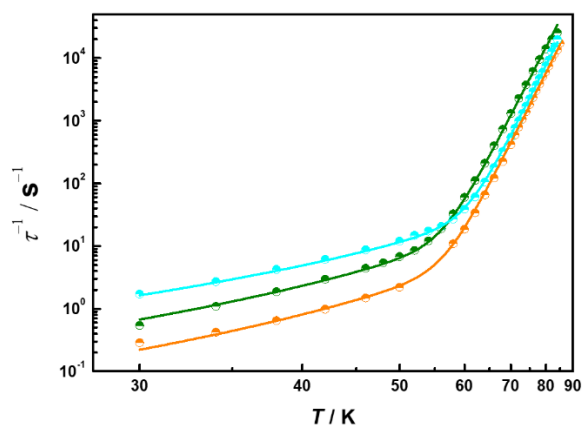
Figure S19. Temperature dependence of the magnetic relaxation rate τ^{-1} in log-log plot. Solid orange, green and sky-blue points are extracted from ac susceptibility data for **1**–**3**, respectively.
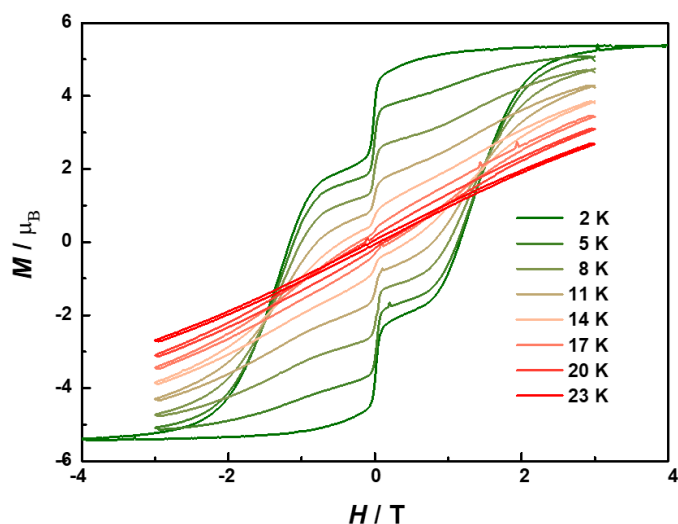
Figure S20. Magnetic hysteresis loops for **1** with an average sweep rate of 100 Oe·s^{-1}.
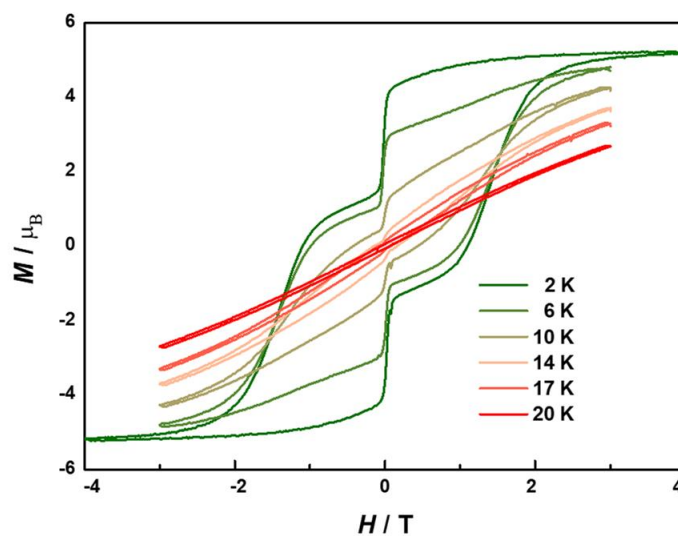
Figure S21. Magnetic hysteresis loops for **2** with an average sweep rate of 100 Oe·s^{-1}.
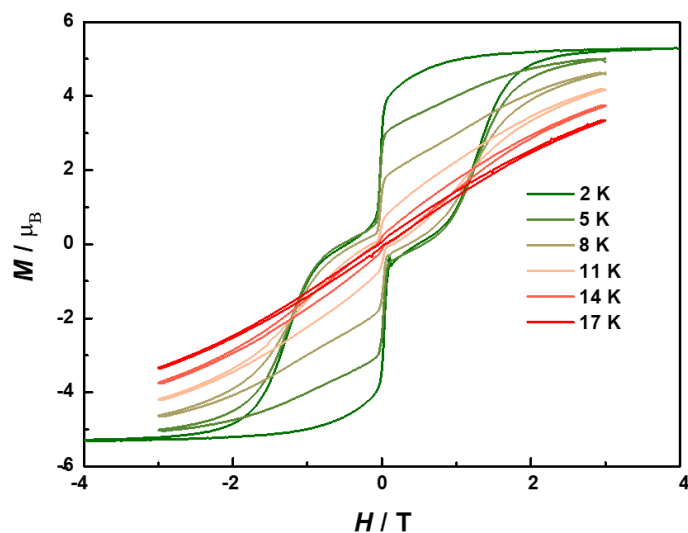
Figure S22. Magnetic hysteresis loops for **3** with an average sweep rate of 100 Oe·s⁻¹.
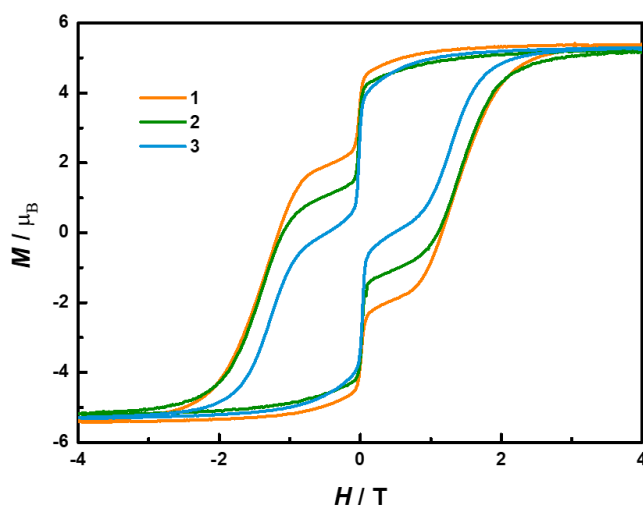
Figure S23. Magnetic hysteresis loops for **1**–**3** with an average sweep rate of 100 Oe·s⁻¹ at 2 K.

Table S7. The magnetic fit parameters for **1**–**4**.

	1	**2**	**3**	**4**
τ_0/s	$3.00(9)\times10^{-12}$	$1.70(6)\times10^{-12}$	$1.88(6)\times10^{-12}$	$1.17(6)\times10^{-12}$
U_{eff}/K	1430(20)	1400(31)	1446(25)	1815(1)
C/s⁻¹·K⁻ⁿ	$5.0(5)\times10^{-8}$	$3.0(4)\times10^{-7}$	$4.0(7)\times10^{-6}$	$1.0(1)\times10^{-6}$
n	4.5(4)	4.3(5)	3.8(2)	3.8(1)
T_B^{ZFC}/K	14.0	10.8	9.8	14.0
T_B^{100s}/K	12.0	8.0	3.0	/
T_B^{hys} (@100 Oe/s)/K	23.0	20.0	17.0	/
τ_{30K}/s	3.48	1.84	0.58	0.44

We extract the magnetic relaxation times from DC magnetisation decay using a stretched exponential $M(t) = M_{eq} + (M_0 - M_{eq})e^{-(t/\tau)^{\alpha}}$.

Table S8. Parameters used to fit dc magnetic relaxation data for **1** and magnetic relaxation times extracted from these fits.

T(K)	$M_0(\mu B)$	$M_{eq}(\mu B)$	α	$\tau(s)$
2	0.97771	0.00212(0.00077)	0.748(0.003)	513(1.9)
4	0.74378	0.00107(0.00061)	0.818(0.004)	316(1.3)
6	0.55248	0.00179(0.01884)	0.865(0.181)	235(38.3)
8	0.40167	0.00038(0.02418)	0.880(0.289)	191(48.1)
10	0.28063	0.00774(0.00759)	0.886(0.070)	154(11.7)
12	0.14896	0.00183(0.00838)	0.923(0.495)	106(44.8)
14	0.06014	0.00191(0.00016)	0.842(0.020)	73(0.9)
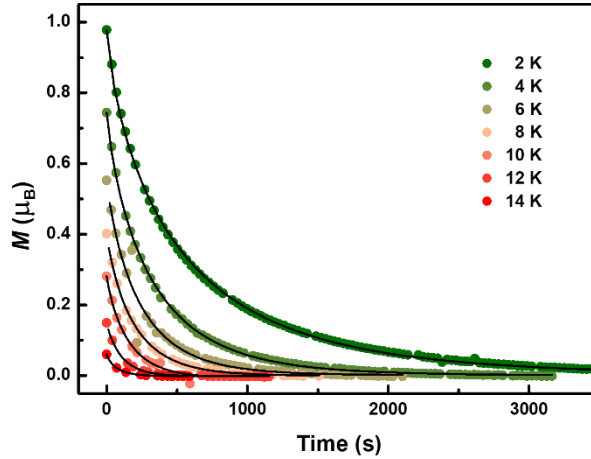
Figure S24. Dc magnetic relaxation data for **1** collected at 2, 4, 6, 8, 10, 12 and 14 K. Black lines represent the fits to the data using stretched exponential functions, which were used to extract τ.

Table S9. Parameters used to fit dc magnetic relaxation data for **2** and magnetic relaxation times extracted from these fits.

T(K)	$M_0(\mu B)$	$M_{eq}(\mu B)$	α	$\tau(s)$
2	1.30906	0.01119(0.00035)	0.880(0.002)	246(0.5)
4	0.82161	0.00165(0.03208)	0.917(0.246)	163(33.7)
6	0.55413	0.00141(0.01907)	0.911(0.284)	136(30.8)
8	0.35534	0.00164(0.01200)	0.913(0.318)	118(31.7)
10	0.21264	0.00147(0.00014)	0.821(0.009)	86(0.7)
12	0.14896	0.00080(0.00523)	0.827(0.690)	69(38.9)
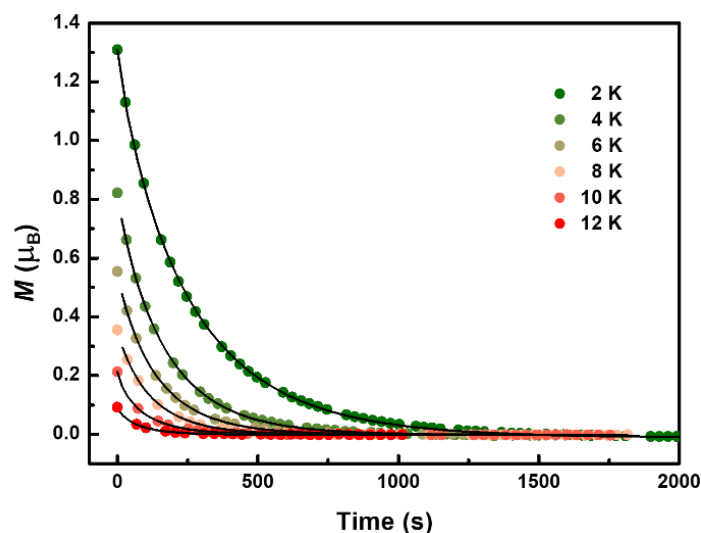
Figure S25. Dc magnetic relaxation data for **2** collected at 2, 4, 6, 8, 10 and 12 K. Black lines represent the fits to the data using stretched exponential functions, which were used to extract τ.

Table S10. Parameters used to fit dc magnetic relaxation data for **3** and magnetic relaxation times extracted from these fits.

$T(K)$	$M_0(\mu B)$	$M_{eq}(\mu B)$	α	$\tau(s)$
2	0.24613	0.00656(0.01191)	0.740(0.168)	219(44.6)
3	0.08125	0.00828(0.00486)	0.870(0.672)	73(39.0)
4	0.01423	0.00640(0.00022)	0.744(0.057)	29(1.2)
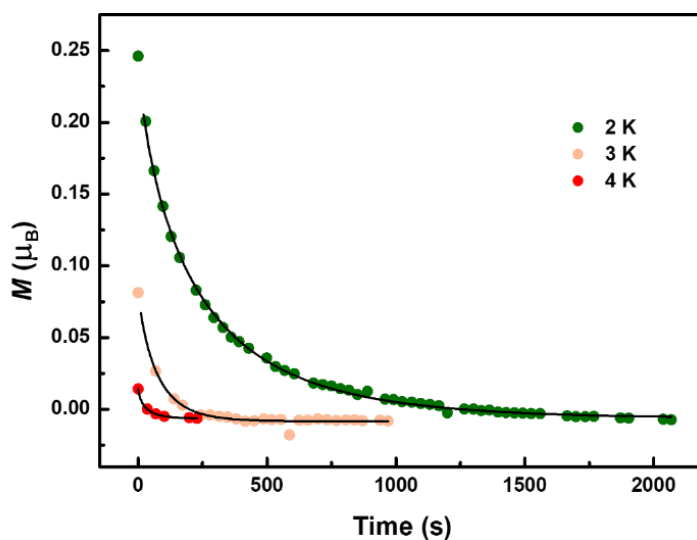
Figure S26. Dc magnetic relaxation data for **3** collected at 2, 3 and 4 K. Black lines represent the fits to the data using stretched exponential functions, which were used to extract τ.
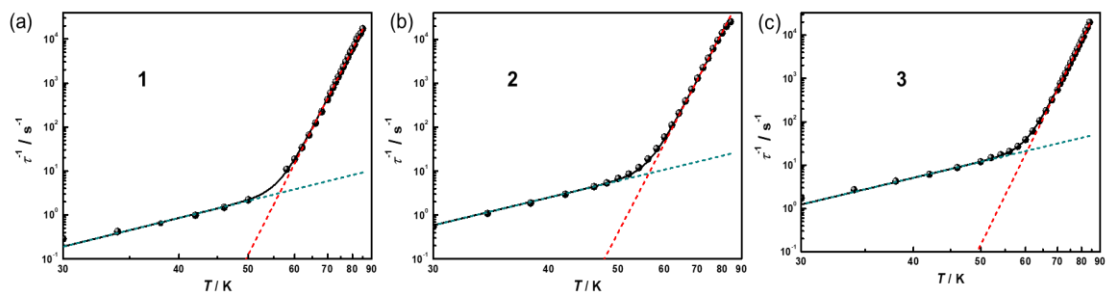
Figure S27. Experimental relaxation rates (black dots) and simulations with Orbach (red dotted line) and Raman (blue dotted line) relaxation processes for **1**–**3**.

5. Ab initio Calculations

Ab initio calculations at the SA-CASSCF/RASSI level were performed using the program OPENMOLCAS software, and the structure was originally taken from the X-ray structure of **1**–**3** without optimization. The basis sets were chosen from the ANO-RCC library[5,] as has been used in many works. The Dy atom was treated with VTZP quality, then the related Cl and O atoms with VDZP quality and others (C and H atoms) with VDZ quality. The state-averaged CASSCF orbitals of the sextets, quartets and doublets were optimized with 21, 224 and 490 states, respectively, with the RASSCF module. Then, 21, 128 and 130 sextets, quartets and doublets were chosen to construct and diagonalize the spin-orbit (SO) coupling Hamiltonian with the RASSI[6] module. These computed SO states were written into the SINGLE_ANISO[7] program to compute the g-tensors, crystal field parameters and magnetic energy levels for the doublets of the ground $J = 15/2$ multiplet of the ^6H term for Dy(III). The two electron integrals were Cholesky decomposed with a threshold of 1×10^{-8} to account for the accuracy[8].
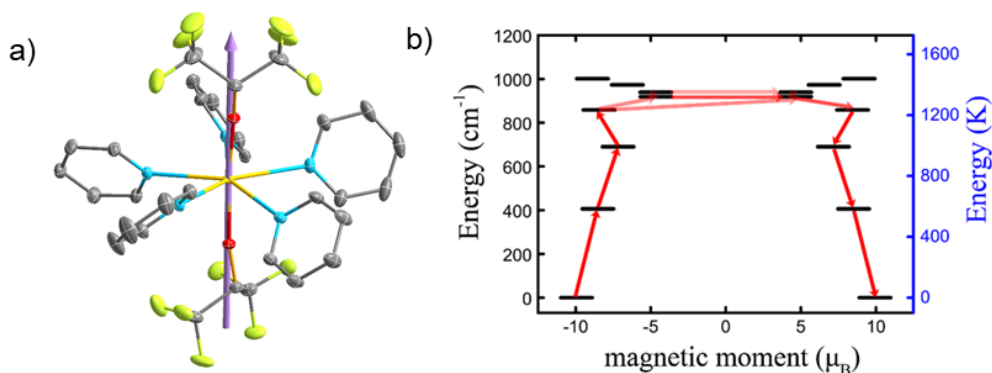
Figure S28. a) The principal magnetic axis of the ground Kramers' doublet of **1**. b) *Ab initio* calculated electronic states of **1** with the probability of transition between different substates. Opacity of the arrows gives the relative transition propensity.
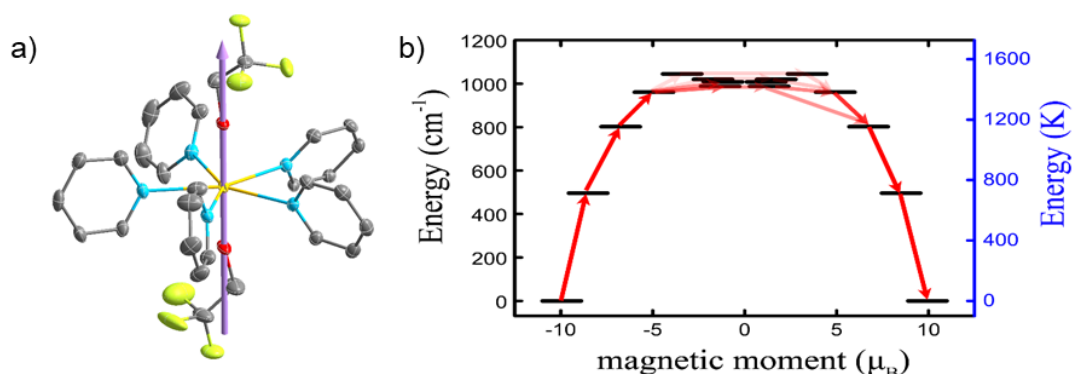
Figure S29. a) The principal magnetic axis of the ground Kramers' doublet of **2**. b) *Ab initio* calculated electronic states of **2** with the probability of transition between different substates. Opacity of the arrows gives the relative transition propensity.
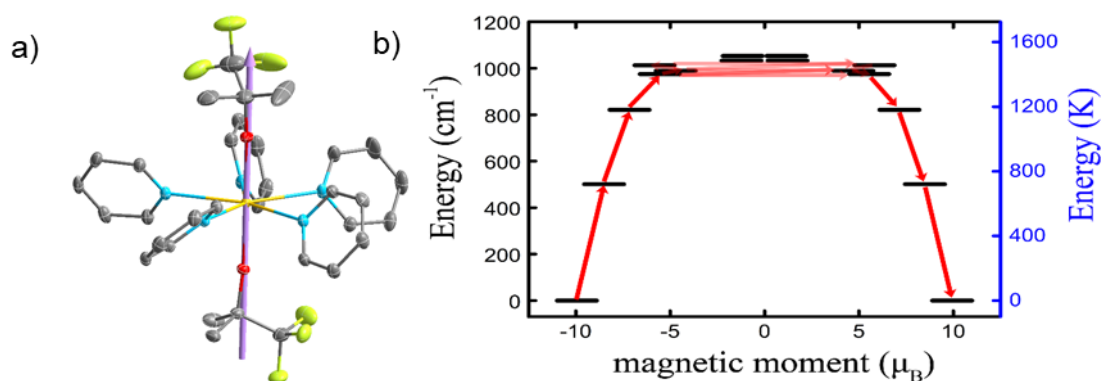
Figure S30. a) The principal magnetic axis of the ground Kramers' doublet of **3**. b) *Ab initio* calculated electronic states of **3** with the probability of transition between different substates. Opacity of the arrows gives the relative transition propensity.

Table S11. SA-CASSCF/RASSI calculated electronic states for **1**.

Energy(cm^{-1})	g_x	g_y	g_z	g_z Angle (°)	Wavefunction [a]
0	0.00	0.00	19.99	--	99.59%$\|\pm15/2\rangle$
406	0.00	0.00	17.33	0.17	99.32%$\|\pm13/2\rangle$
690	0.04	0.04	14.59	0.95	98.54%$\|\pm11/2\rangle$
858	0.31	0.48	11.35	5.21	91.35%$\|\pm9/2\rangle$
919	2.34	3.33	11.95	57.89	23.69%$\|\pm7/2\rangle$ + 19.04%$\|\pm3/2\rangle$ + 33.02%$\|\mp1/2\rangle$ + 10.02%$\|\mp7/2\rangle$
939	2.08	5.03	11.65	84.87	23.52%$\|\pm7/2\rangle$ + 21.84%$\|\pm5/2\rangle$ + 12.43%$\|\pm3/2\rangle$ + 16.30%$\|\pm1/2\rangle$ + 13.38%$\|\mp1/2\rangle$
973	0.24	2.57	14.77	87.96	17.76%$\|\pm7/2\rangle$ + 19.90%$\|\pm5/2\rangle$ + 28.11%$\|\mp3/2\rangle$ + 14.07%$\|\mp5/2\rangle$
1001	0.37	1.77	18.10	89.64	12.90%$\|\pm7/2\rangle$ + 14.93%$\|\pm5/2\rangle$ + 25.11%$\|\pm1/2\rangle$ + 16.77%$\|\mp3/2\rangle$ + 18.46%$\|\mp5/2\rangle$

[a] Only components with > 10% contribution are given, rounded to the nearest percent.

Table S12. SA-CASSCF/RASSI calculated electronic states for **2**.

Energy(cm^{-1})	g_x	g_y	g_z	g_z Angle (°)	Wavefunction [a]
0	0.00	0.00	19.99	--	99.84%$\|\pm15/2>$
496	0.00	0.00	17.32	0.14	99.67%$\|\pm13/2>$
802	0.06	0.06	14.63	1.70	99.36%$\|\pm11/2>$
961	0.10	0.65	11.30	7.30	91.92%$\|\pm9/2>$
988	0.26	2.40	16.70	79.56	67.43%$\|\pm1/2>$ + 15.58%$\|\mp3/2>$
1008	1.89	5.01	10.70	82.91	20.06%$\|\pm5/2>$ + 39.89%$\|\pm3/2>$ + 14.56%$\|\mp1/2>$
1020	2.43	3.75	9.78	87.36	43.43%$\|\pm7/2>$ + 15.19%$\|\pm5/2>$ + 12.58%$\|\mp3/2>$ + 10.65%$\|\mp7/2>$
1045	0.33	1.79	16.95	70.59	31.71%$\|\pm7/2>$ + 49.06%$\|\pm5/2>$ + 10.81%$\|\pm3/2>$

[a] Only components with > 10% contribution are given, rounded to the nearest percent.

Table S13. SA-CASSCF/RASSI calculated electronic states for **3**.

Energy(cm^{-1})	g_x	g_y	g_z	g_z Angle (°)	Wavefunction [a]
0	0.00	0.00	19.89	--	99.85%$\|\pm15/2>$
501	0.00	0.00	17.00	0.86	99.77%$\|\pm13/2>$
821	0.12	0.13	14.30	4.30	99.29%$\|\pm11/2>$
975	1.11	4.43	11.09	56.11	36.32%$\|\pm9/2>$ + 35.5%$\|\pm1/2>$ + 20.44%$\|\mp1/2>$
989	0.52	4.27	9.41	69.58	50.51%$\|\pm9/2>$ + 12.5%$\|\pm1/2>$ + 10.00%$\|\mp1/2>$ + 15.75%$\|\mp3/2>$
1013	1.59	3.28	11.66	87.05	20.24%$\|\pm3/2>$ + 10.33%$\|\pm1/2>$ + 39.44%$\|\mp3/2>$
1033	8.24	5.44	2.43	14.12	48.68%$\|\pm5/2>$ + 28.56%$\|\mp7/2>$
1053	10.78	8.25	2.32	35.07	29.55%$\|\pm5/2>$ + 59.08%$\|\mp7/2>$

[a] Only components with > 10% contribution are given, rounded to the nearest percent.

Table S14. *Ab initio* calculated crystal field parameters for **1**.

Crystal Field Parameter	Value/cm^{-1}
B_2^{-2}	0.19036090008539E-01
B_2^{-1}	-0.64326178133895E-02
B_2^0	-0.54984968157226E+01
B_2^1	-0.53748352187433E-01
B_2^2	0.53696019841536E+00
B_4^{-4}	0.20135067031742E-02
B_4^{-3}	0.41638265408368E-01
B_4^{-2}	-0.17844040925424E-02
B_4^{-1}	-0.75947884258835E-02
B_4^0	-0.95355199319257E-02
B_4^1	-0.18348923514741E-02
B_4^2	-0.10614740418241E-02
B_4^3	-0.14353430859682E-02
B_4^4	0.21288638438911E-03
B_6^{-6}	0.53142546771471E-04
B_6^{-5}	-0.88856600814674E-05
B_6^{-4}	0.13810544902778E-04
B_6^{-3}	0.21879769838885E-04
B_6^{-2}	-0.29275202003422E-04
B_6^{-1}	-0.20439183210056E-04
B_6^0	0.13776902733203E-04
B_6^1	-0.89685619080196E-04
B_6^2	-0.47978359471852E-05
B_6^3	-0.21314327004720E-04
B_6^4	0.64705177050995E-05
B_6^5	0.16347797808480E-03
B_6^6	0.38361329472417E-04

Table S15. *Ab initio* calculated crystal field parameters for **2**.

Crystal Field Parameter	Value/cm^{-1}
B_2^{-2}	0.31492286767030E-01
B_2^{-1}	-0.21792276850590E-02
B_2^0	-0.55961133235008E+01
B_2^1	-0.10279451066309E-01
B_2^2	0.16152339710067E+00
B_4^{-4}	0.17462963193797E-02
B_4^{-3}	-0.17612107994597E-01
B_4^{-2}	-0.42389095623109E-03
B_4^{-1}	-0.18991855676960E-02
B_4^0	-0.12630408365727E-01
B_4^1	0.73752382774966E-02
B_4^2	-0.11032284808258E-02
B_4^3	-0.38195016101834E-02
B_4^4	-0.34140735603897E-03
B_6^{-6}	0.42339808848895E-04
B_6^{-5}	-0.48419079641848E-04
B_6^{-4}	0.19369551913468E-04
B_6^{-3}	-0.13247791065504E-03
B_6^{-2}	-0.23220995464180E-04
B_6^{-1}	-0.42261910975963E-04
B_6^0	0.61038974308974E-05
B_6^1	-0.82355493572610E-05
B_6^2	0.15732758123830E-04
B_6^3	-0.11044437632652E-04
B_6^4	0.74505420390760E-06
B_6^5	-0.26003509916628E-03
B_6^6	0.13065462406920E-04

Table S16. *Ab initio* calculated crystal field parameters for **3**.

Crystal Field Parameter	Value/cm^{-1}
B_2^{-2}	0.24068282706477E-01
B_2^{-1}	0.44885915171866E-01
B_2^0	-0.55860307900551E+01
B_2^1	-0.51263451362109E-01
B_2^2	0.24835614920004E+00
B_4^{-4}	0.29113293252248E-02
B_4^{-3}	-0.74530826240698E-02
B_4^{-2}	-0.15216769225217E-03
B_4^{-1}	0.59405400719026E-02
B_4^0	-0.13507376911849E-01
B_4^1	-0.23080196784108E-02
B_4^2	-0.13100065155309E-02
B_4^3	-0.30906530519354E-02
B_4^4	-0.37446649344675E-02
B_6^{-6}	0.55906858269436E-04
B_6^{-5}	-0.80371704100472E-04
B_6^{-4}	0.26368723865022E-04
B_6^{-3}	-0.47029241575159E-04
B_6^{-2}	0.65950770324006E-07
B_6^{-1}	0.31441854402680E-04
B_6^0	0.10684117949958E-04
B_6^1	-0.21626688879242E-04
B_6^2	-0.13769967928503E-05
B_6^3	-0.19767572938235E-04
B_6^4	-0.30799832134555E-04
B_6^5	-0.19527503406363E-03
B_6^6	-0.42332112717751E-04

Table S17. Average transition magnetic moment elements between the states of **1**, given in μ_B^2. *

	$|+\frac{15}{2}\rangle$	$|-\frac{15}{2}\rangle$	$|+\frac{13}{2}\rangle$	$|-\frac{13}{2}\rangle$	$|+\frac{11}{2}\rangle$	$|-\frac{11}{2}\rangle$	$|+\frac{9}{2}\rangle$	$|-\frac{9}{2}\rangle$	$|+a\rangle$	$|-a\rangle$	$|+b\rangle$	$|-b\rangle$	$|+c\rangle$	$|-c\rangle$	$|+d\rangle$	$|-d\rangle$
$|+\frac{15}{2}\rangle$	--	--	4.8E-09	4.4E+00	2.9E-02	5.2E-07	1.9E-06	3.5E-03	2.5E-04	1.9E-04	1.3E-04	1.0E-04	2.8E-04	1.4E-04	1.5E-04	1.5E-04
$|-\frac{15}{2}\rangle$	--	--	4.4E+00	4.8E-09	5.2E-07	2.9E-02	3.5E-03	1.9E-06	1.9E-04	2.5E-04	1.0E-04	1.3E-04	1.4E-04	2.8E-04	1.5E-04	1.5E-04
$|+\frac{13}{2}\rangle$	4.8E-09	4.4E+00	--	3.5E-07	1.6E-04	8.3E+00	3.5E-02	8.1E-05	7.2E-03	6.7E-03	2.5E-03	4.3E-03	3.4E-03	6.5E-03	2.6E-03	2.7E-03
$|-\frac{13}{2}\rangle$	4.4E+00	4.8E-09	3.5E-07	--	8.3E+00	1.6E-04	8.1E-05	3.5E-02	6.7E-03	7.2E-03	4.3E-03	2.5E-03	6.5E-03	3.4E-03	2.7E-03	2.6E-03
$|+\frac{11}{2}\rangle$	2.9E-02	5.2E-07	1.6E-04	8.3E+00	--	1.5E-03	3.2E-03	1.1E+01	3.8E-02	8.1E-02	7.8E-02	5.0E-02	4.4E-02	1.2E-01	1.3E-02	5.5E-02
$|-\frac{11}{2}\rangle$	5.2E-07	2.9E-02	8.3E+00	1.6E-04	1.5E-03	--	1.1E+01	3.2E-03	8.1E-02	3.8E-02	5.0E-02	7.8E-02	1.2E-01	4.4E-02	5.5E-02	1.3E-02
$|+\frac{9}{2}\rangle$	1.9E-06	3.5E-03	3.5E-02	8.1E-05	3.2E-03	1.1E+01	--	4.0E-02	5.4E+00	3.5E+00	1.1E+00	3.2E+00	5.2E-01	1.2E+00	1.5E-01	5.4E-01
$|-\frac{9}{2}\rangle$	3.5E-03	1.9E-06	8.1E-05	3.5E-02	1.1E+01	3.2E-03	4.0E-02	--	3.5E+00	5.4E+00	3.2E+00	1.1E+00	1.2E+00	5.2E-01	5.4E-01	1.5E-01
$|+a\rangle$	2.5E-04	1.9E-04	7.2E-03	6.7E-03	3.8E-02	8.1E-02	5.4E+00	3.5E+00	--	1.3E+01	2.9E+00	8.7E+00	2.4E+00	6.3E-01	4.1E-01	4.4E-01
$|-a\rangle$	1.9E-04	2.5E-04	6.7E-03	7.2E-03	8.1E-02	3.8E-02	3.5E+00	5.4E+00	1.3E+01	--	8.7E+00	2.9E+00	6.3E-01	2.4E+00	4.4E-01	4.1E-01
$|+b\rangle$	1.3E-04	1.0E-04	2.5E-03	4.3E-03	7.8E-02	5.0E-02	1.1E+00	3.2E+00	2.9E+00	8.7E+00	--	2.9E+00	4.1E+00	2.6E+00	4.4E-01	7.2E-01
$|-b\rangle$	1.0E-04	1.3E-04	4.3E-03	2.5E-03	5.0E-02	7.8E-02	3.2E+00	1.1E+00	8.7E+00	2.9E+00	2.9E+00	--	2.6E+00	4.1E+00	7.2E-01	4.4E-01
$|+c\rangle$	2.8E-04	1.4E-04	3.4E-03	6.5E-03	4.4E-02	1.2E-01	5.2E-01	1.2E+00	2.4E+00	6.3E-01	4.1E+00	2.6E+00	--	1.8E+01	5.8E+00	1.7E+00
$|-c\rangle$	1.4E-04	2.8E-04	6.5E-03	3.4E-03	1.2E-01	4.4E-02	1.2E+00	5.2E-01	6.3E-01	2.4E+00	2.6E+00	4.1E+00	1.8E+01	--	1.7E+00	5.8E+00
$|+d\rangle$	1.5E-04	1.5E-04	2.6E-03	2.7E-03	1.3E-02	5.5E-02	1.5E-01	5.4E-01	4.1E-01	4.4E-01	4.4E-01	7.2E-01	5.8E+00	1.7E+00	--	2.6E+01
$|-d\rangle$	1.5E-04	1.5E-04	2.7E-03	2.6E-03	5.5E-02	1.3E-02	5.4E-01	1.5E-01	4.4E-01	4.1E-01	7.2E-01	4.4E-01	1.7E+00	5.8E+00	2.6E+01	--

* The states $|\pm a\rangle$ to $|\pm d\rangle$ represent the fifth to eighth KDs with highly mixed wavefunctions.

Table S18. Average transition magnetic moment elements between the states of **2**, given in μ_B^2. *

	$\|+\frac{15}{2}>$	$\|-\frac{15}{2}>$	$\|+\frac{13}{2}>$	$\|-\frac{13}{2}>$	$\|+\frac{11}{2}>$	$\|-\frac{11}{2}>$	$\|+\frac{9}{2}>$	$\|-\frac{9}{2}>$	$\|+a>$	$\|-a>$	$\|+b>$	$\|-b>$	$\|+c>$	$\|-c>$	$\|+d>$	$\|-d>$
$\|+\frac{15}{2}>$	--	1.1E-10	4.4E+00	1.1E-07	8.3E-03	3.3E-07	1.2E-06	2.0E-03	9.2E-05	1.7E-05	4.5E-05	1.2E-04	6.3E-05	2.7E-04	4.5E-04	7.3E-06
$\|-\frac{15}{2}>$	1.1E-10	--	1.1E-07	4.4E+00	3.3E-07	8.3E-03	2.0E-03	1.2E-06	1.7E-05	9.2E-05	1.2E-04	4.5E-05	2.7E-04	6.3E-05	7.3E-06	4.5E-04
$\|+\frac{13}{2}>$	4.4E+00	1.1E-07	--	2.4E-06	8.3E+00	3.4E-04	4.9E-04	2.2E-02	9.4E-04	3.1E-03	2.4E-03	2.6E-03	7.0E-04	1.7E-03	7.2E-03	2.3E-05
$\|-\frac{13}{2}>$	1.1E-07	4.4E+00	2.4E-06	--	3.4E-04	8.3E+00	2.2E-02	4.9E-04	3.1E-03	9.4E-04	2.6E-03	2.4E-03	1.7E-03	7.0E-04	2.3E-05	7.2E-03
$\|+\frac{11}{2}>$	8.3E-03	3.3E-07	8.3E+00	3.4E-04	--	3.3E-03	6.5E-03	1.1E+01	2.9E-01	2.8E-02	2.4E-02	6.7E-02	2.0E-02	1.1E-01	8.8E-02	2.6E-03
$\|-\frac{11}{2}>$	3.3E-07	8.3E-03	3.4E-04	8.3E+00	3.3E-03	--	1.1E+01	6.5E-03	2.8E-02	2.9E-01	6.7E-02	2.4E-02	1.1E-01	2.0E-02	2.6E-03	8.8E-02
$\|+\frac{9}{2}>$	1.2E-06	2.0E-03	4.9E-04	2.2E-02	6.5E-03	1.1E+01	--	5.4E-02	1.2E+00	7.2E-01	4.4E-01	4.0E+00	5.7E+00	1.3E+00	1.1E-01	2.6E+00
$\|-\frac{9}{2}>$	2.0E-03	1.2E-06	2.2E-02	4.9E-04	1.1E+01	6.5E-03	5.4E-02	--	7.2E-01	1.2E+00	4.0E+00	4.4E-01	1.3E+00	5.7E+00	2.6E+00	1.1E-01
$\|+a>$	9.2E-05	1.7E-05	9.4E-04	3.1E-03	2.9E-01	2.8E-02	1.2E+00	7.2E-01	--	2.3E+01	4.9E+00	2.0E+00	1.3E+00	3.0E+00	4.8E-01	1.5E-01
$\|-a>$	1.7E-05	9.2E-05	3.1E-03	9.4E-04	2.8E-02	2.9E-01	7.2E-01	1.2E+00	2.3E+01	--	2.0E+00	4.9E+00	3.0E+00	1.3E+00	1.5E-01	4.8E-01
$\|+b>$	4.5E-05	1.2E-04	2.4E-03	2.6E-03	2.4E-02	6.7E-02	4.4E-01	4.0E+00	4.9E+00	2.0E+00	--	8.8E+00	6.2E+00	4.3E+00	1.4E+00	2.5E+00
$\|-b>$	1.2E-04	4.5E-05	2.6E-03	2.4E-03	6.7E-02	2.4E-02	4.0E+00	4.4E-01	2.0E+00	4.9E+00	8.8E+00	--	4.3E+00	6.2E+00	2.5E+00	1.4E+00
$\|+c>$	6.3E-05	2.7E-04	7.0E-04	1.7E-03	2.0E-02	1.1E-01	5.7E+00	1.3E+00	1.3E+00	3.0E+00	6.2E+00	4.3E+00	--	4.8E+00	1.6E+00	4.6E+00
$\|-c>$	2.7E-04	6.3E-05	1.7E-03	7.0E-04	1.1E-01	2.0E-02	1.3E+00	5.7E+00	3.0E+00	1.3E+00	4.3E+00	6.2E+00	4.8E+00	--	4.6E+00	1.6E+00
$\|+d>$	4.5E-04	7.3E-06	7.2E-03	2.3E-05	8.8E-02	2.6E-03	1.1E-01	2.6E+00	4.8E-01	1.5E-01	1.4E+00	2.5E+00	1.6E+00	4.6E+00	--	9.6E-01
$\|-d>$	7.3E-06	4.5E-04	2.3E-05	7.2E-03	2.6E-03	8.8E-02	2.6E+00	1.1E-01	1.5E-01	4.8E-01	2.5E+00	1.4E+00	4.6E+00	1.6E+00	9.6E-01	--

* The states $|\pm a>$ to $|\pm d>$ represent the fifth to eighth KDs with highly mixed wavefunctions.

Table S19. Average transition magnetic moment elements between the states of **3**, given in μ_B^2. *

	$\lvert+\tfrac{15}{2}\rangle$	$\lvert-\tfrac{15}{2}\rangle$	$\lvert+\tfrac{13}{2}\rangle$	$\lvert-\tfrac{13}{2}\rangle$	$\lvert+\tfrac{11}{2}\rangle$	$\lvert-\tfrac{11}{2}\rangle$	$\lvert+a\rangle$	$\lvert-a\rangle$	$\lvert+b\rangle$	$\lvert-b\rangle$	$\lvert+c\rangle$	$\lvert-c\rangle$	$\lvert+d\rangle$	$\lvert-d\rangle$	$\lvert+e\rangle$	$\lvert-e\rangle$
$\lvert+\tfrac{15}{2}\rangle$	--	2.5E-10	4.4E+00	1.1E-07	6.0E-06	6.0E-03	3.7E-05	3.3E-04	4.3E-05	4.7E-04	1.6E-04	6.2E-05	3.2E-04	2.6E-04	1.1E-04	4.2E-04
$\lvert-\tfrac{15}{2}\rangle$	2.5E-10	--	1.1E-07	4.4E+00	6.0E-03	6.0E-06	3.3E-04	3.7E-05	4.7E-04	4.3E-05	6.2E-05	1.6E-04	2.6E-04	3.2E-04	4.2E-04	1.1E-04
$\lvert+\tfrac{13}{2}\rangle$	4.4E+00	1.1E-07	--	3.1E-06	5.9E-03	8.3E+00	3.7E-03	7.8E-03	1.1E-03	6.4E-03	7.4E-03	3.6E-03	2.5E-03	3.7E-03	1.7E-03	4.1E-03
$\lvert-\tfrac{13}{2}\rangle$	1.1E-07	4.4E+00	3.1E-06	--	8.3E+00	5.9E-03	7.8E-03	3.7E-03	6.4E-03	1.1E-03	3.6E-03	7.4E-03	3.7E-03	2.5E-03	4.1E-03	1.7E-03
$\lvert+\tfrac{11}{2}\rangle$	6.0E-06	6.0E-03	5.9E-03	8.3E+00	--	5.2E-02	5.0E+00	3.9E-02	5.5E+00	1.1E-01	2.8E-01	3.5E-01	6.2E-02	2.2E-01	3.7E-02	2.2E-02
$\lvert-\tfrac{11}{2}\rangle$	6.0E-03	6.0E-06	8.3E+00	5.9E-03	5.2E-02	--	3.9E-02	5.0E+00	1.1E-01	5.5E+00	3.5E-01	2.8E-01	2.2E-01	6.2E-02	2.2E-02	3.7E-02
$\lvert+a\rangle$	3.7E-05	3.3E-04	3.7E-03	7.8E-03	5.0E+00	3.9E-02	--	4.7E+00	6.3E+00	3.1E+00	5.3E+00	3.1E+00	1.7E-01	6.7E-01	1.9E+00	1.5E-01
$\lvert-a\rangle$	3.3E-04	3.7E-05	7.8E-03	3.7E-03	3.9E-02	5.0E+00	4.7E+00	--	3.1E+00	6.3E+00	3.1E+00	5.3E+00	6.7E-01	1.7E-01	1.5E-01	1.9E+00
$\lvert+b\rangle$	4.3E-05	4.7E-04	1.1E-03	6.4E-03	5.5E+00	1.1E-01	6.3E+00	3.1E+00	--	1.9E+00	1.5E+00	1.2E+00	2.9E-01	8.4E+00	1.8E+00	5.5E-01
$\lvert-b\rangle$	4.7E-04	4.3E-05	6.4E-03	1.1E-03	1.1E-01	5.5E+00	3.1E+00	6.3E+00	1.9E+00	--	1.2E+00	1.5E+00	8.4E+00	2.9E-01	5.5E-01	1.8E+00
$\lvert+c\rangle$	1.6E-04	6.2E-05	7.4E-03	3.6E-03	2.8E-01	3.5E-01	5.3E+00	3.1E+00	1.5E+00	1.2E+00	--	1.2E+01	3.5E+00	4.4E+00	3.5E+00	2.8E+00
$\lvert-c\rangle$	6.2E-05	1.6E-04	3.6E-03	7.4E-03	3.5E-01	2.8E-01	3.1E+00	5.3E+00	1.2E+00	1.5E+00	1.2E+01	--	4.4E+00	3.5E+00	2.8E+00	3.5E+00
$\lvert+d\rangle$	3.2E-04	2.6E-04	2.5E-03	3.7E-03	6.2E-02	2.2E-01	1.7E-01	6.7E-01	2.9E-01	8.4E+00	3.5E+00	4.4E+00	--	7.3E+00	1.5E+00	9.3E+00
$\lvert-d\rangle$	2.6E-04	3.2E-04	3.7E-03	2.5E-03	2.2E-01	6.2E-02	6.7E-01	1.7E-01	8.4E+00	2.9E-01	4.4E+00	3.5E+00	7.3E+00	--	9.3E+00	1.5E+00
$\lvert+e\rangle$	1.1E-04	4.2E-04	1.7E-03	4.1E-03	3.7E-02	2.2E-02	1.9E+00	1.5E-01	1.8E+00	5.5E-01	3.5E+00	2.8E+00	1.5E+00	9.3E+00	--	1.4E+01
$\lvert-e\rangle$	4.2E-04	1.1E-04	4.1E-03	1.7E-03	2.2E-02	3.7E-02	1.5E-01	1.9E+00	5.5E-01	1.8E+00	2.8E+00	3.5E+00	9.3E+00	1.5E+00	1.4E+01	--

* The states $\lvert\pm a\rangle$ to $\lvert\pm e\rangle$ represent the fourth to eighth KDs with highly mixed wavefunctions.

6. DFT Calculations

The molecular vibration modes were calculated using DFT methods based on Gaussian 09D software.[9] The Dy(III) ion was substituted by the Y(III) ion to avoid a convergence problem, while the atomic mass of Y(III) was set to be the same as Dy(III) (162.5). The geometries were taken from the X-ray single crystal structures of **1**–**3**. The methods we used were PBE density functional plus Grimme's D3 dispersion correction.[10] We chose the cc-pVDZ basis set for carbon, hydrogen, oxygen, nitrogen and boron atoms,[11] while for yttrium, the Stuttgart RSC 1997 effective core potential (ECP) was employed, [12] as such was commonly used in computing vibrations for Dy(III) ion-based complexes.

Table S20 Coordination geometry of the cation for complex **1**.

Atom	x(Å)	y(Å)	z(Å)
Dy	0.000014	-0.000044	-0.090840
O	-2.114270	-0.238600	-0.232630
O	2.114280	0.238530	-0.232750
N	-0.340650	1.418900	1.974340
N	0.340930	-1.418560	1.974570
N	0.096950	-2.440580	-0.836300
N	-0.097230	2.440250	-0.836990
N	0.000079	-0.000494	-2.636220
H	1.990700	-0.880440	-5.247420
C	1.103440	-0.487930	-4.732450
C	-0.000051	-0.001330	-5.447840
C	1.061760	-0.470320	-3.333430
C	-1.103480	0.485710	-4.732630
H	-0.000103	-0.001660	-6.547180
H	1.902400	-0.848980	-2.733490
C	-1.061660	0.468920	-3.333610
H	-1.990780	0.877910	-5.247760
F	3.694020	-1.731160	-1.455140
H	-1.902250	0.847940	-2.733810
H	3.690560	0.848960	-1.460240
C	4.183400	-0.950950	-0.438710
F	-3.693830	1.730680	-1.456030
F	-3.387310	-2.605850	0.448350
F	-3.891590	-0.996570	1.850700
C	-3.450140	-0.410020	-0.454670
F	3.891540	0.997960	1.850030
F	3.387000	2.606400	0.446830
F	3.963110	-1.637210	0.719780

C	3.450100	0.410080	-0.454980
C	-1.466140	1.270430	2.713810
C	0.605560	2.279640	2.419790
C	1.466570	-1.270070	2.713820
C	-0.605310	-2.279090	2.420380
C	-0.905830	-2.936190	-1.598930
C	1.101220	-3.281190	-0.491920
C	0.905260	2.935680	-1.600110
C	-1.101420	3.280910	-0.492510
F	5.359950	1.654330	0.356160
F	5.515260	-0.845230	-0.615560
H	-1.899700	2.855660	0.130560
C	-4.183200	0.951150	-0.439090
H	-3.690760	-0.849410	-1.459670
H	-1.704510	-2.225220	-1.851330
H	-1.503360	-2.380080	1.794960
C	-4.050090	-1.411230	0.559850
H	-2.213530	0.570630	2.315070
C	4.049950	1.411940	0.558950
H	1.503490	2.380600	1.794200
H	1.899730	-2.855800	0.130750
C	-1.685310	1.966660	3.907740
C	0.468390	3.009500	3.605730
H	2.213970	-0.570440	2.314800
C	1.685850	-1.966060	3.907860
C	-0.468030	-3.008720	3.606450
C	-0.946380	-4.262280	-2.041080
C	1.143690	-4.620930	-0.893970
H	1.703890	2.224680	-1.852600
C	0.945590	4.261640	-2.042670
C	-1.144090	4.620530	-0.894930
F	-3.962640	1.638030	0.718980
F	-5.515100	0.845550	-0.615700
F	-5.360130	-1.653570	0.357230
H	-2.619640	1.812340	4.464040
C	-0.699470	2.852130	4.365710
H	1.269680	3.691160	3.921250
H	2.620290	-1.811730	4.463970
C	0.699990	-2.851320	4.366190
H	-1.269330	-3.690220	3.922260
H	-1.789680	-4.609660	-2.652970
C	0.100250	-5.123930	-1.683060
H	1.986700	-5.254700	-0.587660

C	-0.100950	5.123350	-1.684530
H	1.788660	4.608880	-2.654960
H	-1.987030	5.254350	-0.588520
H	-0.839560	3.412940	5.300820
H	0.840180	-3.411940	5.301400
H	0.101210	-6.172530	-2.013110
H	-0.102070	6.171850	-2.014890

Table S21. Coordination geometry of the cation for complex **2**.

Atom	x(Å)	y(Å)	z(Å)
Dy	12.71109	-11.7673	5.6264
O	12.97016	-11.589	7.66747
O	12.11483	-12.0658	3.67377
N	12.8569	-14.236	5.91296
N	15.03669	-12.4039	4.96972
N	14.10589	-9.71824	5.30577
N	11.1423	-9.83667	5.7221
N	10.43134	-12.6299	6.21516
F	15.75802	-11.0153	8.46538
F	15.14189	-13.219	8.48072
C	13.36477	-11.5291	9.02525
F	13.92903	-10.8879	1.67006
F	12.13783	-9.60187	2.28356
C	11.81541	-12.0903	2.29057
C	12.24191	-15.067	4.97263
C	13.39294	-14.8674	7.04044
C	16.00018	-12.9251	5.84258
C	15.43186	-12.2378	3.63607
C	15.05037	-9.38128	6.2838
C	14.03084	-8.86749	4.19558
C	10.64927	-9.42287	6.96253
C	10.60545	-9.1993	4.59841
C	9.43489	-12.8398	5.25898
C	10.07996	-12.9239	7.53473
H	13.27704	-10.5013	9.47554
C	14.93376	-11.9467	9.14841
H	12.7974	-12.236	9.69358
H	13.92478	-14.1837	7.75384
H	12.20566	-13.0031	1.76034
C	12.51558	-10.8091	1.57131
H	14.67673	-11.7748	2.94547
H	10.71475	-12.0171	2.06418

H	13.28814	-9.16508	3.40447
H	11.83726	-14.5292	4.09344
C	12.14068	-16.4671	5.11974
C	13.32184	-16.2645	7.24037
H	15.68031	-13.0251	6.91644
C	17.2985	-13.2903	5.42263
C	16.71783	-12.5901	3.1688
H	15.14464	-10.0865	7.15291
C	15.87948	-8.24143	6.18758
C	14.83927	-7.71769	4.05439
H	11.1052	-9.94706	7.82482
C	9.66147	-8.42604	7.11395
C	9.61556	-8.19485	4.68947
H	11.05542	-9.51321	3.61985
H	9.74463	-12.6013	4.22362
C	8.14302	-13.3167	5.57201
C	8.80765	-13.4045	7.91431
H	10.89185	-12.7434	8.26476
F	15.39722	-12.0846	10.45597
F	12.1659	-10.6284	0.23395
H	11.64318	-17.0677	4.33817
C	12.68401	-17.0776	6.27474
H	13.76612	-16.7092	8.14837
H	18.01455	-13.6958	6.15889
C	17.66616	-13.1305	4.06714
H	16.96963	-12.4366	2.10475
H	16.6053	-8.02872	6.99201
C	15.77366	-7.39084	5.06351
H	14.73446	-7.0863	3.1546
H	9.31634	-8.14258	8.12371
C	9.13057	-7.80405	5.95936
H	9.23095	-7.72249	3.76832
H	7.4006	-13.4598	4.76718
C	7.82164	-13.6044	6.91951
H	8.59533	-13.6177	8.97682
H	12.61665	-18.1721	6.41594
H	18.67639	-13.4137	3.71868
H	16.4135	-6.49397	4.97166
H	8.35511	-7.02117	6.04934
H	6.81733	-13.979	7.1904

Table S22. Coordination geometry of the cation for complex **3**.

Atom	x(Å)	y(Å)	z(Å)
Dy	0.00519	0.19189	-0.00639
O	-2.04506	0.40487	-0.55452
O	2.06471	0.35861	0.524
N	-0.05682	-2.3972	0.06445
N	-0.58696	-0.55046	2.34329
N	-0.38354	2.30483	1.40949
N	0.47615	2.21971	-1.51641
N	0.56326	-0.69705	-2.31556
F	-3.9145	-1.33383	0.6143
F	-3.30661	-1.93794	-1.40887
C	-3.38387	0.43939	-0.94376
F	3.82847	-1.55649	-0.53353
F	3.21178	-1.98123	1.53186
C	3.40883	0.35002	0.8952
C	0.98858	-3.14334	-0.36776
C	-1.13977	-3.05846	0.53992
C	0.30601	-1.23015	3.1018
C	-1.79714	-0.27136	2.88041
C	0.26195	2.53097	2.57657
C	-1.26718	3.23766	0.98745
C	1.39555	3.13425	-1.13239
C	-0.14931	2.41393	-2.69997
C	1.77807	-0.49006	-2.87422
C	-0.35022	-1.40567	-3.02151
H	-4.04613	1.27489	0.97673
C	-3.98264	-0.96933	-0.70922
H	-1.77259	3.00791	0.0392
H	-2.93069	0.08216	-3.05979
H	-2.4955	0.26298	2.22066
C	-4.20512	1.44099	-0.10579
C	-3.53331	0.77433	-2.44145
H	4.10122	0.98801	-1.08864
C	3.92999	-1.10205	0.7598
H	1.85767	-2.59098	-0.74611
H	1.2709	-1.45182	2.62278
C	4.27087	1.23948	-0.02441
C	3.59563	0.78808	2.36182
C	0.99597	-4.54221	-0.33646
C	-1.222	-4.45412	0.59565
H	-1.97746	-2.43787	0.88133
C	0.0299	-1.63908	4.41161

C	-2.1572	-0.64683	4.17976
H	0.96928	1.75014	2.88931
C	0.0577	3.67838	3.35193
C	-1.53635	4.41275	1.69837
H	1.88009	2.93263	-0.16687
C	1.72373	4.25736	-1.90018
C	0.11394	3.50862	-3.5319
H	-0.89057	1.65178	-2.9782
H	2.49173	0.07587	-2.25872
C	2.12384	-0.97019	-4.14268
C	-0.08992	-1.91695	-4.29797
H	-1.31939	-1.56577	-2.52702
F	-5.28734	-1.05981	-1.07398
H	-5.28845	1.35734	-0.31883
H	-3.88615	2.47171	-0.35195
H	-3.17438	1.80731	-2.61308
H	-4.58822	0.71375	-2.77193
F	5.23199	-1.23503	1.12073
H	5.35006	1.12367	0.19462
H	4.00005	2.30076	0.13213
H	3.28769	1.84698	2.45951
H	4.65088	0.70188	2.68549
H	2.96989	0.1741	3.03735
H	1.88016	-5.08813	-0.6921
C	-0.13211	-5.21504	0.152
H	-2.13364	-4.92872	0.98288
H	0.79122	-2.18608	4.98407
C	-1.22461	-1.34134	4.9635
H	-3.15596	-0.399	4.56373
H	0.61188	3.80983	4.29119
C	-0.85986	4.64018	2.9051
H	-2.26754	5.13381	1.30826
H	2.48217	4.9653	-1.53917
C	1.07065	4.45009	-3.12577
H	-0.42528	3.61524	-4.48296
H	3.12745	-0.77783	-4.54535
C	1.17071	-1.6957	-4.87158
H	-0.86804	-2.48295	-4.82776
H	-0.16136	-6.31352	0.18627
H	-1.47377	-1.65064	5.98865
H	-1.0457	5.55244	3.48979
H	1.30367	5.3206	-3.75549
H	1.40835	-2.08686	-5.87117

Table S23. Calculated IR vibrational mode energies for **1**.

Mode-IR	Energy/cm^{-1}	Mode-IR	Energy/cm^{-1}	Mode-IR	Energy/cm^{-1}
1	15.8	77	619.0	153	1138.1
2	24.1	78	620.6	154	1138.3
3	26.2	79	630.0	155	1161.7
4	27.5	80	634.6	156	1165.9
5	29.3	81	639.8	157	1196.5
6	29.4	82	640.8	158	1196.6
7	30.6	83	641.0	159	1198.9
8	36.3	84	641.6	160	1200.2
9	38.5	85	643.2	161	1202.2
10	39.5	86	655.7	162	1203.7
11	45.1	87	656.3	163	1203.8
12	48.0	88	693.7	164	1206.2
13	50.4	89	694.1	165	1223.4
14	54.1	90	694.4	166	1242.5
15	56.6	91	697.7	167	1244.6
16	58.9	92	706.8	168	1310.1
17	59.6	93	712.5	169	1310.3
18	63.7	94	714.4	170	1314.5
19	67.5	95	741.8	171	1314.9
20	68.9	96	742.2	172	1315.7
21	71.5	97	743.9	173	1316.1
22	74.8	98	744.9	174	1317.1
23	75.1	99	746.8	175	1318.8
24	79.8	100	812.6	176	1318.8
25	91.3	101	812.7	177	1329.9
26	97.6	102	850.4	178	1330.6
27	104.8	103	851.2	179	1330.7
28	106.8	104	862.6	180	1331.6
29	111.9	105	862.8	181	1332.4
30	114.1	106	868.2	182	1430.7
31	128.0	107	869.9	183	1430.8
32	129.2	108	876.7	184	1431.5
33	129.7	109	925.9	185	1431.8
34	133.4	110	926.0	186	1432.5
35	135.6	111	934.3	187	1463.6
36	136.4	112	935.9	188	1464.1
37	142.3	113	953.9	189	1464.4
38	143.7	114	960.7	190	1465.2

39	158.3	115	960.9	191	1466.3
40	166.3	116	967.6	192	1580.5
41	169.1	117	968.0	193	1581.0
42	169.8	118	985.3	194	1581.5
43	177.6	119	989.9	195	1582.0
44	214.3	120	989.9	196	1582.4
45	237.7	121	991.8	197	1609.6
46	257.9	122	992.0	198	1610.8
47	258.7	123	994.6	199	1611.6
48	259.5	124	1004.5	200	1611.7
49	261.6	125	1004.6	201	1612.1
50	283.4	126	1006.7	202	2852.9
51	283.4	127	1007.0	203	2853.6
52	314.0	128	1009.6	204	3126.8
53	314.6	129	1018.7	205	3128.7
54	353.7	130	1019.2	206	3128.8
55	355.4	131	1027.3	207	3128.9
56	373.0	132	1027.8	208	3128.9
57	376.2	133	1029.2	209	3130.6
58	379.5	134	1030.0	210	3135.1
59	379.5	135	1030.1	211	3135.1
60	383.5	136	1060.4	212	3136.5
61	410.5	137	1061.4	213	3138.1
62	414.6	138	1061.5	214	3139.0
63	415.5	139	1061.9	215	3143.2
64	419.2	140	1062.0	216	3143.9
65	423.2	141	1063.2	217	3143.9
66	484.2	142	1063.9	218	3144.2
67	484.9	143	1065.5	219	3147.8
68	494.0	144	1065.5	220	3151.4
69	494.1	145	1066.8	221	3151.7
70	506.1	146	1122.2	222	3151.7
71	506.1	147	1123.3	223	3152.2
72	521.3	148	1134.9	224	3153.3
73	521.4	149	1135.1	225	3155.9
74	615.9	150	1135.1	226	3156.4
75	616.1	151	1135.2	227	3157.5
76	617.9	152	1135.3	228	3157.5

Table S24. Calculated Raman vibrational mode energies for **1**.

Mode-Raman	Energy/cm^{-1}	Mode-Raman	Energy/cm^{-1}	Mode-Raman	Energy/cm^{-1}
1	15.8	77	619.0	153	1138.1
2	24.1	78	620.6	154	1138.3
3	26.2	79	630.0	155	1161.7
4	27.5	80	634.6	156	1165.9
5	29.3	81	639.8	157	1196.5
6	29.4	82	640.8	158	1196.6
7	30.6	83	641.0	159	1198.9
8	36.3	84	641.6	160	1200.2
9	38.5	85	643.2	161	1202.2
10	39.5	86	655.7	162	1203.7
11	45.1	87	656.3	163	1203.8
12	48.0	88	693.7	164	1206.2
13	50.4	89	694.1	165	1223.4
14	54.1	90	694.4	166	1242.5
15	56.6	91	697.7	167	1244.6
16	58.9	92	706.8	168	1310.1
17	59.6	93	712.5	169	1310.3
18	63.7	94	714.4	170	1314.5
19	67.5	95	741.8	171	1314.9
20	68.9	96	742.2	172	1315.7
21	71.5	97	743.9	173	1316.1
22	74.8	98	744.9	174	1317.1
23	75.1	99	746.8	175	1318.8
24	79.8	100	812.6	176	1318.8
25	91.3	101	812.7	177	1329.9
26	97.6	102	850.4	178	1330.6
27	104.8	103	851.2	179	1330.7
28	106.8	104	862.6	180	1331.6
29	111.9	105	862.8	181	1332.4
30	114.1	106	868.2	182	1430.7
31	128.0	107	869.9	183	1430.8
32	129.2	108	876.7	184	1431.5
33	129.7	109	925.9	185	1431.8
34	133.4	110	926.0	186	1432.5
35	135.6	111	934.3	187	1463.6
36	136.4	112	935.9	188	1464.1
37	142.3	113	953.9	189	1464.4
38	143.7	114	960.7	190	1465.2

39	158.3	115	960.9	191	1466.3
40	166.3	116	967.6	192	1580.5
41	169.1	117	968.0	193	1581.0
42	169.8	118	985.3	194	1581.5
43	177.6	119	989.9	195	1582.0
44	214.3	120	989.9	196	1582.4
45	237.7	121	991.8	197	1609.6
46	257.9	122	992.0	198	1610.8
47	258.7	123	994.6	199	1611.6
48	259.5	124	1004.5	200	1611.7
49	261.6	125	1004.6	201	1612.1
50	283.4	126	1006.7	202	2852.9
51	283.4	127	1007.0	203	2853.6
52	314.0	128	1009.6	204	3126.8
53	314.6	129	1018.7	205	3128.7
54	353.7	130	1019.2	206	3128.8
55	355.4	131	1027.3	207	3128.9
56	373.0	132	1027.8	208	3128.9
57	376.2	133	1029.2	209	3130.6
58	379.5	134	1030.0	210	3135.1
59	379.5	135	1030.1	211	3135.1
60	383.5	136	1060.4	212	3136.5
61	410.5	137	1061.4	213	3138.1
62	414.6	138	1061.5	214	3139.0
63	415.5	139	1061.9	215	3143.2
64	419.2	140	1062.0	216	3143.9
65	423.2	141	1063.2	217	3143.9
66	484.2	142	1063.9	218	3144.2
67	484.9	143	1065.5	219	3147.8
68	494.0	144	1065.5	220	3151.4
69	494.1	145	1066.8	221	3151.7
70	506.1	146	1122.2	222	3151.7
71	506.1	147	1123.3	223	3152.2
72	521.3	148	1134.9	224	3153.3
73	521.4	149	1135.1	225	3155.9
74	615.9	150	1135.1	226	3156.4
75	616.1	151	1135.2	227	3157.5
76	617.9	152	1135.3	228	3157.5

Table S25. Calculated IR vibrational mode energies for **2**.

Mode-IR	Energy/cm^{-1}	Mode-IR	Energy/cm^{-1}	Mode-IR	Energy/cm^{-1}
1	22.8	71	653.5	141	1249.9
2	23.3	72	657.6	142	1263.0
3	27.0	73	659.7	143	1263.1
4	27.3	74	720.4	144	1278.8
5	30.9	75	729.0	145	1282.3
6	34.7	76	729.5	146	1284.4
7	41.6	77	733.1	147	1291.5
8	49.9	78	735.5	148	1292.2
9	61.3	79	740.7	149	1293.3
10	63.8	80	755.4	150	1293.8
11	68.6	81	755.8	151	1308.3
12	74.9	82	767.4	152	1311.8
13	85.8	83	768.4	153	1342.8
14	88.0	84	774.2	154	1388.2
15	97.9	85	776.1	155	1393.4
16	103.0	86	900.3	156	1400.5
17	107.0	87	915.2	157	1402.6
18	115.9	88	916.3	158	1437.5
19	120.1	89	932.3	159	1448.8
20	124.3	90	933.5	160	1487.7
21	128.8	91	938.0	161	1488.2
22	130.0	92	939.1	162	1489.3
23	132.2	93	952.6	163	1490.2
24	137.3	94	976.9	164	1493.1
25	139.2	95	978.9	165	1517.1
26	141.1	96	994.6	166	1540.9
27	148.6	97	1016.4	167	1543.5
28	155.4	98	1017.5	168	1569.5
29	159.0	99	1022.1	169	1575.7
30	160.4	100	1022.1	170	1594.8
31	163.8	101	1023.8	171	1596.1
32	176.0	102	1027.7	172	1644.6
33	187.5	103	1030.0	173	1646.2
34	198.2	104	1031.7	174	1646.5
35	201.7	105	1032.7	175	1652.9
36	207.7	106	1035.7	176	1654.3
37	208.7	107	1042.8	177	1666.1

38	224.9	108	1044.8	178	1668.9
39	229.1	109	1046.2	179	1669.3
40	241.1	110	1051.7	180	1673.1
41	246.6	111	1054.1	181	1674.4
42	301.8	112	1082.1	182	3110.4
43	311.8	113	1082.8	183	3112.3
44	314.1	114	1088.9	184	3142.4
45	322.2	115	1092.0	185	3145.6
46	384.0	116	1092.8	186	3178.0
47	400.9	117	1098.0	187	3182.8
48	402.4	118	1104.6	188	3203.3
49	408.2	119	1105.0	189	3204.3
50	413.8	120	1111.8	190	3220.7
51	416.7	121	1113.0	191	3224.1
52	420.4	122	1114.0	192	3378.3
53	420.6	123	1114.6	193	3380.2
54	430.6	124	1119.0	194	3389.7
55	431.7	125	1123.7	195	3392.1
56	449.5	126	1139.0	196	3392.2
57	455.9	127	1142.4	197	3392.4
58	468.7	128	1151.9	198	3395.3
59	469.5	129	1155.7	199	3395.7
60	517.3	130	1175.8	200	3400.5
61	537.5	131	1179.7	201	3404.7
62	626.1	132	1202.0	202	3405.3
63	634.3	133	1203.9	203	3407.4
64	643.4	134	1203.9	204	3407.5
65	647.2	135	1208.7	205	3411.4
66	647.5	136	1209.3	206	3413.6
67	648.5	137	1213.2	207	3413.7
68	649.5	138	1216.4	208	3416.5
69	650.9	139	1234.3	209	3416.6
70	651.5	140	1244.6	210	3419.3

Table S26. Calculated Raman vibrational mode energies for **2**.

Mode-Raman	Energy/cm^{-1}	Mode-Raman	Energy/cm^{-1}	Mode-Raman	Energy/cm^{-1}
1	22.8	71	653.5	141	1249.9
2	23.3	72	657.6	142	1263.0
3	27.0	73	659.7	143	1263.1
4	27.3	74	720.4	144	1278.8
5	30.9	75	729.0	145	1282.3
6	34.7	76	729.5	146	1284.4
7	41.6	77	733.1	147	1291.5
8	49.9	78	735.5	148	1292.2
9	61.3	79	740.7	149	1293.3
10	63.8	80	755.4	150	1293.8
11	68.6	81	755.8	151	1308.3
12	74.9	82	767.4	152	1311.8
13	85.8	83	768.4	153	1342.8
14	88.0	84	774.2	154	1388.2
15	97.9	85	776.1	155	1393.4
16	103.0	86	900.3	156	1400.5
17	107.0	87	915.2	157	1402.6
18	115.9	88	916.3	158	1437.5
19	120.1	89	932.3	159	1448.8
20	124.3	90	933.5	160	1487.7
21	128.8	91	938.0	161	1488.2
22	130.0	92	939.1	162	1489.3
23	132.2	93	952.6	163	1490.2
24	137.3	94	976.9	164	1493.1
25	139.2	95	978.9	165	1517.1
26	141.1	96	994.6	166	1540.9
27	148.6	97	1016.4	167	1543.5
28	155.4	98	1017.5	168	1569.5
29	159.0	99	1022.1	169	1575.7
30	160.4	100	1022.1	170	1594.8
31	163.8	101	1023.8	171	1596.1
32	176.0	102	1027.7	172	1644.6
33	187.5	103	1030.0	173	1646.2
34	198.2	104	1031.7	174	1646.5
35	201.7	105	1032.7	175	1652.9
36	207.7	106	1035.7	176	1654.3
37	208.7	107	1042.8	177	1666.1
38	224.9	108	1044.8	178	1668.9

39	229.1	109	1046.2	179	1669.3
40	241.1	110	1051.7	180	1673.1
41	246.6	111	1054.1	181	1674.4
42	301.8	112	1082.1	182	3110.4
43	311.8	113	1082.8	183	3112.3
44	314.1	114	1088.9	184	3142.4
45	322.2	115	1092.0	185	3145.6
46	384.0	116	1092.8	186	3178.0
47	400.9	117	1098.0	187	3182.8
48	402.4	118	1104.6	188	3203.3
49	408.2	119	1105.0	189	3204.3
50	413.8	120	1111.8	190	3220.7
51	416.7	121	1113.0	191	3224.1
52	420.4	122	1114.0	192	3378.3
53	420.6	123	1114.6	193	3380.2
54	430.6	124	1119.0	194	3389.7
55	431.7	125	1123.7	195	3392.1
56	449.5	126	1139.0	196	3392.2
57	455.9	127	1142.4	197	3392.4
58	468.7	128	1151.9	198	3395.3
59	469.5	129	1155.7	199	3395.7
60	517.3	130	1175.8	200	3400.5
61	537.5	131	1179.7	201	3404.7
62	626.1	132	1202.0	202	3405.3
63	634.3	133	1203.9	203	3407.4
64	643.4	134	1203.9	204	3407.5
65	647.2	135	1208.7	205	3411.4
66	647.5	136	1209.3	206	3413.6
67	648.5	137	1213.2	207	3413.7
68	649.5	138	1216.4	208	3416.5
69	650.9	139	1234.3	209	3416.6
70	651.5	140	1244.6	210	3419.3

Table S27. Calculated IR vibrational mode energies for **3**.

Mode-IR	Energy/cm^{-1}	Mode-IR	Energy/cm^{-1}	Mode-IR	Energy/cm^{-1}
1	19.8	83	642.1	165	1218.9
2	22.5	84	642.4	166	1262.7
3	27.3	85	642.9	167	1262.8
4	27.8	86	695.2	168	1314.9
5	28.6	87	696.1	169	1316.1

6	30.6	88	696.9	170	1316.6
7	36.0	89	698.9	171	1317.0
8	38.6	90	699.1	172	1317.7
9	40.0	91	724.7	173	1317.8
10	41.2	92	725.4	174	1320.5
11	44.5	93	742.6	175	1329.8
12	54.8	94	743.5	176	1330.2
13	57.4	95	744.1	177	1330.8
14	61.8	96	745.0	178	1331.6
15	65.3	97	745.4	179	1332.4
16	69.5	98	859.8	180	1337.0
17	72.9	99	862.0	181	1337.2
18	73.6	100	864.9	182	1393.4
19	77.8	101	865.3	183	1394.3
20	80.1	102	865.7	184	1401.3
21	91.5	103	866.4	185	1402.0
22	95.4	104	867.9	186	1415.0
23	96.1	105	885.4	187	1416.5
24	106.6	106	886.4	188	1428.3
25	109.0	107	926.5	189	1429.6
26	116.5	108	927.1	190	1430.7
27	124.4	109	929.3	191	1431.7
28	128.0	110	931.5	192	1431.9
29	129.9	111	936.5	193	1432.5
30	131.3	112	949.1	194	1433.3
31	131.9	113	951.2	195	1462.1
32	140.3	114	962.8	196	1462.6
33	143.5	115	964.8	197	1463.2
34	144.2	116	967.1	198	1464.4
35	147.7	117	971.3	199	1469.0
36	159.1	118	971.7	200	1580.6
37	171.3	119	989.0	201	1580.8
38	174.4	120	989.5	202	1581.7
39	179.0	121	990.1	203	1582.2
40	193.9	122	992.4	204	1582.9
41	211.2	123	992.7	205	1609.5
42	215.8	124	997.9	206	1609.7
43	224.7	125	1002.8	207	1609.7
44	236.4	126	1003.3	208	1610.2
45	237.9	127	1003.7	209	1613.1
46	252.3	128	1004.5	210	2984.6

Mode-Raman	Energy/cm⁻¹	Mode-Raman	Energy/cm⁻¹	Mode-Raman	Energy/cm⁻¹
47	255.1	129	1006.6	211	2985.1
48	269.8	130	1008.1	212	2988.7
49	272.9	131	1025.4	213	2989.3
50	325.9	132	1026.5	214	3073.4
51	328.8	133	1027.7	215	3073.8
52	356.4	134	1028.3	216	3078.5
53	356.9	135	1030.1	217	3078.8
54	357.8	136	1060.5	218	3079.4
55	359.3	137	1061.1	219	3080.0
56	377.3	138	1061.2	220	3080.6
57	377.6	139	1061.7	221	3081.1
58	382.5	140	1062.2	222	3126.0
59	385.3	141	1062.9	223	3126.1
60	386.1	142	1063.0	224	3127.1
61	413.1	143	1063.3	225	3127.3
62	416.1	144	1064.2	226	3128.4
63	416.7	145	1066.4	227	3129.0
64	418.6	146	1077.8	228	3129.2
65	419.4	147	1080.4	229	3132.5
66	463.6	148	1085.9	230	3133.5
67	464.5	149	1090.1	231	3135.0
68	465.0	150	1129.0	232	3135.4
69	466.1	151	1131.5	233	3138.5
70	551.8	152	1133.9	234	3138.9
71	552.9	153	1134.0	235	3143.2
72	568.0	154	1134.1	236	3147.9
73	569.8	155	1134.9	237	3148.0
74	587.9	156	1134.9	238	3148.3
75	589.5	157	1169.7	239	3148.5
76	614.0	158	1170.7	240	3149.2
77	614.5	159	1183.2	241	3153.5
78	615.1	160	1188.3	242	3153.7
79	617.7	161	1200.5	243	3153.7
80	618.8	162	1201.6	244	3153.8
81	640.5	163	1205.1	245	3164.0
82	640.7	164	1205.8	246	3166.8

Table S28. Calculated Raman vibrational mode energies for **3**.

Mode-Raman	Energy/cm⁻¹	Mode-Raman	Energy/cm⁻¹	Mode-Raman	Energy/cm⁻¹
1	19.8	83	642.1	165	1218.9
2	22.5	84	642.4	166	1262.7

3	27.3	85	642.9	167	1262.8
4	27.8	86	695.2	168	1314.9
5	28.6	87	696.1	169	1316.1
6	30.6	88	696.9	170	1316.6
7	36.0	89	698.9	171	1317.0
8	38.6	90	699.1	172	1317.7
9	40.0	91	724.7	173	1317.8
10	41.2	92	725.4	174	1320.5
11	44.5	93	742.6	175	1329.8
12	54.8	94	743.5	176	1330.2
13	57.4	95	744.1	177	1330.8
14	61.8	96	745.0	178	1331.6
15	65.3	97	745.4	179	1332.4
16	69.5	98	859.8	180	1337.0
17	72.9	99	862.0	181	1337.2
18	73.6	100	864.9	182	1393.4
19	77.8	101	865.3	183	1394.3
20	80.1	102	865.7	184	1401.3
21	91.5	103	866.4	185	1402.0
22	95.4	104	867.9	186	1415.0
23	96.1	105	885.4	187	1416.5
24	106.6	106	886.4	188	1428.3
25	109.0	107	926.5	189	1429.6
26	116.5	108	927.1	190	1430.7
27	124.4	109	929.3	191	1431.7
28	128.0	110	931.5	192	1431.9
29	129.9	111	936.5	193	1432.5
30	131.3	112	949.1	194	1433.3
31	131.9	113	951.2	195	1462.1
32	140.3	114	962.8	196	1462.6
33	143.5	115	964.8	197	1463.2
34	144.2	116	967.1	198	1464.4
35	147.7	117	971.3	199	1469.0
36	159.1	118	971.7	200	1580.6
37	171.3	119	989.0	201	1580.8
38	174.4	120	989.5	202	1581.7
39	179.0	121	990.1	203	1582.2
40	193.9	122	992.4	204	1582.9
41	211.2	123	992.7	205	1609.5
42	215.8	124	997.9	206	1609.7
43	224.7	125	1002.8	207	1609.7

44	236.4	126	1003.3	208	1610.2
45	237.9	127	1003.7	209	1613.1
46	252.3	128	1004.5	210	2984.6
47	255.1	129	1006.6	211	2985.1
48	269.8	130	1008.1	212	2988.7
49	272.9	131	1025.4	213	2989.3
50	325.9	132	1026.5	214	3073.4
51	328.8	133	1027.7	215	3073.8
52	356.4	134	1028.3	216	3078.5
53	356.9	135	1030.1	217	3078.8
54	357.8	136	1060.5	218	3079.4
55	359.3	137	1061.1	219	3080.0
56	377.3	138	1061.2	220	3080.6
57	377.6	139	1061.7	221	3081.1
58	382.5	140	1062.2	222	3126.0
59	385.3	141	1062.9	223	3126.1
60	386.1	142	1063.0	224	3127.1
61	413.1	143	1063.3	225	3127.3
62	416.1	144	1064.2	226	3128.4
63	416.7	145	1066.4	227	3129.0
64	418.6	146	1077.8	228	3129.2
65	419.4	147	1080.4	229	3132.5
66	463.6	148	1085.9	230	3133.5
67	464.5	149	1090.1	231	3135.0
68	465.0	150	1129.0	232	3135.4
69	466.1	151	1131.5	233	3138.5
70	551.8	152	1133.9	234	3138.9
71	552.9	153	1134.0	235	3143.2
72	568.0	154	1134.1	236	3147.9
73	569.8	155	1134.9	237	3148.0
74	587.9	156	1134.9	238	3148.3
75	589.5	157	1169.7	239	3148.5
76	614.0	158	1170.7	240	3149.2
77	614.5	159	1183.2	241	3153.5
78	615.1	160	1188.3	242	3153.7
79	617.7	161	1200.5	243	3153.7
80	618.8	162	1201.6	244	3153.8
81	640.5	163	1205.1	245	3164.0
82	640.7	164	1205.8	246	3166.8

Figure S31. Far-IR spectra of **1**. orange lines represent experimental data, blue lines and green lines represent calculated data of cation $[\text{Dy}((\text{OCH}(\text{CF}_3)_2)_2\text{py}_5]^+$ and $(\text{Bph}_4)^-$.
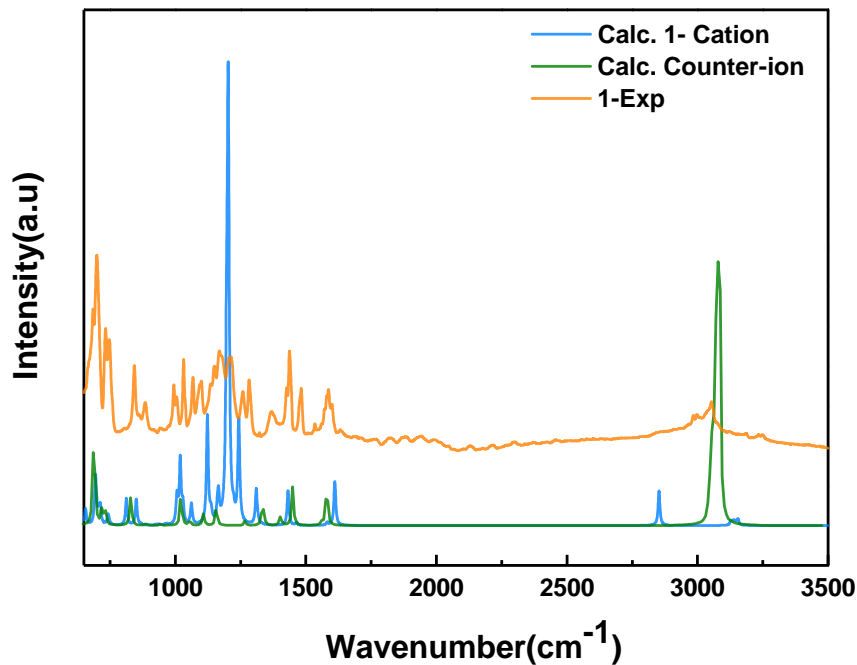
Figure S32. Vibrational spectra for **1**; orange lines represent experimental data, blue lines and green lines represent calculated data of cation $[\text{Dy}((\text{OCH}(\text{CF}_3)_2)_2\text{py}_5]^+$ and $(\text{Bph}_4)^-$.
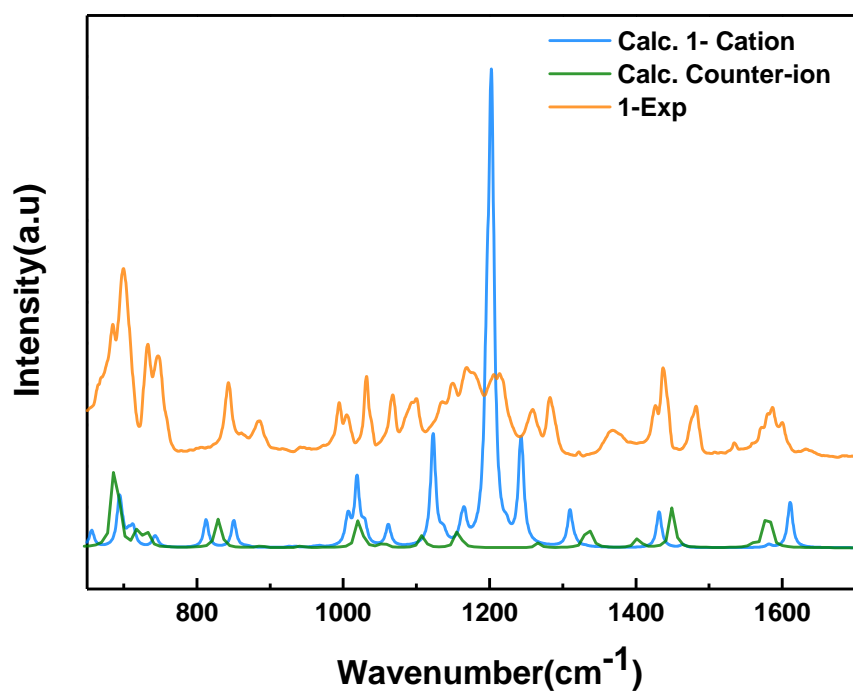
Figure S33. Vibrational spectra for **1** zoomed in to the region 650–1700 cm^{-1}; orange lines represent experimental data, blue lines and green lines represent calculated data of cation [Dy((OCH(CF$_3$)$_2$)$_2$py$_5$]$^+$ and (Bph$_4$)$^-$.
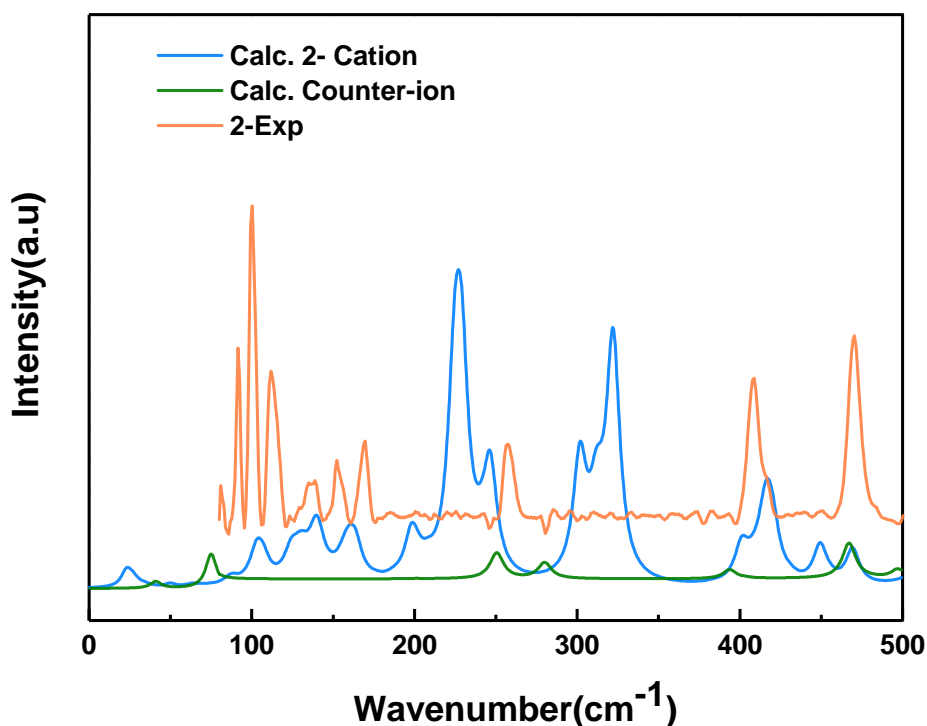
Figure S34. Far-IR spectra of **2**. orange lines represent experimental data, blue lines and green lines represent calculated data of cation [Dy((OCH$_2$CF$_3$)$_2$py$_5$]$^+$ and (Bph$_4$)$^-$.
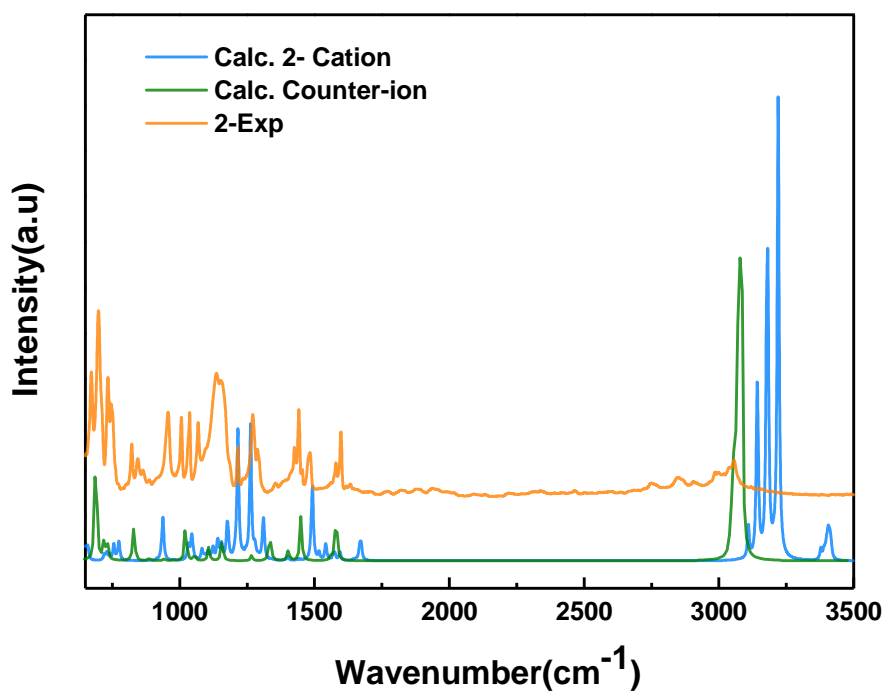
Figure S35. Vibrational spectra for **2**; orange lines represent experimental data, blue lines and green lines represent calculated data of cation $[Dy((OCH_2CF_3)_2py_5]^+$ and $(Bph_4)^-$.
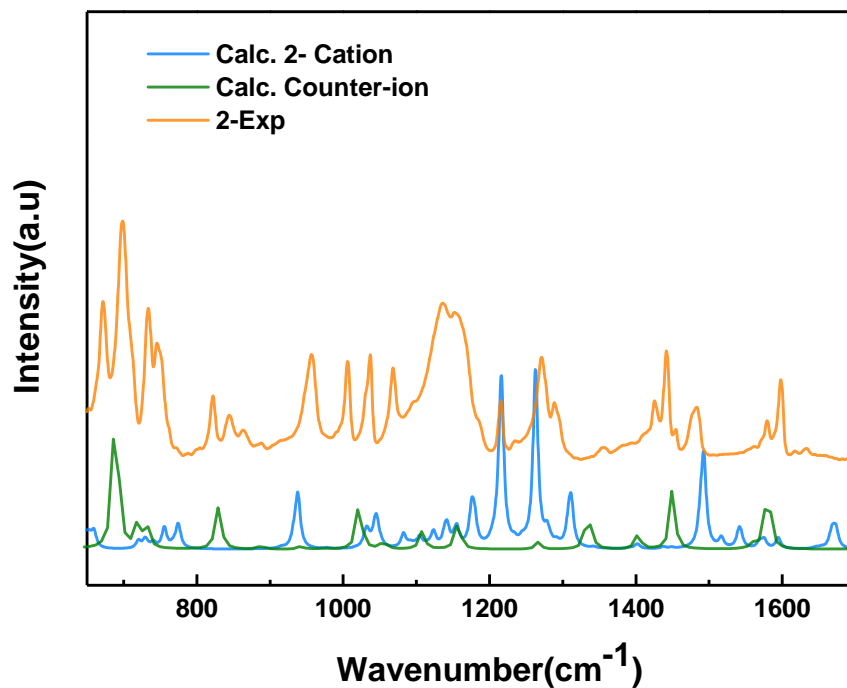
Figure S36. Vibrational spectra for **2** zoomed in to the region 650–1700 cm^{-1}; orange lines represent experimental data, blue lines and green lines represent calculated data of cation $[Dy((OCH_2CF_3)_2py_5]^+$ and $(Bph_4)^-$.
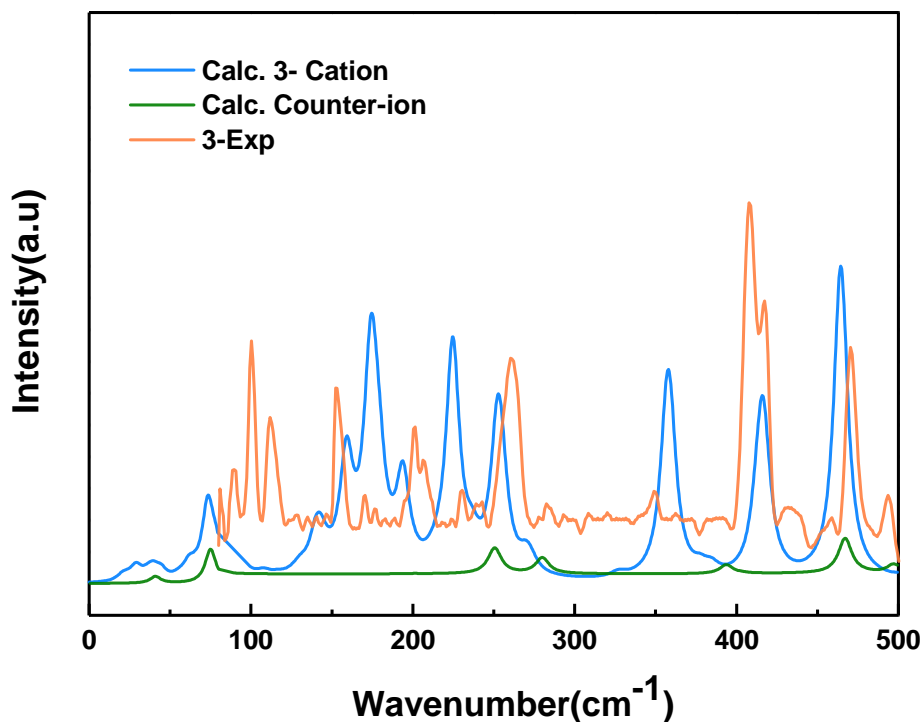
Figure S37. Far-IR spectra of **3**, orange lines represent experimental data, blue lines and green lines represent calculated data of cation $[Dy(OCMe_2CF_3)_2py_5]^+$ and $(Bph_4)^-$.
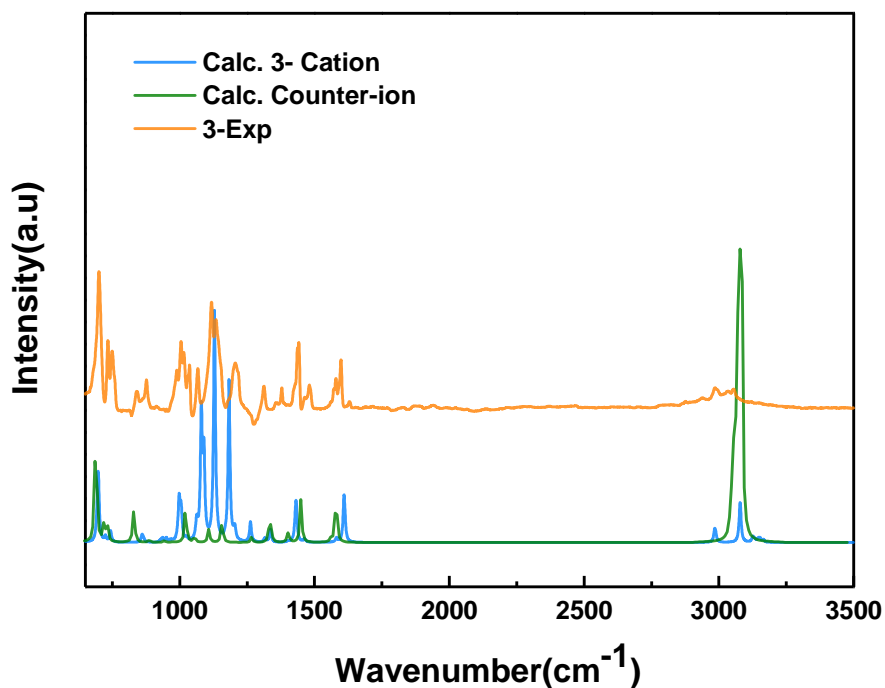
Figure S38. Vibrational spectra for **3**, orange lines represent experimental data, blue lines and green lines represent calculated data of cation $[Dy(OCMe_2CF_3)_2py_5]^+$ and $(Bph_4)^-$.
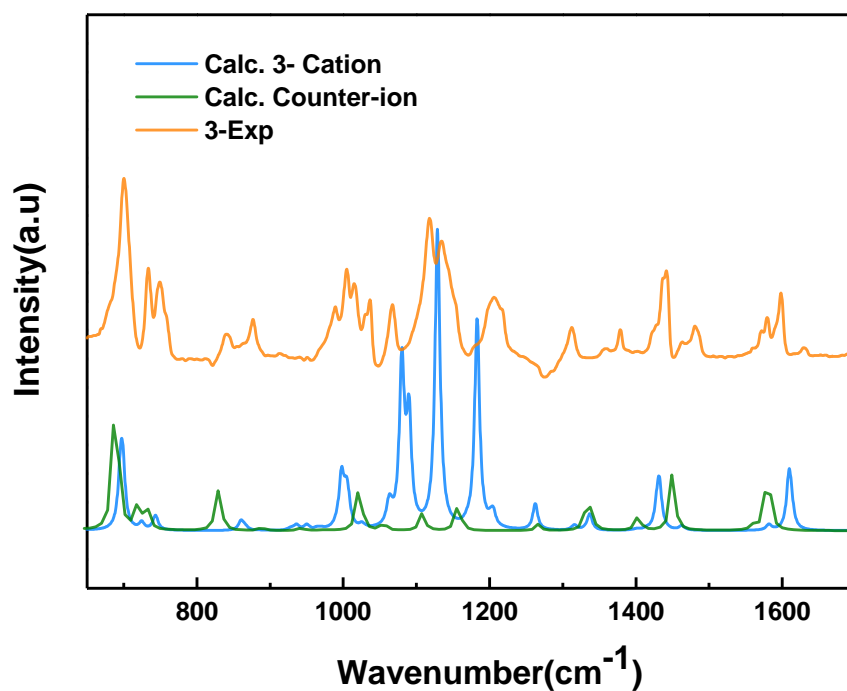
Figure S39. Vibrational spectra for **3** zoomed in to the region 650–1700 cm^{-1}, orange lines represent experimental data, blue lines and green lines represent calculated data of cation $[Dy(OCMe_2CF_3)_2py_5]^+$ and $(Bph_4)^-$.
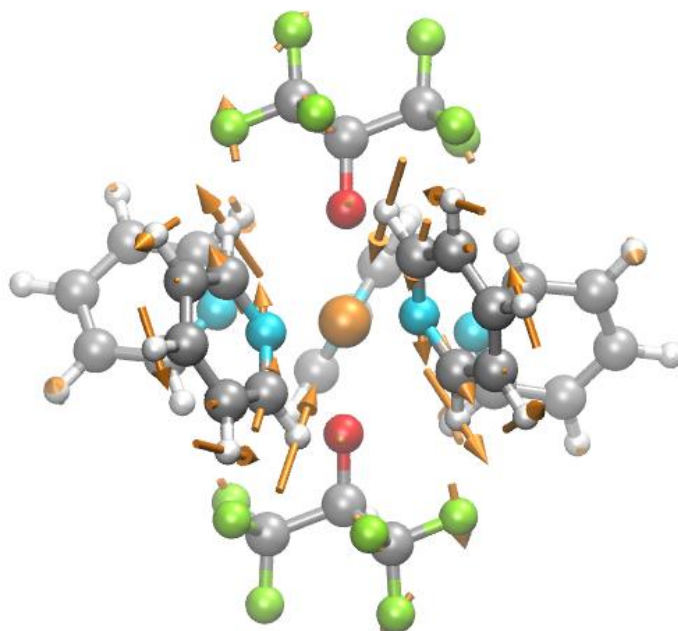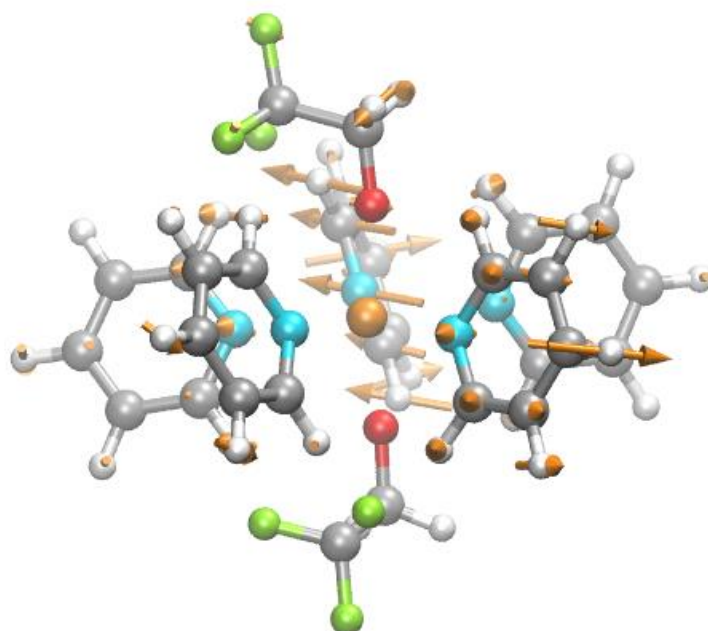

Figure S40. Vibrational mode 26 of complexes **1** according to DFT calculations on the optimized gas-phase molecular structure of **1**; see also Tables S20 and S23 and Figure S32.
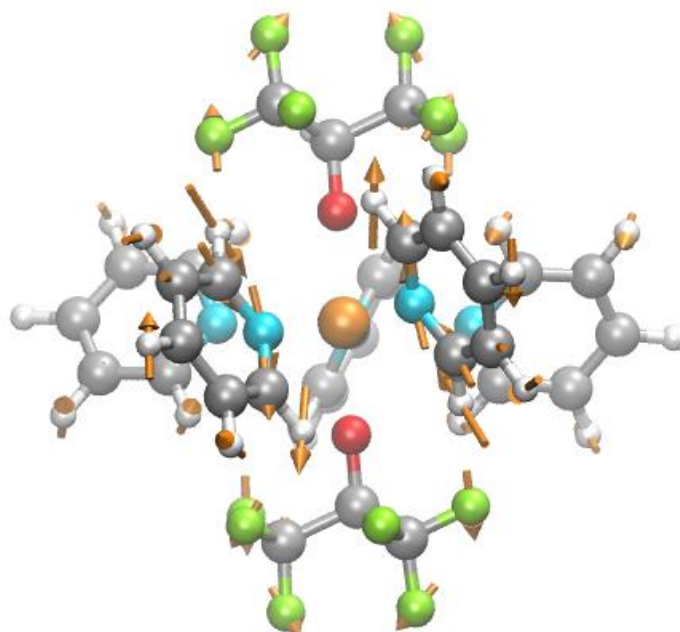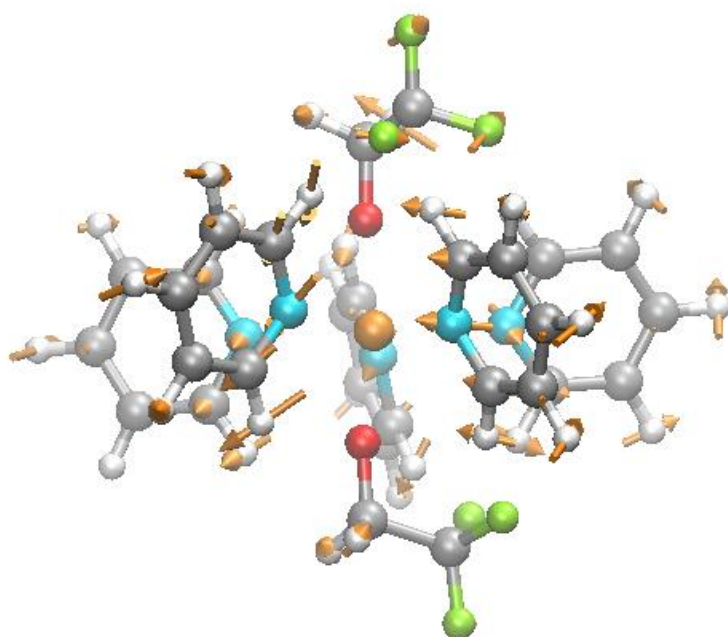
Figure S41. The vibrational mode 27 of complexes **1** according to DFT calculations on the optimized gas-phase molecular structure of **1**; see also Tables S20 and S23 and Figure S32.
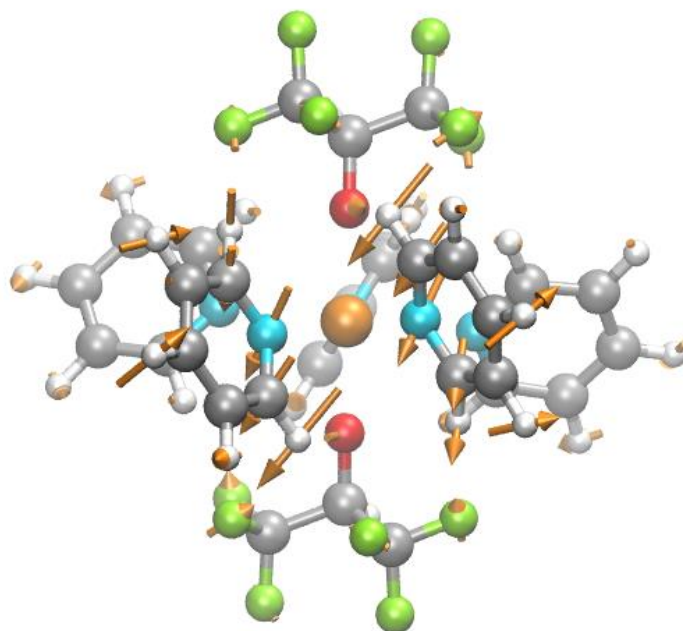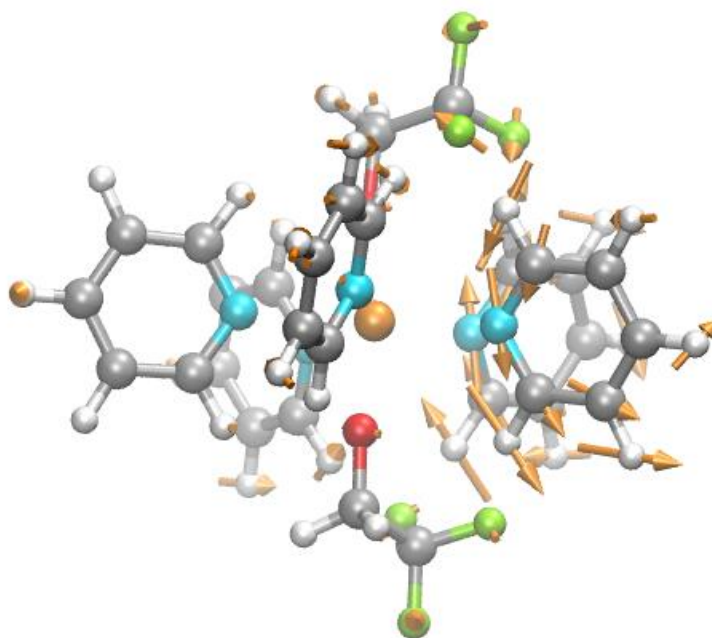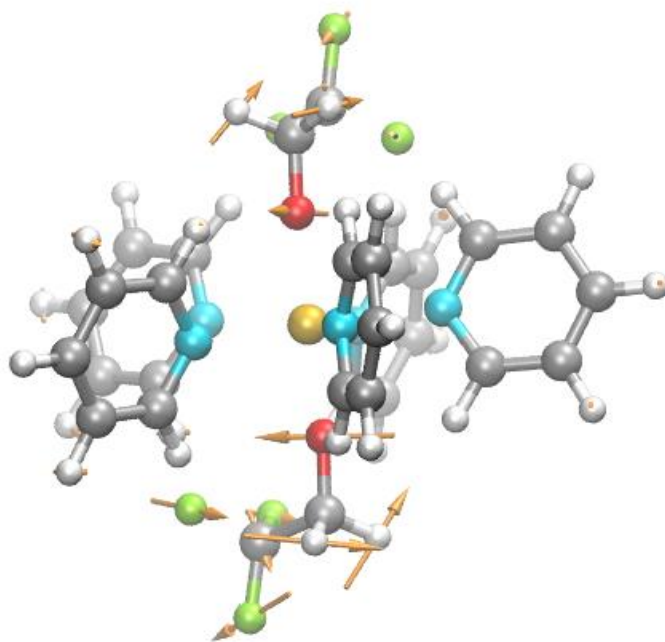

Figure S42. The vibrational mode 28 of complexes **1** according to DFT calculations on the optimized gas-phase molecular structure of **1**; see also Tables S20 and S23 and Figure S32.
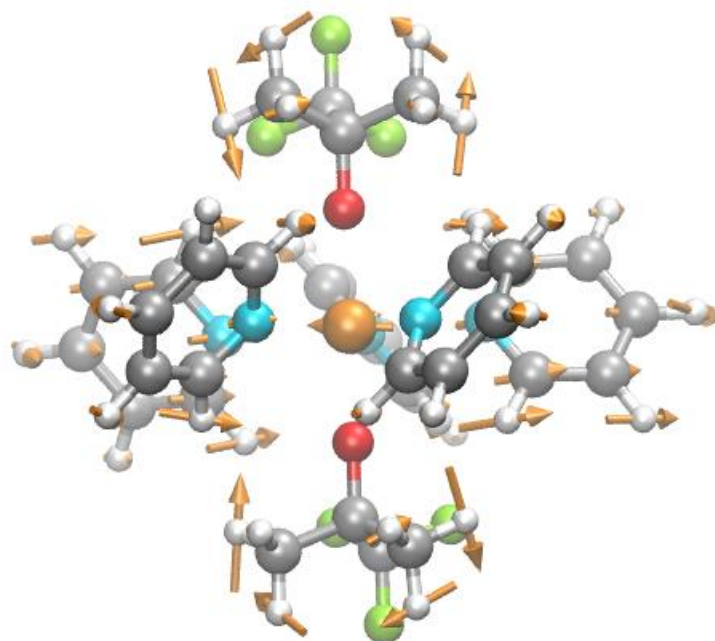
Figure S43. The vibrational mode 38 of complexes **1** according to DFT calculations on the optimized gas-phase molecular structure of **1**; see also Tables S20 and S23 and Figure S32.
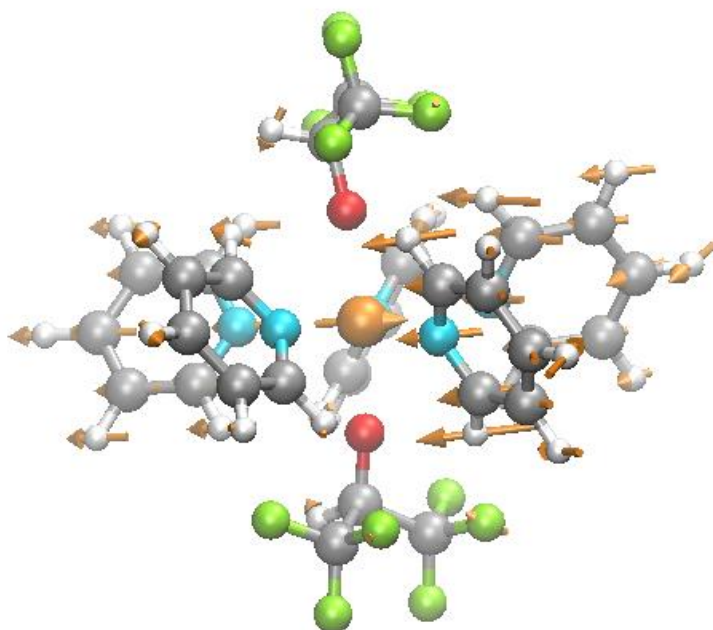
Figure S44. The vibrational mode 42 of complexes **1** according to DFT calculations on the optimized gas-phase molecular structure of **1**; see also Tables S20 and S23 and Figure S32.
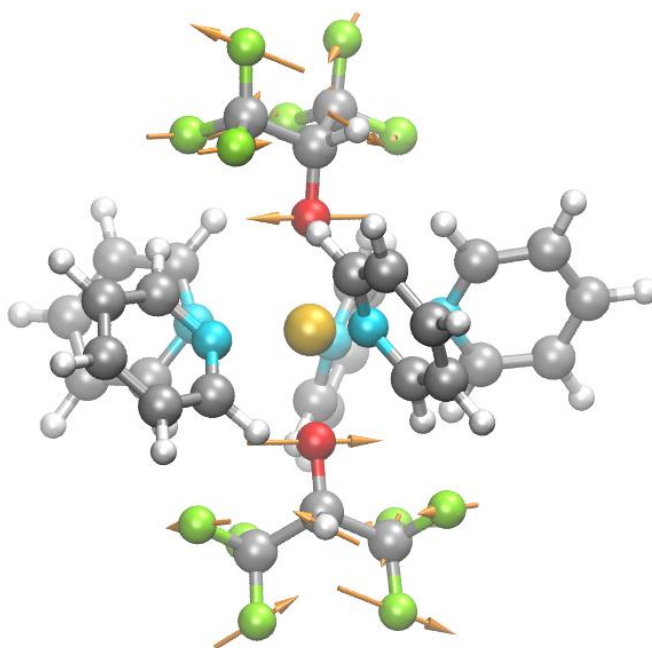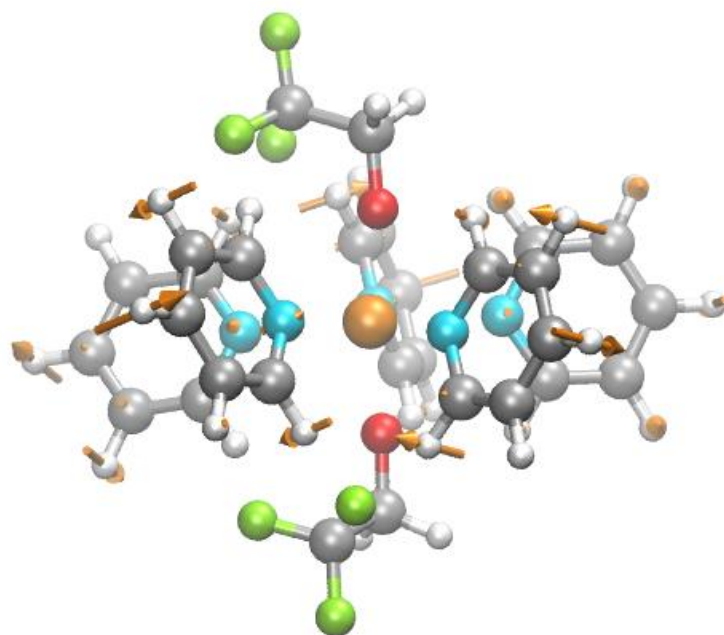
Figure S45. The vibrational mode 48 of complexes **1** according to DFT calculations on the optimized gas-phase molecular structure of **1**; see also Tables S20 and S23 and Figure S32.
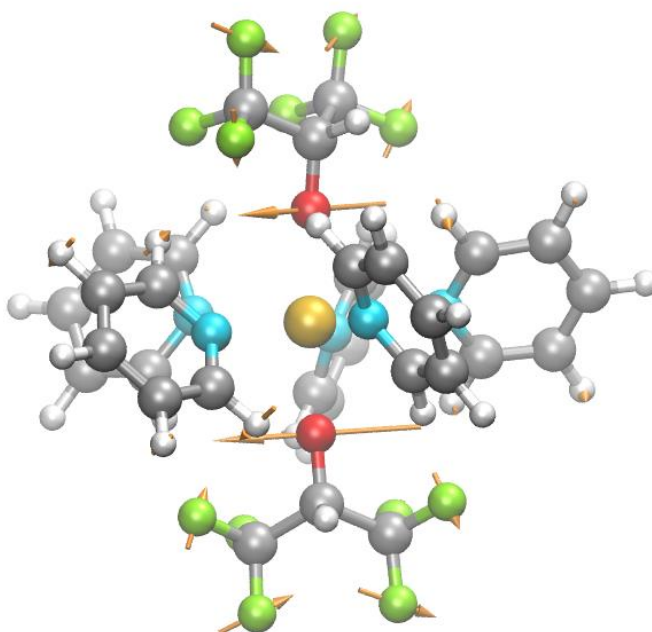
Figure S46. The vibrational mode 55 of complexes **1** according to DFT calculations on the optimized gas-phase molecular structure of **1**; see also Tables S20 and S23 and Figure S32.
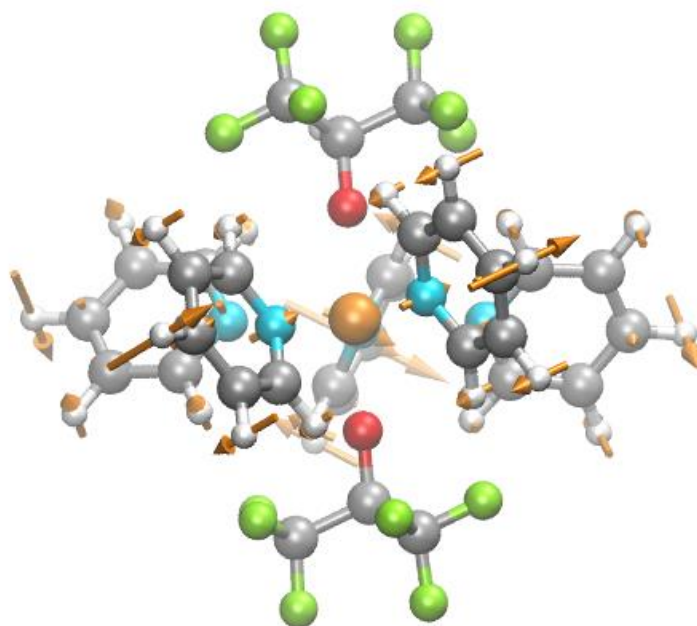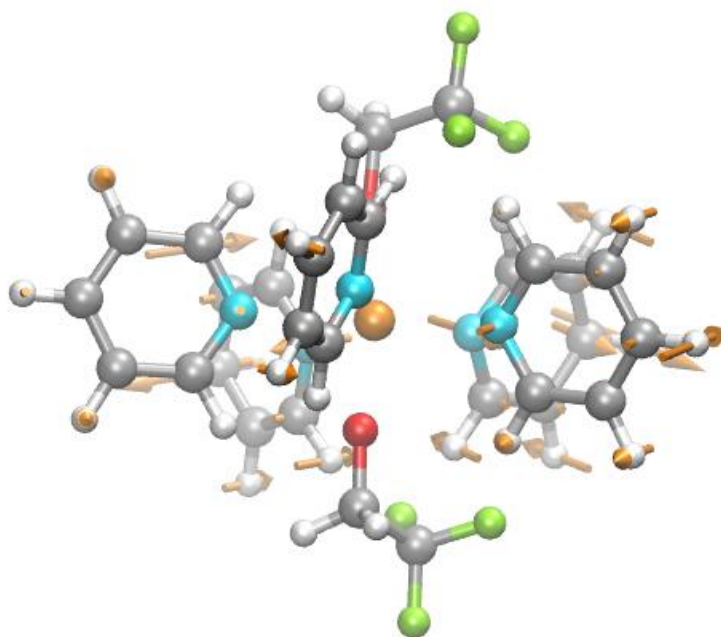
Figure S47. The vibrational mode 62 of complexes **1** according to DFT calculations on the optimized gas-phase molecular structure of **1**; see also Tables S20 and S23 and Figure S32.
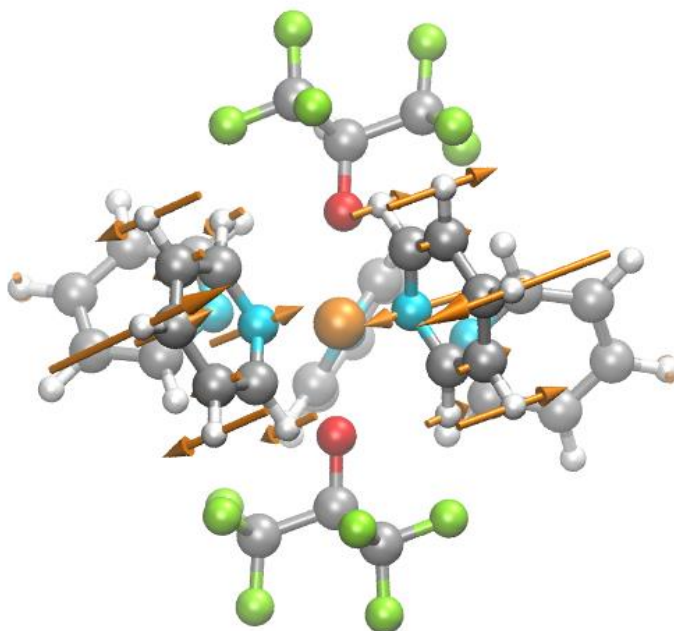
Figure S48. The vibrational mode 65 of complexes **1** according to DFT calculations on the optimized gas-phase molecular structure of **1**; see also Tables S20 and S23 and Figure S32.
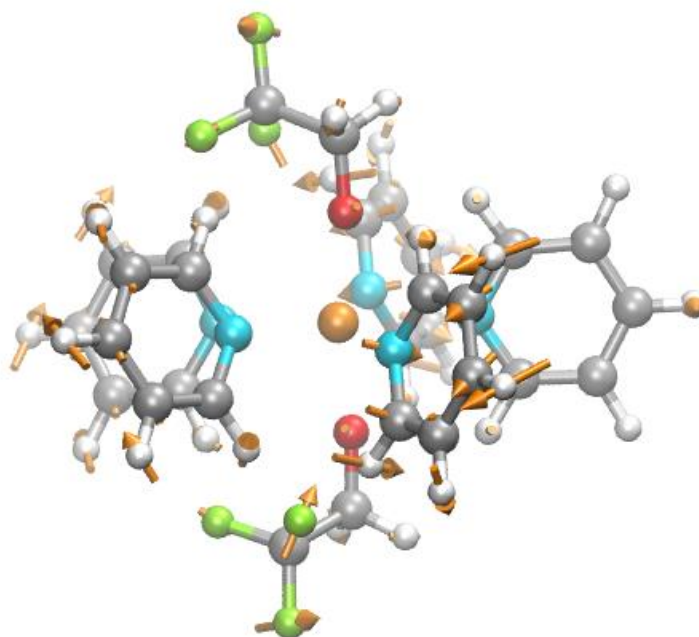
Figure S49. The vibrational mode 15 of complexes **2** according to DFT calculations on the optimized gas-phase molecular structure of **2**; see also Table S21 S25 and Figure S35.
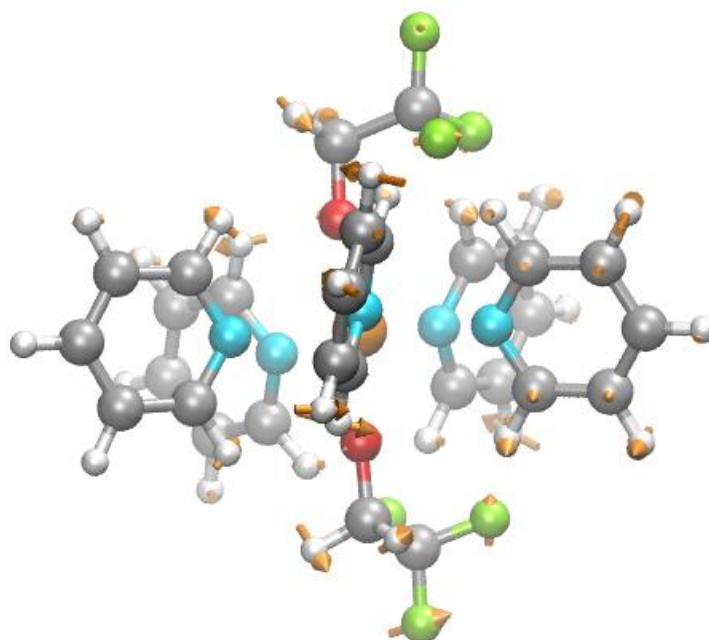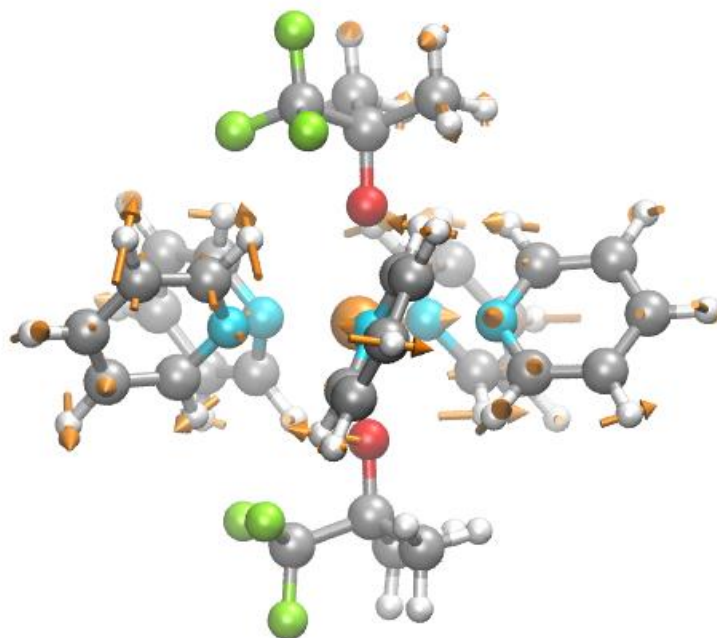

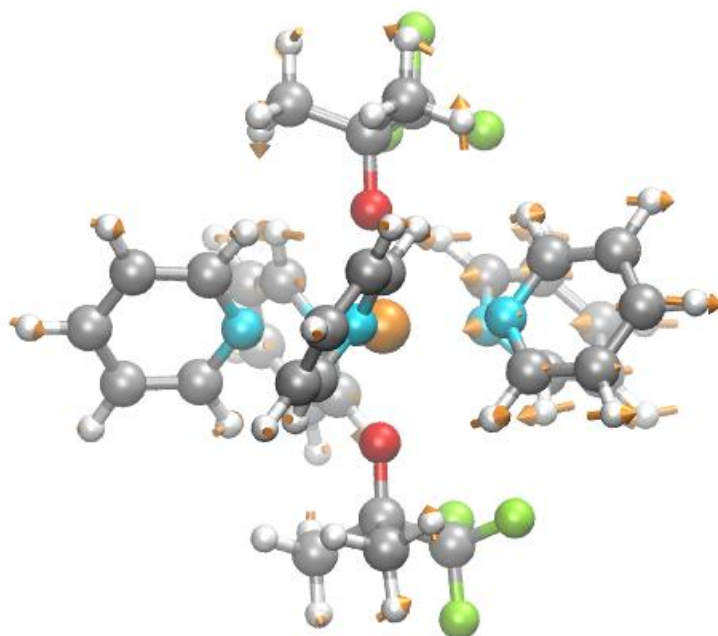**Figure S50**. Vibrational mode 16 of complex **2** according to DFT calculations on the optimized gas-phase molecular structure of **2**; see also Table S21 S25 and Figure S35.
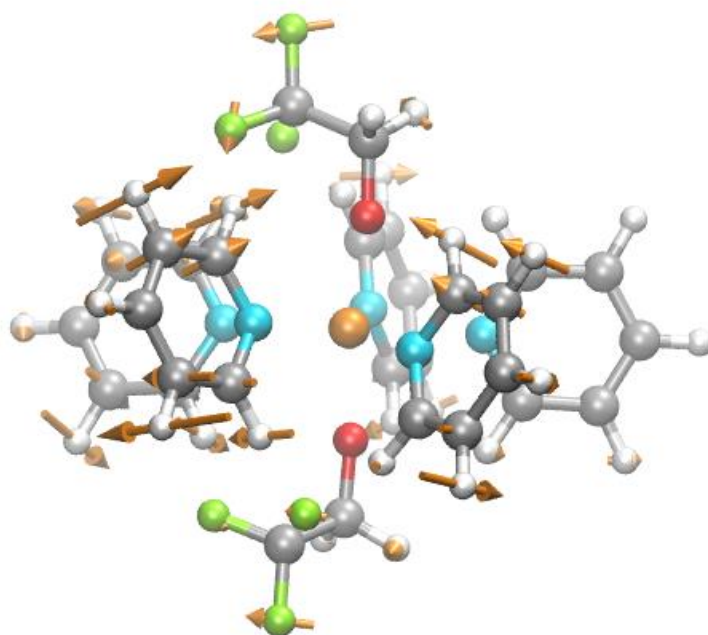
Figure S51. Vibrational mode 17 of complex **2** according to DFT calculations on the optimized gas-phase molecular structure of **2**; see also Table S21 S25 and Figure S35.

Figure S52. The vibrational mode 29 of complexes **2** according to DFT calculations on the optimized gas-phase molecular structure of **2**; see also Table S21 S25 and Figure S35.
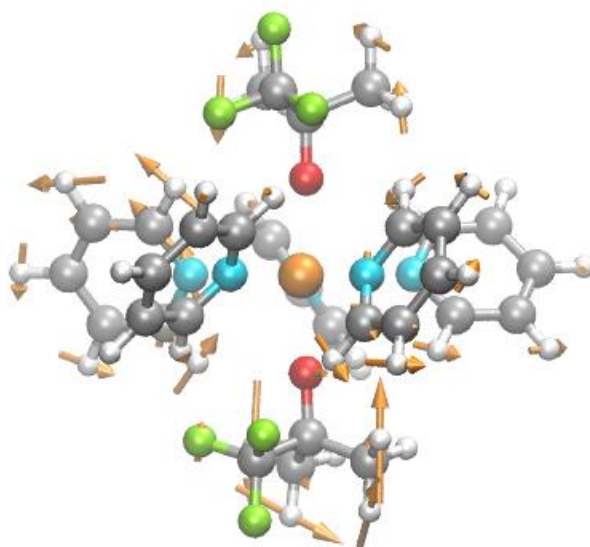
Figure S53. The vibrational mode 30 of complexes **2** according to DFT calculations on the optimized gas-phase molecular structure of **2**; see also Table S21 S25 and Figure S35.

Figure S54. Vibrational mode 31 of complex **2** according to DFT calculations on the optimized gas-phase molecular structure of **2**; see also Table S21 S25 and Figure S35.

Figure S55. The vibrational mode 41 of complexes **2** according to DFT calculations on the optimized gas-phase molecular structure of **2**; see also Tables S21 and S25 and Figure S35.
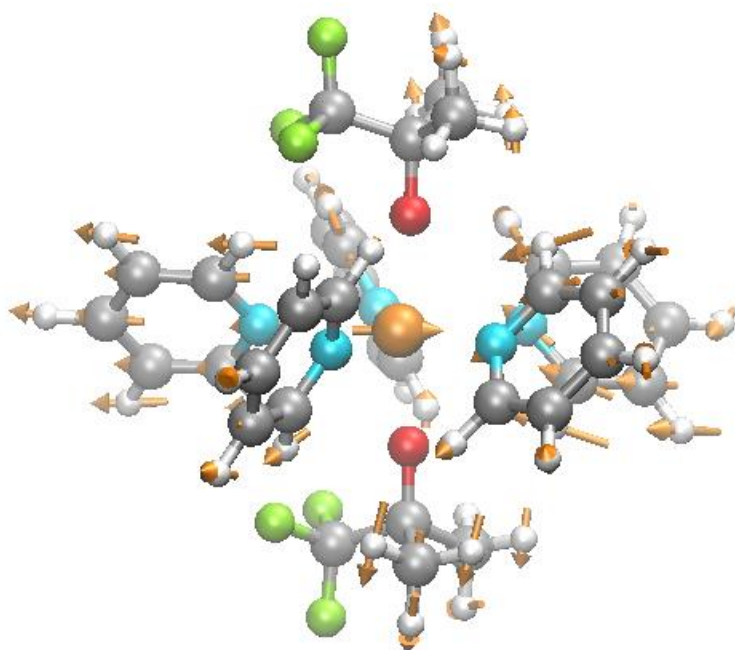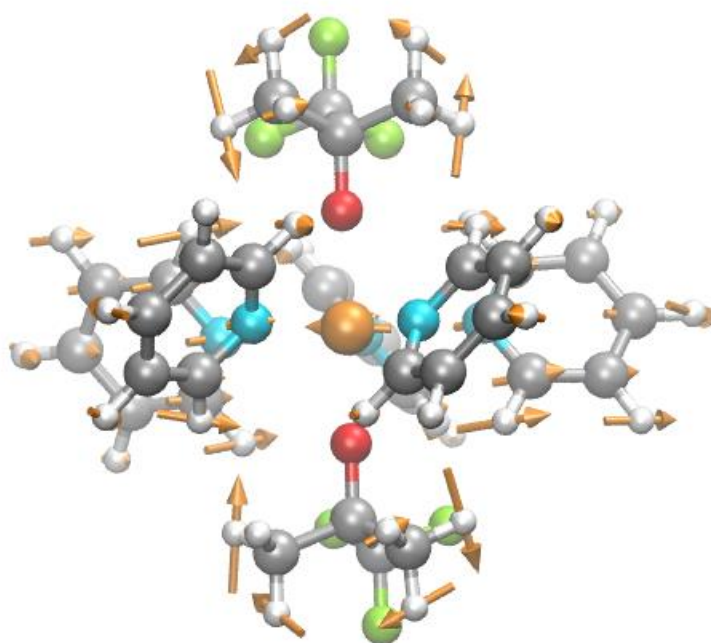

Figure S56. The vibrational mode 49 of complexes **2** according to DFT calculations on the optimized gas-phase molecular structure of **2**; see also Table S21 S25 and Figure S35.

Figure S57. The vibrational mode 55 of complexes **2** according to DFT calculations on the optimized gas-phase molecular structure of **2**; see also Table S21 S25 and Figure S35.

Figure S58. Vibrational mode 23 of complex **3** according to DFT calculations on the optimized gas-phase molecular structure of **3**; see also Tables S22 and S26 and Figure S38.

Figure S59. The vibrational mode 24 of complexes **3** according to DFT calculations on the optimized gas-phase molecular structure of **3**; see also Tables S22 and S26 and Figure S38.
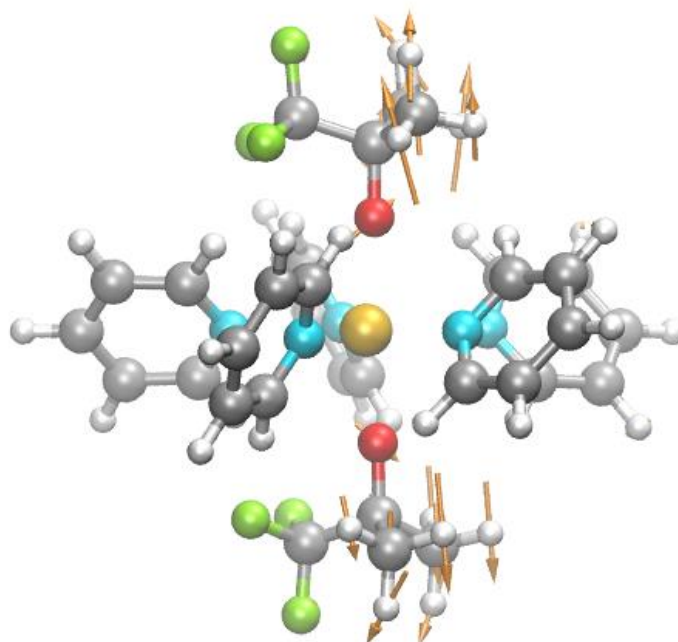

Figure S60. Vibrational mode 26 of complex **3** according to DFT calculations on the optimized gas-phase molecular structure of **3**; see also Tables S22 and S26 and Figure S38.

Figure S61. The vibrational mode 36 of complexes **3** according to DFT calculations on the optimized gas-phase molecular structure of **3**; see also Tables S22 and S26 and Figure S38.
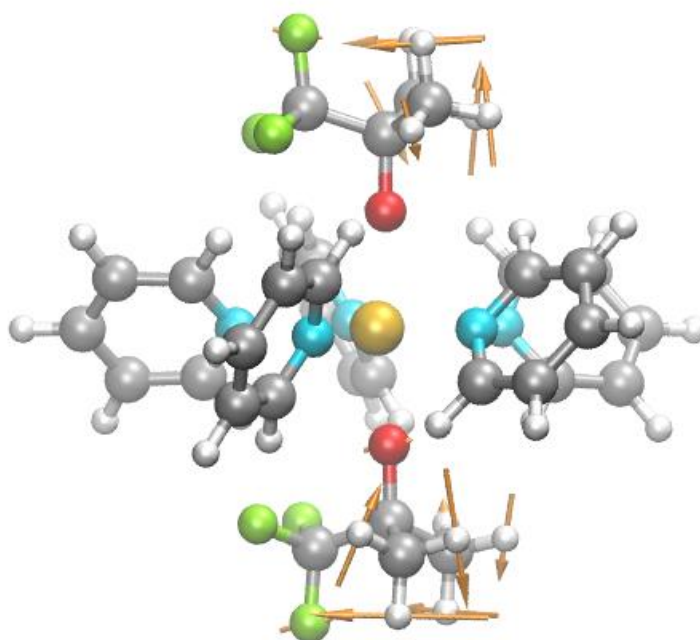

Figure S 62. The vibrational mode 38 of complexes **3** according to DFT calculations on the optimized gas-phase molecular structure of **3**; see also Tables S22 and S26 and Figure S38.
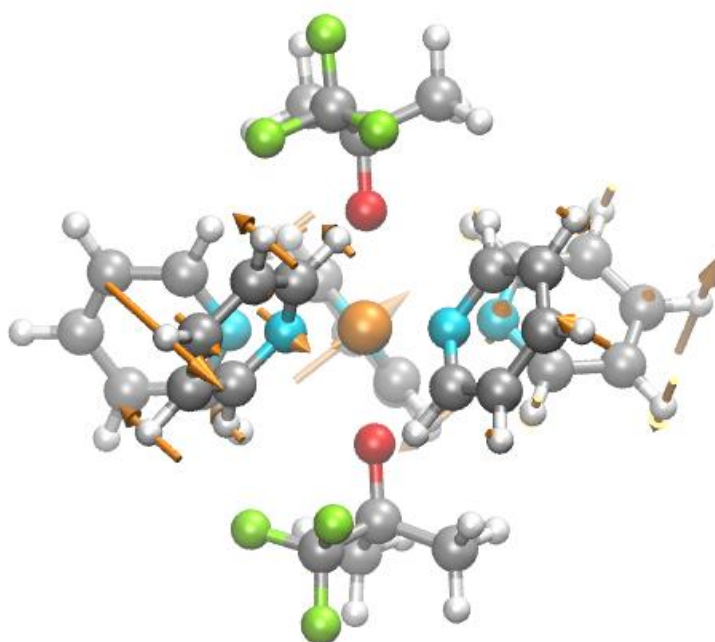
Figure S63. The vibrational mode 40 of complexes **3** according to DFT calculations on the optimized gas-phase molecular structure of **3**; see also Tables S22 and S26 and Figure S38.
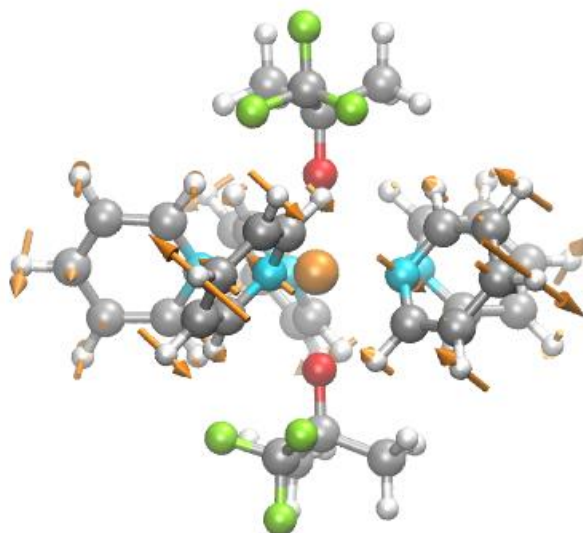

Figure S64. The vibrational mode 46 of complexes **3** according to DFT calculations on the optimized gas-phase molecular structure of **3**; see also Tables S22 and S26 and Figure S38.

Figure S65. Vibrational mode 63 of complex **3** according to DFT calculations on the optimized gas-phase molecular structure of **3**; see also Tables S22 and S26 and Figure S38.

Figure S66. The vibrational mode 65 of complexes **3** according to DFT calculations on the optimized gas-phase molecular structure of **3**; see also Tables S22 and S26 and Figure S38.
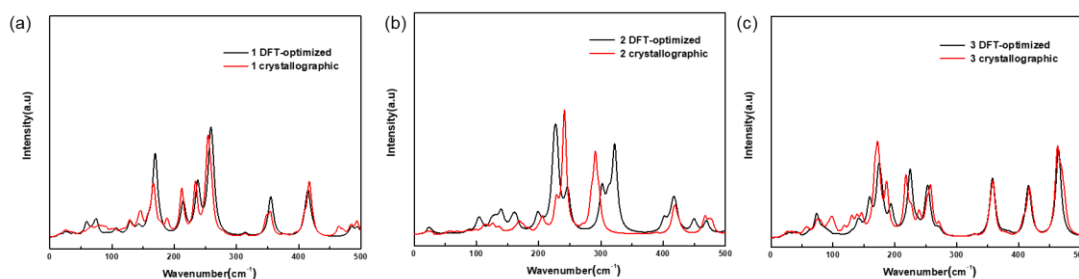
Figure S67. Calculated IR spectra in the range of 0–500 cm^{-1} for DFT-optimized and crystallographic structures of **1**–**3** (a)-(c).

References:

1. J. B. Reed, B. S. Hopkins, L. F. Audrieth, P. W. Selwood, R. Ward and J. J. Dejong, *Inorganic Syntheses, Volume 1* 28-33.
2. Sheldrick, G. M. Crystal structure refinement with SHELXL. *Acta Cryst. Sect. C.* **2015**, *71*, 3–8.
3. Sheldrick, G. M. A short history of SHELX. *Acta Cryst. Sect. A.,* **2008**, *64*, 112–122.
4. Dolomanov, O. V., Bourhis, L. J., Gildea, R. J., Howard, J. A. K., Puschmann, H OLEX2: a complete structure solution, refinement and analysis program. *J. Appl. Crystallogr.*, **2009**, *42*, 339–341.
5. B. O. Roos, R. Lindh, P. Å. Malmqvist, V. Veryazov, P. O. Widmark, *J. Phys. Chem. A*, **2004,** *108*, 2851–2858.
6. B. O. Roos, R. Lindh, P. Å. Malmqvist, V. Veryazov and P.O. Widmark, *Chem. Phys. Lett*., **2005**, *409*, 295–299.
7. a) P. J. Stephens, F. J. Devlin, C. F. Chabalowski, M. J. J. Frisch, *Phys. Chem.*, **1994**, *98*, 11623–11627; b) A. D. Becke, *J. Chem. Phys*., **1993**, *98*, 5648–5652; c) C. T. Lee, W. T. Yang, R. G. Parr, *Phys. Rev. B*., 1988, *37*, 785?789; d) A. D. Becke, *Phys. Rev. A*., **1988**, *38*, 3098–3100.
8. T. R. Cundari, W. J. J. Stevens, *Chem. Phys*., **1993**, *98*, 5555–5565.
9. M. J. Frisch, G. W. Trucks, H. B. Schlegel, G. E. Scuseria, M. A. Robb, J. R. Cheeseman, G. Scalmani, V. Barone, B. Mennucci, G. A. Petersson, H. Nakatsuji, M. Caricato, X. Li, H. P. Hratchian, A. F. Izmaylov, J. Bloino, G. Zheng, J. L. Sonnenberg, M. Hada, M. Ehara, K. Toyota, R. Fukuda, J. Hasegawa, M. Ishida, T. Nakajima, Y. Honda, O. Kitao, H. Nakai, T. Vreven, J. A. Montgomery, J. E. Peralta, F. Ogliaro, M. Bearpark, J. J. Heyd, E. Brothers, K. N. Kudin, V. N. Staroverov, R. Kobayashi, J. Normand, K. Raghavachari, A. Rendell, J. C. Burant, S. S. Iyengar, J. Tomasi, M. Cossi, N. Rega, N. J. Millam, M. Klene, J. E. Knox, J. B. Cross, V. Bakken, C. Adamo, J. Jaramillo, R. Gomperts, R. E. Stratmann, O. Yazyev, A. J. Austin, R. Cammi, C. Pomelli, J. W. Ochterski, R. L. Martin, K. Morokuma, V. G. Zakrzewski, G. A. Voth, P. Salvador, J. J. Dannenberg, S. Dapprich, A. D. Daniels, O?. Farkas, J. B. Foresman, J. V. Ortiz, J. Cioslowski, D.

J. Fox, Gaussian 09; Gaussian, Inc.: Wallingford, CT, 2009.

10. S. Grimme, *J. Comput. Chem*., **2004**, *25*, 1463–73.

11. T.H. Dunning, *J. Chem. Phys*., **1989**, *90*, 1007–1023.

12. a) L. Giuseppe, L. F. Ignazio, Chem. Phys. Lett., **1996**, 255, 341–346; b) E. A. Lucas, H. Y. Stephen, S. O. George, K. W. Angela, *J. Chem. Theory Comput*., **2017**, *13*, 2831–2839.